RICE UNIVERSITY

The biophysics of intracellular transport driven by structurally-defined systems of motor proteins.

by

D. Kenneth Jamison

A THESIS SUBMITTED IN PARTIAL FULFILLMENT
OF THE REQUIREMENTS FOR THE DEGREE

Doctor of Philosophy

APPROVED, THESIS COMMITTEE

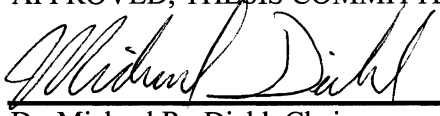

Dr. Michael R. Diehl, Chair
Assistant Professor of Bioengineering and
Assistant Professor of Chemistry,
Rice University

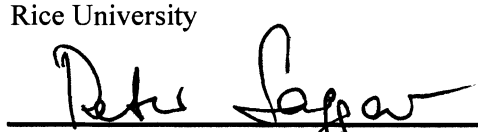

Dr. Peter Saggau
Professor, Department of Neuroscience,
Baylor College of Medicine

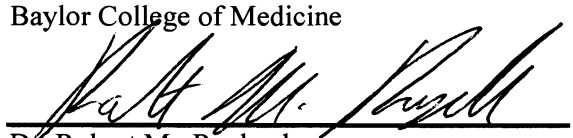

Dr. Robert M. Raphael
Associate Professor of Bioengineering,
Rice University

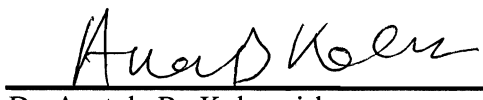

Dr. Anatoly B. Kolomeisky
Associate Professor of Chemistry and
Associate Professor of Chemical and
Biomolecular Engineering,
Rice University

HOUSTON, TEXAS
April 2011

Abstract

The biophysics of intracellular transport driven by structurally-defined systems of motor proteins.

by

D. Kenneth Jamison

The number of motor proteins attached to cellular cargos is widely believed to influence intracellular transport processes and may play a role in transport regulation. However, to date, investigating the biophysics of multiple-motor dynamics has been challenging since the number of motors responsible for cargo motion is not easily characterized. This work examines the transport properties of structurally-defined motor complexes containing two kinesin-1 motors, from both an experimental and theoretical perspective. Motor complexes were synthesized using DNA as a molecular scaffold and engineered DNA-conjugated protein polymers as linkers to couple motors to scaffolds. After anchoring the motor complexes to a bead their dynamic properties were measured using an automated optical trapping instrument that could be used to perform both static (increasing load) and force-feedback (constant load) optical trapping experiments. Data from these experiments is compared to predictions from a microscopic transition rate model of multiple kinesin dynamics. Together, these studies uncovered that multiple kinesins typically cannot cooperate since the microtubule-bound configuration of a motor complex often prevents both kinesins from sharing

cargo loads. Furthermore, multiple-motor behaviors are influenced by the fact that motor complexes display hysteretic force-velocity behaviors when applied loads change rapidly in time. Overall, such behaviors suggest the number of kinesins on a cargo will not be a key determinant of intracellular transport processes, and in turn, will not contribute appreciably to mechanisms that regulate cargo motion. However, this work also provides evidence that processive microtubule motors that are less efficient than kinesin (e.g., dynein) will cooperate productively, produce greater responses to motor number, and may therefore act as a regulator of cargo transport.

Acknowledgments

Thanks to my advisor and thesis committee chair, Michael R. Diehl, without his distinctive vision and tireless pursuit of excellence these studies would not have been possible. My sincere gratitude to Pamela E. Constantinou and Arthur R. Rogers, only through their skill and tenacity were these synthetic systems realized. Many thanks to Jonathan W. Driver for leading the development of all the theoretical work presented and through these efforts pushing the boundaries of our understanding.

A very special thank you to Dzifa Y. Duose for her constant support throughout these years and her irreplaceable friendship. Thanks to my brother Mark for always making me smile and reminding me what is most important in life. All my love to my parents who have sacrificed more than I can ever know to help me succeed and reach for my goals. And finally, thank you Jayita for making this long journey worthwhile.

Contents

List of Figures

List of Tables

List of Equations

Chapter 1

Introduction to Motor Proteins and their Role in Intracellular Transport

Intracellular transport of cytoplasmic materials in eukaryotic cells is a vital process in cell physiology. For cells to live, divide, and function efficiently a highly specific distribution and delivery of organelles, vesicles, protein complexes, mRNAs, and other cargos must be maintained within the cell. Processes as varied and essential as delivery of neurotransmitters along axonal extensions towards neuronal synapses to shuttling vesicle-membrane-bound proteins for post-translational modifications require proper molecular motor function. In fact, most proteins synthesized within a cell are carried to their final destination by transport motor proteins (Hirokawa, 2009). For small molecules (e.g. gases or glucose), purely diffusive motion often suffices to meet cellular transportation needs, but for larger objects and/or longer distances active

transport mechanisms are required for cellular functions to happen on a sufficiently fast time scale, especially within the highly viscous and extraordinarily crowded environment of the cytoplasm (Figure 1.1). Motor proteins provide the mechanism by which the cell can achieve its necessary subcellular organization and transportation activity. Motors hydrolyze ATP to carry cargos through the meshwork of the cytoplasmic matrix by binding processively along filamentous tracks known as microtubules (see Vale, 2003 for review). Microtubules have a specific orientation within cells; they generally radiate outward towards the cell periphery and originate at a central cell nucleus like spokes from the hub of a wagon wheel. Microtubules themselves are continuously in a state of growth and destruction. One end of the filament (the "plus-end") is always growing towards the periphery of the cell, through addition of tubulin proteins that are the basic component of microtubules, while the opposite end (the "minus-end") is continually breaking apart. Approximately 13 protofilaments (alternating alpha and beta tubulin protein sub units in a linear sequence) roll to form microtubules and provide multiple parallel pathways that molecular motors can access on a single microtubule (Amos, 2004). Kinesin and dynein, the two major classes of cytoplasmic motor proteins, found in abundance within nearly all multi-cellular organisms, favor motion towards opposite ends of microtubules (kinesin towards the peripheral plus-end and dynein towards the central minus-end) thereby providing a means for transportation of cargos to and from any location within a cell.

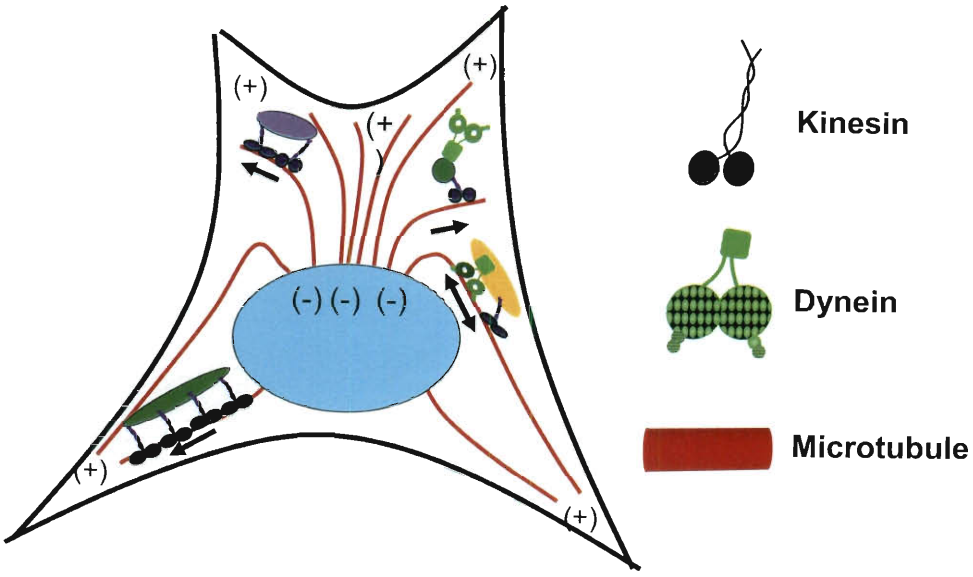

Figure 1.1: Intracellular Transport by the Motor Proteins Kinesin and Dynein

1.1. The Molecular Structure and Classification of Kinesin Motor Proteins

There are many different kinesin and dynein motor proteins that together comprise what are known as motor protein super-families. Molecular motors are generally composed of several protein domains. The motor protein kinesin (the primary focus of this thesis) is often found as a tetrameric protein consisting of two "heavy chains" and two "light chains". The tail-end "light-chain" is responsible for binding motors to cargos while the "heavy-chain" contains the stalk (or body) of the motor as well as two active motor domains These active motor domains ("motor heads") are the critical force-production elements of motor proteins where ATP hydrolysis takes place. In general, two motor amino acid chains (heavy chain monomers) combine through coiled-coil interaction of their stalks to form a two-headed motor protein system (see

Figure 1.2; Higuchi, 2004) that walks in a hand-over-hand fashion (Asbury, 2003) to move processively along microtubules (just as a child might reach out their arms one in front of the other to cross a set of monkey bars). Members of a particular motor protein super-family perform a wide variety of cellular functions yet typically share an active motor domain with 30-50% amino acid sequence overlap (Vale, 1996). Kinesin motors are further classified by the location of their active motor domain: N-kinesins and C-kinesins have their active domains in the amino-terminal and carboxyl-terminal regions, respectively, while M-kinesins active domains are somewhere in the middle of the motor protein (Miki, 2001; Lawrence, 2004). N-kinesins, the largest sub-family by far are all plus-end-directed motors and contain the kinesin-1 motor (a common motor within the kinesin super-family, and the focus of this thesis), which is primarily responsible for transport of intracellular cargos. Due to the similarity in the sequence of N-kinesin active domains and size of the overall protein it can be expected that conclusions from this work will benefit understanding of multi-motor processes of other closely related kinesin family members and thereby inform an even broader array of cellular functions.

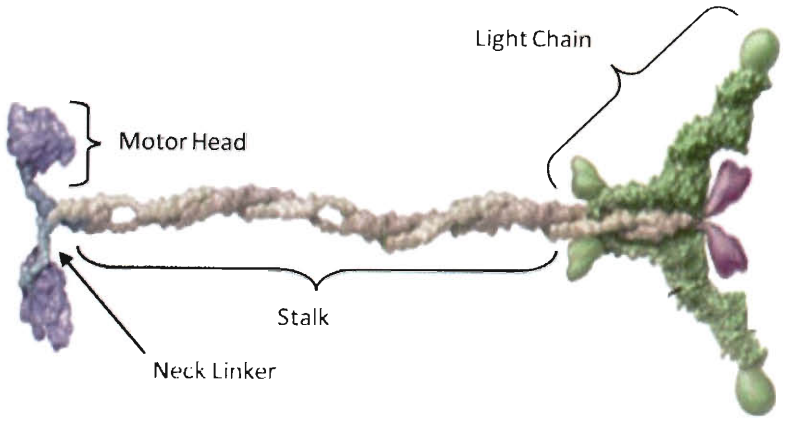

Figure 1.2: The Kinesin Motor Protein

Single kinesin motor molecules have now been studied for decades; one of the major areas of research has been focused on gaining an understanding of the structure and mechanics of the motor's active heads. These studies are a foundation from which one can begin to understand single motor protein dynamics, and a necessary stepping stone to appreciate larger multi-motor modes of intracellular transport. Atomic structures of human kinesins show the motor domain to be roughly 7.0 x 4.5 x 4.5 nm in size, composed primarily of a central 8-stranded beta-sheet with three helices on either side (Kull, 1996). An exposed cleft in the motor head serves as a nucleotide (ADP, ADP-Pi, or ATP) binding site; conformational changes occurring between ATP and ADP bound configurations enable changes in affinity between the motor head and microtubule track providing the mechanism by which the molecular motor may successively bind and unbind filaments to affect transport. Specifically, the motor domain has two "switch" residues located on mobile loops toward the rear of the nucleotide binding cleft which are thought to act as sensors to the bound nucleotide state. These residues move in to

form hydrogen bonds with ATP when it is in the cleft and subsequently move away when a hydrolyzed phosphate is released. This hydrolysis reaction occurs by an attack of an ordered water molecule to cleave a phosphate from ADP, transitioning the motor head into a force-generating state. Although, it is important to note that there is still much debate surrounding the nature of kinesin's power stroke (how exactly the chemical energy from ATP is converted to mechanical work), and today the field is moving towards understanding this phenomenon as a result of conformational changes in the protein (Rice, 1999) coupled with a random filament binding-site search powered by thermal fluctuations (Hirokawa, 2008). Nevertheless, it has been shown that a point mutation of a single residue at the so-called "switch II" site yields completely inactive motors, suggesting that these switching conformational changes do indeed hold a critical role in the mechanochemical cycle of kinesin (Vale, 1996).

Another critical structural component of the kinesin motor molecule is the "neck linker" connecting the motor's active head domains to its long coiled-coil stalk. The neck region is also thought to be a key mechanistic determinant of motor motility; this small string of 14-18 amino acids (Shastry, 2010) displays high sequence conservation only between motor subclasses with similar motile properties, suggesting its critical role in motor performance. The neck linker also plays a key role in communicating inter-head strains that coordinate both heads from simultaneously detaching from their filament and is crucial for the biased forward directional motion exhibited by kinesin (Miyazono, 2010). Experimental results show that strain between motor heads of a single kinesin are responsible for mechanochemical "gating" of the forward head, i.e.

rearward strain prevents microtubule-release of the leading head by inhibition of ATP binding, increasing processivity (Guydosh, 2006). Conversely, on the opposite end of the motor molecule the "tail" domains display extreme sequence variability within a given motor super-family (Goldstein, 1993). Many of the unique motor-membrane binding interactions that govern biological function are determined by this "tail" domain of motor proteins by directing particular motor types to bind specific cargos and thereby orchestrating the proper distribution, organization, and polarization of cytosolic components. In this study the cargo-binding tail domains of kinesin motors are replaced by protein sequences that impart both specific binding and designed elastic properties to motor assemblies. Replacing the tail end of the motor molecule has no bearing on the motile properties of the kinesin motor, and provides a convenient means for engineering desirable assemblies of motor proteins. In the study of motor proteins, and particularly kinesin, there is a long history of the use of recombinant DNA techniques to build artificial motor protein systems that can yield great insight into the mechanics of individual motors. Such studies have elucidated how: intramolecular strain coordinates kinesin stepping (Yildiz, 2004; Miyazono, 2010), neck linker length can control overall motor processivity (Shastry, 2010), and monomeric motor domains are capable of acting independently as force-generating elements (Diehl, 2006). In the study described within, truncations of the motor protein kinesin (where the tail-end binding regions of kinesin are removed, but the motor and neck linker domains essential for normal motor processivity remain untouched) are genetically engineered for incorporation into two-motor assemblies while preserving their overall native dimeric structure.

1.2. Motor Proteins Perform a Variety of Important Cellular Tasks

While the primary focus of this thesis is the transport properties of motor proteins that are responsible for delivery and distribution of cellular materials, these conceptually simple processes can have broad impacts on long-term cellular and even organism-level functions. In particular, the role of motor proteins is quite refined in epithelial cells and neurons where vesicle transport down long axonal extensions of distances up to meters in certain cases (Grafstein, 1980) must be accommodated. Consider the lifecycle of a neuronal vesicle where newly synthesized membrane-enclosed cargos are produced in the cell body and transported anterogradely (toward the cell periphery, by kinesin motors) to the axon terminal where their cargos contribute to the process of neurotransmission by association with the synaptic plasma membrane and the subsequent release of neurotransmitter materials (LaVail, 1974). While, at the same time, endocytosis of depleted membrane forms new multivesicular bodies that are transported retrogradely to the cell body where they are degraded by lysosomes (Fahim, 1985), completing the cycle. Cytoplasmic transportation of this type has become extremely efficient during its 700 million years of evolution (Lasek, 1985) and happens on an incredibly grand scale. Consider that through any given cross-section of a neurite (any membranous projection from the cell body of a neuron) a flux of 30 vesicles/minute has been visually observed by DIC microscopy, equally divided between transportation to both ends of a microtubule (Hill, 2004). Given that typical neurons have on average two to three neurites measuring 300 microns in total length (Kimura,

2003), one can get a sense of the extent and variety of motor-driven transportation events occurring within a cell or neuronal network at any given moment.

Shuttling of vesicles along the axons between nerve cell bodies and synapses is just one important example of the many functions motor proteins play within the cell. Motors are also responsible for the movement of chromosomes during cell division (Hyman, 1991) and can play a profound role in early organism development (e.g. in *Drosophila* an asymmetric distribution of components within young embryos establishes a body plan for the future organism; Nusslein-Volhard, 1987). Kinesin family motors are also known to be responsible for: transport and organization of mitochondria along axons (Nangaku, 1994, Wozniak, 2005, Tanaka, 1998, Kanai, 2000), elongation of neurites (an essential process for wiring of the brain; Wedaman, 1996), shuttling of materials between the endoplasmic reticulum (ER) and Golgi apparatus (Stauber, 2006), lysosome transport (Gross, 2002), and transport of endosomes (Bananis, 2000) among other duties! The experimental studies described in later chapters investigate motor protein function at a fundamental level, and will therefore impact basic understandings and interpretations of nearly all kinesin-driven cellular transport processes, while theoretical insights garnered through analysis of experiments can inform an even broader set of motor functions.

1.2.1. Regulatory Mechanisms are Needed to Direct Motor-Protein Mediated Transport Tasks

Motor proteins contribute to a large variety of transport and cellular tasks, yet these duties are primarily accomplished by only two motor protein families (kinesin and dyneins, each with only a handful to tens of constituent family members). This incongruence between the number of intracellular transport tasks and the relatively small variety of motors available to do perform transport alludes to the underlying regulatory mechanisms that must be in place to provide the spatial and temporal variety in activity that has been observed during intracellular transport (Welte, 1998; Fahim, 1985; Adams, 1983; Schroer, 1985; Sato-Yoshitake, 1992; Lee, 1995). To compound upon this issue, transport tasks are neither uniform in their nature nor static in time. Differences in cargo size, shape, composition, and other factors such as cell type and cell lifecycle can place demands on the transportation machinery of the cell that are constantly changing in time. In meeting these demands kinesin and dynein, by virtue of their overall directionally-opposed motility characteristics, present the potential to interfere or work against each other. Therefore cellular transportation management schemes must be in place to regulate motor-motor interactions in order to promote efficient utilization of the available motor protein population and also to balance the net effect of competing motor populations to complete transport tasks. Control of the number and types of motors working collectively (or competitively) on a cargo are important method by which regulation might occur and varying transportation needs satisfied. As a result the experimental and theoretical studies described in later

chapters not only reveal how kinesins act in groups, but they also gives insight into the role that motor number can and cannot play as a regulatory control point for cellular functions.

Regulation of motor number might be accomplished by internal (e.g. motor-motor communication, motor assembly geometry) or external factors (regulatory kinases, adapter proteins). For example, recent reports indicate that the effective number of kinesin molecules driving cargo transport can be regulated by the decoration of microtubules with non-motile proteins such as tau (Vershinin, 2007). Tau proteins are thought to influence the average run lengths of cargo by decreasing the rates at which kinesin motors bind to microtubules, and have the effect of lowering time-averaged number of multiple kinesins simultaneously engaged in transport during cargo motion; single kinesins motile properties are unaffected by the tau protein. In this way, motor number might serve to regulate transport of subcellular commodities – highlighting the critical importance of understanding the detailed mechanics of multiple motor transport (cargo motility driven by more than one motor). On the other hand, interacting systems of motor proteins also possess intrinsic potential for self-regulation. Such mechanisms are proposed to govern collective transport of motor protein assemblies containing both kinesin and dynein (Muller, 2008; Kural, 2005). It is hypothesized that bidirectional transport in these motor systems facilitates sophisticated physiological functions including the ability to sense and report neuronal injuries as well as error correction mechanisms that prevent cargo from being sent to inappropriate locations in cells. These complicated behaviors are thought to arise from

competitive interactions between motors. Such competition arises through inherently stochastic stepping events that create the potential for motors to interfere or compete against each other (i.e. – through a tug-of-war). However, this description of competitive regulation has not been independently verified for any motor system, and cooperative mechanisms where kinesin motors deterministically yield to one another allowing uninhibited transport in either direction have also been proposed to explain bidirectional transport behaviors. This controversy highlights the importance of understanding factors that regulate microtubule attachment/detachment kinetics and the intrinsic activities of motor molecules in multi-component protein complexes. Transportation management schemes that can regulate motor-motor interactions could promote efficient and effective utilization of the motor protein populations attached to cargos and would therefore have a broad impact on motor-driven cellular processes. As we will see in later chapters, the study described within demonstrates that small groups of kinesins in general do not work cooperatively and most often display performance measurements nearly identical to a single kinesin. However, this should not suggest that motor number does not play a role in regulation of transport. In fact, kinesin's performance in groups can be viewed as a self-regulation mechanism that reduces the number of filament-bound kinesins to one. Further, the theoretical analysis in a later chapter predicts that other motor types (e.g. dynein) have distinct functional properties that may allow dynein number to act as a regulatory control point. Together, the distinct differences in kinesin and dynein cooperative behaviors give insight into bidirectional cargo motions and cellular-level regulation of cargo delivery.

1.3. Motor Proteins Work in Groups to Perform Essential Cellular Tasks

Several previous studies have provided evidence of motor proteins working in groups to move cargo *in vivo*. Early *in vivo* measurements show that mitochondria use as many as 4 – 6 dyneins for motility in the giant amoeba Reticulomyxa (Ashkin, 1990), electron microscopy of fixed cells suggest that 2 – 3 motors pull organelles *in vivo* (Hirokawa, 1998) and 1 – 5 motors are thought to be responsible for vesicle transport in neurons (Miller, 1985): Figure 1.3 shows that more than 65% of vesicle motility events observed in neurons involve two or more cross-links between cargo and microtubules for both plus- and minus-ended motility, suggesting that multiple-motor-driven transportation is the most common mode of intracellular locomotion within axons.

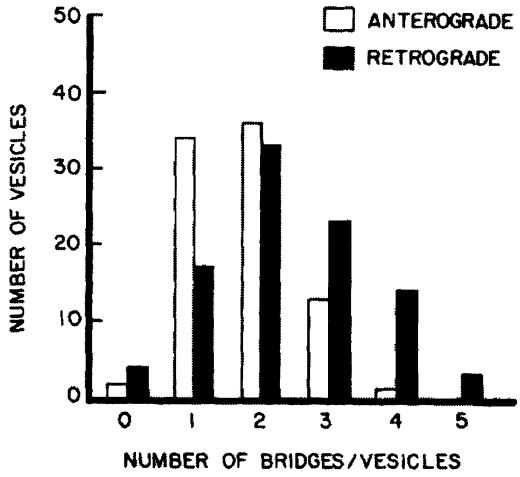

Figure 1.3: Multiple Motors Drive Motility of Neuronal Cargos *in vivo*

This is especially critical to realize given that intracellular transport along axons is perhaps the most physiologically important motor-dependent function due to its role in

maintaining neuronal health and function. In cells, large cargos and the diverse environments in which they are transported necessitate the simultaneous function of several motor proteins to work against higher loads and over longer distances than single motor proteins can achieve alone. As one example, the extra force-production by multiple motors is thought to be required for the extraction of membrane tubules during the formation of organelle structures including the Golgi Apparatus (Leduc, 2004), and also to drive movements of chromosomes during cellular division. An important distinction of collective motility from the case of single motors is that motors must not only work simultaneously, but they must also *share* applied loads while performing critical tasks. This sharing and communication of loads has made prediction of collective molecular motor behavior rather challenging, and highlights the substantial need for deeper mechanistic descriptions of how distributions of forces between motor molecules affects their global mechanical properties and configures their cellular function.

1.3.1. Single Motor Protein Studies have Formed a Foundation upon which Multiple Motor Behaviors can be Examined

To develop an accurate understanding of transport powered by multiple motors it is first necessary to understand how individual motors perform on their own. While *in vitro* studies of single motors have documented the capabilities of individual motor proteins exceptionally well, they have also revealed a large gap in performance between single motor function and the motility observed in live cells. Such comparisons of motor

protein performance have been cited as an indicator of multiple motors driving cargo *in vivo*. For example, dynein-powered glycoprotein complexes carried from the endoplasmic reticulum to the Golgi in living cells routinely move several microns in distance during a single interaction with a microtubule filament (Presley, 1997) and kinesin-driven motion of vesicles in neurites move distances of equal magnitude (Hill, 2004), while *in vitro* studies of single dynein and kinesin motion exhibit average run lengths of less than one micron (Wang, 1995). Multiple motors working together are thought to account for the discrepancy observed between experimental measured run length *in vitro* and *in vivo*; multiple dynein motors working on a single cargo *in vitro* have shown run lengths up to 8 microns (Mallik, 2005). However, as we will see in later chapters, the long run lengths observed experimentally *in* vivo cannot be the result of multiple motors alone, at least for the case of small numbers of kinesin motors for which nearly identical run lengths for single-kinesins and two-kinesin assemblies have recently been measured *in vitro* (Rogers, 2009). Still, there is the possibility that the differences between *in* vitro and *in* vivo run length measurements stems from the action of regulator factors such as the tau protein that hold the potential to mechanistically modulate motor-filament interactions.

Other measures of *in vivo* transportation also indicate cooperation of multiple motors. Within neurites of living PC12 cells, vesicles moving by the so called "fast axonal transport" mechanism, characterized by a range of high transport velocities, exhibit sudden jumps between constant velocities (Hill, 2004). The observed jumps in velocity suggest changes in the number of active motor proteins actively pulling the

vesicle. This approach to interpreting *in vivo* motility is bolstered by the observation that these instantaneous velocity changes occur after an average of 1.3 microns in both anterograde and retrograde directions, while *in vitro* run lengths of single kinesin motors pulling against beads in buffer have been measured as 1.4 microns (Block, 1990). Local changes in the cellular environment such as cytoplasmic crowding or spatial variations in viscosity have been ruled out in causing the observed velocity shifts; the cellular positions where vesicles switched speeds show no strong spatial correlation (Hill, 2003). This again suggests that changes in motor number actively pulling cargo explain features of observed motility in living cells which cannot be duplicated in the context of single motor protein studies. Further evidence for multiple motors working collectively in the cell comes from measured maximum vesicle velocities in neurons exceeding 4500 nm/s (Kaether, 2000), such speeds are wholly unattainable with single motor proteins (as is demonstrated in later chapters, single kinesin motors can only transiently attain velocities approaching 1000 nm/s – and then only under zero-load conditions). The study described within is the first instance where an arrangement of multiple motors and the geometric and mechanical parameters that define their system are rigorously known and controlled. As a result, these combined experimental and theoretical approaches have the unique ability to attribute multiple motor cargo behaviors to specific motor numbers and arrangements and therefore draw meaningful conclusions and interpretations to bridge the gap between what is known of single motors and the intracellular transport phenomena observed in living cells.

1.4. Optical Traps are Proven Tools for the Study of Single Motor Protein Motility

Over the last few decades researchers have utilized many experimental techniques ranging from common fluorescence techniques (Vale, 1996) to atomic force microscopy (Bornschlogl, 2008) and even micro-rheological methods (Holzwarth, 2002) in order to probe motor protein dynamics. During that time optical traps (or optical tweezers) have emerged as the most widely utilized, and perhaps the most sensitive and versatile tools to study motor motility. The nature of the physics that underlie optical traps make them particularly well suited to apply forces from 1 – 100 pN on biological materials; a physical range that is relevant for the study of many cellular and macromolecular-scale structures and processes. For example, optical traps have demonstrated the capability to halt swimming sperm cells, drag bacterium through water faster than they can swim (Berns, 1991), and distort DNA, RNA, and cytoskeletal filaments to investigate mechanical properties (Weber, 1992). Single motor proteins such as kinesin and dynein produce forces in the single to tens of piconewtons range, and as a result optical trapping devices have been used extensively for their study.

Optical traps are conceptually simple instruments that require little effort to set up in their most basic form. Most often in biological applications, an optical trap is established by a high numerical aperture objective tightly focusing an infrared laser beam (infrared wavelengths are selected because they are less prone to cause photodamage of trapped biological particles). Tightly focused Gaussian-profile laser

beams have extremely high intensity gradients that make optical trapping of small particles possible near the focus. Trapped particles experience radiation pressures (forces from a combination of scattering and absorption) from the laser light in proportion and direction of increasing light intensity gradient (Svoboda, 1994). Often, inorganic dielectric particles such as polystyrene microspheres are chosen as control "handles" for trapping experiments due to their favorable optical properties and versatility as substrates for molecular complexes (i.e. optical loads from the trap are applied to the microspheres themselves and thereby forces are imparted on any biological material linked to the beads surface). In the experimental studies that are the focus of this thesis 0.5 micron diameter polystyrene microspheres are utilized. This microsphere size is appropriate to apply a range of biologically significant forces on motor proteins while working with moderate trapping laser powers that are unlikely to introduce significant photodamage to trapped biomaterials, and also provides for a sufficiently large position detection range through the use of a back-focal-plane detection system (BFPDSs are advantageous for their ability to resolve the motions of trapped particles with extremely high resolution at very fast time scales, this detection system will be explained in more detail in Chapter 2). Use of 0.5 micron diameter polystyrene beads is motivated biologically as well; this is a typical size of many cytoplasmic cargos in the cell (Rogers, 1997), though it is somewhat larger than most vesicular cargos which are typically have diameters of ~200 nm (Miller, 1985). The study described in later chapters has utilized a more sophisticated form of optical trap than described here, which incorporates several measures to ensure laser power stability

(and therefore optical load stability) as well as the ability to apply dynamic loads to trapped particles, and mitigate sources of experimental noise, however, the fundamentals of the optical trap itself remain the same. Optical traps are particularly attractive methods for dynamic force applications because the forces they impart, in general, scale in the same manner as those of a simple Hookeian spring. For small lateral displacements (< ~150 nm) perpendicular to the optical axis, forces felt by trapped particles are proportional to displacements from the optical axis (Visscher, 1996); i.e. there is an F = kx relationship that describes the forces applied by optical traps (where 'F' is the optical trapping force, 'k' is a measure of the trap's stiffness in a Hookeian sense, and 'x' is the distance between the center of a trapped particle and the optical axis of the trapping laser). The combination of an optical trap's ease of use, versatility in applying range of forces to a vast assortment of targets, precise motion-detection methods, and geometric similarity to biological cargos makes it an unparalleled tool for studying motor protein dynamics at the single-molecule and the most appropriate candidate for the experimental investigations of this thesis at molecular-motor-assembly levels.

Optical traps have been used extensively to study the mechanics and transportation capabilities of single motor proteins working against a load. Trapping studies of single motors have revealed the mechanical elastic properties of motors, structural protein details, nanoscale stepping mechanics, specifics of motor mechanochemistry, and force production capabilities. For motor studies, optical traps are typically operated in one of two modes: "static" or "force-feedback". In a static

trap, the trapping laser remains stationary allowing motor molecules to pull against the trap as if tethered by a spring to a stationary object. In force-feedback mode constant loads are applied by dynamically moving the position of the trap. Figure 3a shows force-velocity curves for a single kinesin motor at limiting and saturating ATP concentrations; figure 3b shows single kinesin velocities against ATP concentrations and constant loads, both generated using an optical trap in force feedback mode (Visscher, 1998, 1999). These results are typical of motor protein studies that utilize optical traps, and they form a foundation upon which to understand and interpret multiple motor trapping studies. In the study described in later chapters, systems composed of two kinesins are evaluated by similar methods using both static and force-feedback trapping modes. Each mode has its benefits and limitations; in relating these modes to real intracellular transport behaviors it is sometimes useful to view the two trapping modes as limiting cases of motility where the static trap represents motors pulling a cargo passed a cytoplasmic obstacle, while the trap in force-feedback is more representative of cargo transport against relatively constant viscous load. As we will see in later chapters, the differences between static and force-feedback modes also plays a key role in understanding the instantaneous and steady-state dynamics of multiple motor systems, and how important these properties are for intracellular transport.

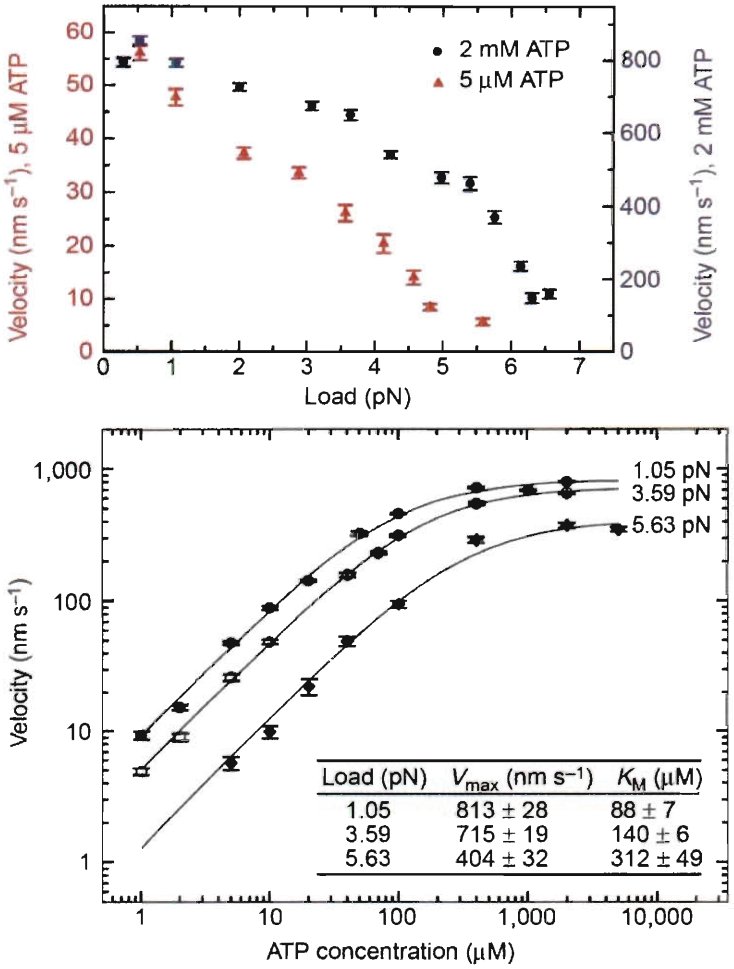

Figure 1.4: Motility Characteristics of Single Kinesin Motors Studied with Optical Traps

1.5. Previous Studies of Multiple-Motor Motility Lack Specific Knowledge and Control of the Motor Assemblies Driving Transport

While there is a growing body of work that examines multiple-motor motility (Welte, 1998; Vershinin, 2007; Beeg, 2008; Ross, 2008), results from these studies are confounded by the variability present in experimental systems and the resulting inability to make reliable interpretations of data sets. Specifically, experiments performed to date are limited by difficulties in determining the number of motors and their geometric arrangement on cargo. Current established *in vitro* assays only afford control over the average number of immobilized motors on solid supports; consequently, repeated measurements vary in motor number and composition making identification of mechanistic features of collective motility highly impractical and unlikely. However, such reports do serve to bracket expected results for the two-kinesin systems of interest here. Early *in* vitro studies find that when multiple dynein motors work against a load, stall forces for the group may be additive, i.e. two motors can work against twice the force of a single motor, three motors can generate three times the force, etc. (Mallik, 2005). Similarly, forces produced by motor proteins on lipid droplets in early stages of *ex vivo* Drosophila embryo development suggest that as motor number increases stall forces increase linearly (Welte, 1998). These experiments hint that motors are capable of not just working collectively on a cargo, but also cooperating to some degree - producing force with some synchronicity. However, in these and similar studies the number of motors acting on a cargo are not robustly known; the active motor number

producing transport is assumed based on the argument that a particular number of motors would stall at some multiple of the single motor stall force. Again, these types of studies and the assumptions that must be made to formulate interpretations of the data highlight the need for new lines of investigation that overcome the ambiguity of experimental targets.

Multiple-motor studies conducted to date *in vivo* suffer from the same limitations as *in vitro* studies, with the added complication of unknown motor types driving motion. Overcoming these limitations remains exceptionally challenging since methods to resolve the molecular-scale organization of motors when coupled to cargo in living cells have not been established. Bidirectional motion of cargo powered by what were argued to be kinesin-dynein complexes has been observed *in vivo* (Welte, 2004; Kural, 2005); yet, studies such as these that measure motility in living cells have been unable to conclusively comment on the regulation of these types of systems and their dependence on motor number, type, or any other parameters that may be of significance for motility. For example, when bidirectional motion is observed *in vivo* the retention of sequential full ~8 nm step sizes in either direction is offered as evidence that some unknown switching event coordinates the activation/deactivation of certain motors in order to prevent unproductive motor competition (individual motors very often take 8 nm steps, but when multiple cargo-bound motors are interacting with a filament a single motor step should typically produce cargo motions of ~4 nm; Kural, 2005). This interpretation of transport mechanics assumes that motor proteins with opposing polarities drive motility, however, no evidence is provided to demonstrate

motor types bound to cargo surfaces. Such claims cannot rigorously be made when dynein motors are known to make full 8 nm steps in retrograde and anterograde directions. Another study of melanosome transport in xenopus melanophores holds that both kinesin and dynein motors are ubiquitously present on the surface of moving pigment organelles and that control of organelle direction is determined by the regulation of dynein motor activity only (Levi, 2006), however this conclusion is based upon assumptions of unverified models of motor cooperation and no mechanism of such dynein regulation is offered. Furthermore, motility measurements clearly demonstrating instantaneous alternation between positive and negative stepping directions has recently been observed during *in vitro* optical trapping assays on a single cytoplasmic dynein motor (Gennerich, 2007). This finding puts into question many measurements previously attributed to cooperating/competing kinesin-dynein complexes and further demonstrates the need for controlled assemblies of motors with known properties. In general, while observations of complex collective behaviors have led to specific hypotheses regarding mechanisms governing collective cargo motility (Welte, 2004; Kulic, 2008; Levi, 2006), these studies cannot comment conclusively on collective transport mechanisms since fundamental relationships between the structural organization of motors on cargo and the resulting motility are largely unknown. Even basic relationships such as the dependence of collective motor stalling forces on the motor number have not been rigorously established, and more complicated structural features such as mechanical compliances and geometric arrangements of motors have yet to be addressed. As a result, efforts to understand collective motor dynamics in

cells can clearly benefit from the development of detailed structure-function relationships through experiments where the molecular-scale architecture of motor assemblies is unambiguously known, the study described in later chapters addresses these issues through the use of engineered motor assemblies.

1.5.1. Experimental Investigations of Multiple Motor Behaviors Require New Approaches

Even with well-defined complexes of multiple motors, collective transport experiments must still be designed to evaluate whether grouping motors together leads to competition via mutual interference, results in improved but non-cooperative (additive) motor function, or produces enhanced activities through synergistic cooperation. Each of these three types of collective mechanisms should influence motor mechanochemistry, and endow groups of motors with different motile and force-generating properties. However, making these distinctions requires experiments that examine how sharing applied loads affects motor activities at the molecular level. These types of studies will allow fundamental mechanisms of collective motor transport to be established and used to build models of motor regulation in cells that will lead to new links between motor function and diseases.

The study described in later chapters is the first instance where the parameters that define an arrangement of multiple motors on cargo are rigorously known and controlled. This capability offers new opportunities to evaluate collective transport behaviors using 'single-molecule' methods that permit analyses of nanometer-sized

displacements and piconewton-sized forces produced by motor assemblies and, as described in Chapter 4, have led to a theoretical model of collective motor transport that is grounded by experimental multi-motor data. Consequently, this body of work has uniquely addressed the nature of collective interactions within motor assemblies, and in doing so, developed a detailed and comprehensive description of multi-motor function that holds the potential to change interpretations of a broad range of cellular processes.

1.6. The Mechanisms that Govern and Modulate Intracellular Transport are Not Well Known

Throughout the lifecycle of a cell there are time-dependent transportation needs that must be met. A means of regulating motor-dependent transportation of cargos during these varying cell cycles is required for proper cell function. Motors must recruit the appropriate cargo at the proper time and also release them when their destination is reached. Autoinhibition of cargo-detached kinesins is thought to play a critical role in regulation mechanisms (Dietrich, 2008; Wong, 2009; Hammond, 2009), yet this mechanism alone cannot account for the diversity of transport activities observed. Early theories of directional transport regulation posed that sets of surface determinants on cargos change dynamically and are responsible for binding varying motors when particular transportation is required (Fahim, 1985). This proposal was supported by observations of foreign polystyrene beads and purified synaptic vesicles moving preferentially in one direction when injected into a cell (Adams, 1983; Schroer, 1985);

such artificial cargos present static surface chemistries which would be expected to generate motion in one direction only if surface chemistry is the determinant of cargo trafficking. Electron microscopy studies of motor-driven transportation in neurons also showed that free motors are preferentially bound to the surfaces of vesicles rather than binding sites on microtubules (Miller, 1985), again giving credence to a mechanism of motor regulation directed by surface determinants on cargos. Phosphorylation of kinesin and dynein (or of associated protein complexes) has also been implicated in transport regulation by altering cargo specificity and/or motor activity (Lee, 1995). Indeed phosphorylation of certain kinesin complexes (KIF5-KLC) has been shown to inhibit association with synaptic vesicles (Sato-Yoshitake, 1992) and membrane organelles (Morifini, 2002). Tau, a particular microtubule-associated protein (MAP), can affect motility characteristics such as run lengths and motile forces of kinesin motor proteins *in vitro* (Vershinin, 2007). In neurons where Tau is over-expressed, mitochondria organelles no longer reach the periphery of cells by a potential inhibition of plus-ended kinesin-like motor proteins (Ebneth, 2006). Both Tau and MAP2c are capable of reducing the attachment rate of motors to microtubule tracks (Seitz, 2002). Although microtubule-associated proteins cause these various effects, the number of microtubule-bound motors is the underlying mechanism for the observed changes in motility. Still, how the activity of motor proteins is related to the spatiotemporal-dependent transport of cellular contents remains unclear. Even so, these theories of intracellular motor protein regulation center on the binding characteristics between motors and their cytoskeletal tracks, i.e. modulation of total motor number, further

demonstrating the need for accurate knowledge of multiple-motor motility characteristics and the parameters that govern them.

Over the last decade many advances have been made in understanding the mechanisms by which motors may bind to cargos, yet the exact method by which these binding motifs might regulate cell-wide behaviors is still not well understood. It has been proposed that c-Jun N-terminal kinases (JNKs) can phosphorylate KIF5 motors to make microtubule-motor interactions weaker (Morfini, 2006; Stagi, 2006) and conversely phosphorylation has also been shown to up-regulate motor-dependent axonal transport in *C. elegans* and *D. melanogaster* (Byrd, 2001; Horiuchi, 2007). Alternatively, it has been suggested that the distribution of organelles is controlled through a family of Rab GTPases that are hypothesized to differentially bind motor proteins when in GTP and GDP bound states (Zerial, 2001). Changes in the number of motors driving motility are intrinsic to a surface determinant view of regulation and highlight the need for studies of multiple motor assemblies. Whatever the outcome of studies that question which cargo-surface determinants recruit motor proteins to affect intracellular transport, the underlying dynamics of multiple-motor systems remain the same. The two-kinesin systems analyzed in later chapters reveal behaviors that form a foundation upon which downstream regulatory mechanisms (e.g. cargo-binding determinants) must operate.

1.7. The Study of Multiple-Motor-Driven Motility is Medically Motivated by the Role of Intracellular Transport Dysfunction in Human Diseases

Over the last decade many higher-order physiological functions have highlighted the importance of intracellular transport. Animal models in mice have shown motors play a critical role in early stages of life during left-right body determination (Nonaka, 1998, Takeda, 1999; Marszalek, 1999). Certain kinesin motor complexes also have an established role in tumor suppression (Teng, 2005) and regulation of neuronal morphology (brain wiring; Homma, 2003). And, amazingly, recent studies of transgenic mouse strains that overexpress particular motor complexes have demonstrated improved working and spatial memories (Wong, 2002), suggesting a critical role for motor proteins in memory and learning!

Regularly functioning motor protein machinery is critical to normal cell physiology, loss or inhibition of these motors can lead to severe defects in cellular function. While malfunction of these essential processes can lead to a variety of diseases and disorders, neurons are known to be particularly susceptible to defects in motor transport. This enhanced sensitivity is a result of neuronal structure; their long cytoplasmic extensions (Grafstein, 1980) demand active motor-driven transport for normal operation. Consequently, motor protein function has been identified as a critical factor in the onset of many neurological diseases. For example, mutations of the kinesin motor have been shown to disrupt axonal transport leading to impaired function

reminiscent of vertebrate motor neuron disease (Hurd, 1996). KIF5A (a particular kinesin heavy chain found only in neuronal tissues) is defective in a form of hereditary spastic paraplegia in humans (Reid, 2002). Abnormal neurofilament accumulations are observed in the cell bodies of mice neurons lacking the KIF5A kinesin heavy chain (Xia, 2003), a primary component of the so called "slow axonal transport" machinery, and these accumulations are strikingly similar to those observed in other neurodegenerative diseases, such as amyotrophic lateral sclerosis, Parkinson's disease, and Alzheimer's disease (Julien, 1998; Julien 1999). Neurofilament transport along axons is also important in regulating axon diameter; when neurofilaments aggregate in the cell body due to a malfunctioning motor protein transport system axonal degradation is observed, such degradation is a hallmark of symmetrical sensory polyneuropathy, the most common form of diabetic neuropathy in humans (Zochodne, 1996), suggesting kinesin defects or deficiencies as a potential mechanism for the disease. Further, reductions in motor-protein-mediated transport are believed to stimulate proteolytic processing of the β-amyloid precursor protein, resulting in the development of senile plaques and Alzheimer's disease (Goldstein, 2001; Stokin, 2005). The study described in later chapters has characterized the motile properties of two-kinesin assemblies and set a foundation for discovery and understanding of the form-function rules that govern multiple-motor function. Armed with an understanding of multi-motor dynamics the behaviors observed in dysfunctional modes of transport leading to diseased states may be decoded to improve mechanistic interpretations of disease pathology.

Even with established connections between motor transport and neurological diseases, it remains unclear whether aberrant motor transport either triggers or stems from such illnesses. Resolving the role of motor proteins in neurodegenerative disease pathologies ultimately requires detailed knowledge of the regulatory mechanisms that modulate motor protein activities in cells, and an understanding of whether diseases arise from a breakdown in motor regulation, recruitment, or perhaps the motors themselves. However, while there are many potential levels of motor regulation that may occur (e.g. through phosphorylation, binding of Rab GTPases, etc.), any cellular regulatory mechanism must operate downstream of the intrinsic behaviors of motor protein groups. Yet, to date, a foundational understanding of collective motor function has been elusive. While single-motor biophysics has been extensively studied *in vitro*, the characteristic behaviors of motor groups have not been determined experimentally. Without general knowledge of how motor number and/or assembly architecture can affect intracellular transport properties the fundamental principles governing motor regulation in cells may remain largely unknown. The studies described here directly address these specific transport issues, and in doing so, provide new guidelines to interpret mechanisms that regulate intracellular cargo transport. Accordingly, this work has formed an important foundation to better understand how multiple motors drive transport in cells and can yield insight into how compromised motor protein activities can lead to diseased cellular states.

Summary of Chapter 1

Microtubule motor proteins are the driving force behind many intracellular transport processes and as a consequence their activities affect functions at molecular, cellular, and organism-level scales. Nevertheless, the regulatory mechanisms that control how, when, and where motors perform their transport duties is unknown. Regulatory control may occur on a level intrinsic to motor protein groups and/or at higher-levels by adapter proteins, kinases, non-motile microtubule-associated proteins, etc. Still, regulatory mechanisms that are intrinsic to motor groups have not been explored due to existing limitations in probing the dynamics of multiple-motor systems.

Optical trapping instruments have been a key tool in dissecting motor mechanochemistry at the single-motor level. However, mechanistic understanding of multi-motor protein assembly transport processes still requires the development of new techniques to organize, define, and characterize the structure and dynamic functions of motor systems. Given that aberrant motor transport has been implicated in the pathogenesis of many diseases, and in particular a variety of neurological disorders, such efforts may also serve to advance the development of therapies for motor-related diseases, while providing a framework to understand how motors function together in cell to drive cargo motion.

Chapter 2

Construction and Design of an Optical Trapping Microscope for Fast, Nano-Scale Measurements of Multiple Motor Protein Dynamics

Optical trapping experiments of multi-motor protein complexes can benefit from conducting transport dynamics in both static and force-feedback modes. In a static trap, the infrared trapping laser light remains stationary during data collection. A static trap is well-suited to measure the force production capabilities of motor protein systems under a non-steady-state increasing load and is a convenient method to quickly probe motor behaviors in many force regimes. In force-feedback mode the position of the optical trap is actively controlled to remain a fixed distance trailing behind the position of a transported microsphere. Because the trap applies forces as a function of the trapped particle's distance from the laser focus maintenance of a fixed trailing distance

effectively applies a constant rearward force to the trapped particle and the attached motor protein system. In feedback mode, transport velocities, run lengths, and dwell times, etc. can be measured over a detailed range of loading forces under near-steady-state conditions. Together static and feedback trapping modes provide the tools to probe the complex and nuanced transport capabilities of single and two-kinesin systems. The instrument described in this chapter was tailored for investigations of multiple motor proteins and can be operated in static or force feedback trapping modes while offering the ability to detect sub-nanometer displacements of microspheres with sub-millisecond time resolution.

2.1. Optical Trap Construction and Design

Kinesin motor proteins take characteristic 8 nm steps during intracellular transport, and as we will see in later chapters, multi-motor assemblies often displace cargos by only a nanometer or two as one motor within assembly steps independently. Measurements of motor motility are therefore inherently on the nano-scale and require sensitive instrumentation to track the detailed motions of transported cargos. To investigate the motility of two-kinesin systems an optical trap outfitted with single-molecule fluorescence capabilities and back-focal-plane detection systems will be utilized (a highly simplified schematic of the optical trap showing representative optics and their layout is given in Figure 2.1).

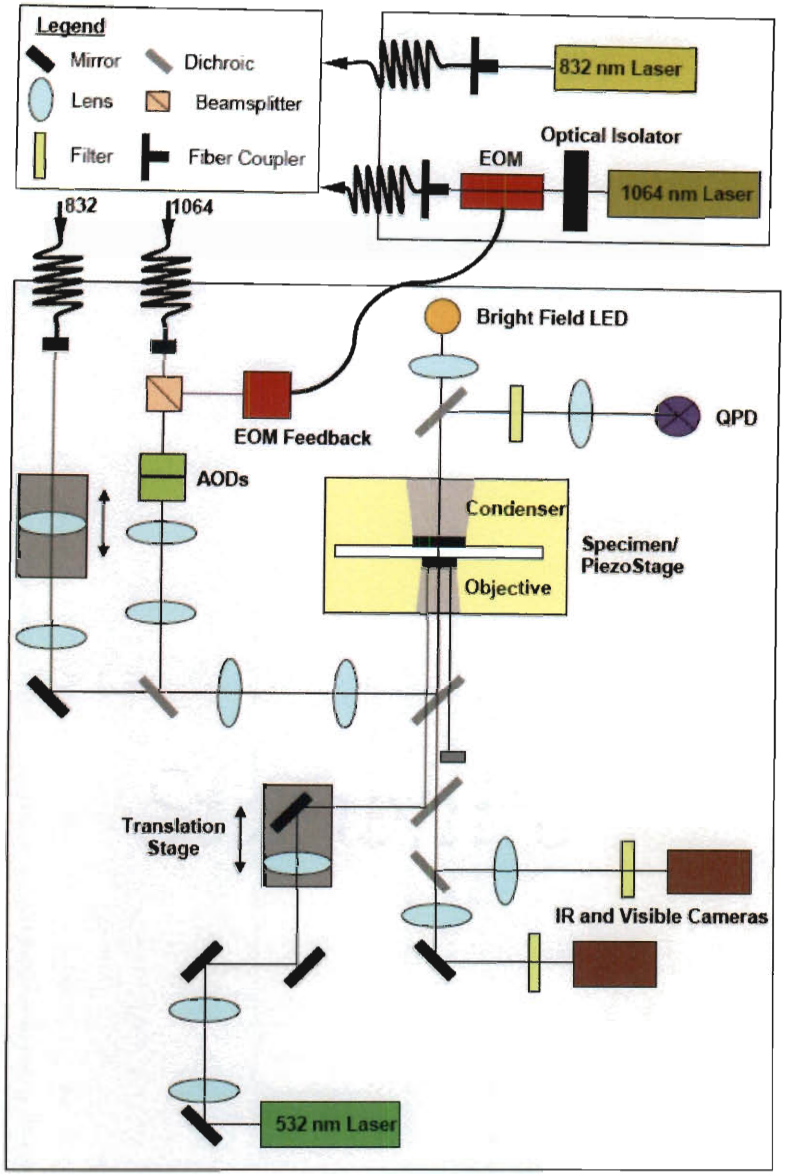

Figure 2.1: Simplified Schematic of the Optical Trapping Instrument

This instrument is based upon an extensively modified Nikon TE2000 microscope; custom brackets, mounts, and stages have been integrated throughout the design of the instrument for increased structural rigidity, modularity of optics and suppression of

resonant structural frequencies. The optical trap itself is created by tightly focusing expanded 1064 nm Nd:YVO_4 laser light (Spectra Physics) using a 100x 1.4 NA Nikon objective. Optical trap steering (and dynamic feedback mode forces) is accomplished through the use of a two-axis acousto-optic modulator (AOM; IntraAction Corp.) placed, along with many other critical optics, in conjugate planes to the specimen plane such that the changes in laser angle accomplished through diffraction at the AODs results in pure translational motion of the trapping laser focus at the specimen plane. A second infrared laser (830 nm; Point Source) is used for measuring bead displacements with nanometer precision in a back-focal-plane detection system (BFPDS) configuration. In this system, 830 nm laser deflections from motor-generated motions of trapped microspheres can be detected at ~100 kHz bandwidth (Peterman, 2003) by imaging of the beam onto a large-area quadrant photodetector (QPD, Electro-Optical Systems; for a detailed description of this detection system see Gittes, 1998). The near-infrared laser wavelengths used here are common in biological trapping applications (Svoboda, 1994), chosen for their overall low potential for causing photodamage (Ashkin, 1987). Microscopes slides are mounted upon a three-axis nano-metric piezo stage (Physik Instrumente) used to translate samples with sub-nanometer accuracy, allowing for various calibration and automation routines. All lasers are also equipped with shuttering control. Fluorescence excitation is accomplished by a 532 nm diode-pumped solid state laser (Intelite). The fluorescence excitation path is switchable between epi-fluorescence and total internal reflection configurations; fluorescence emission is detected by an electron-multiplying CCD camera (Andor). The instrument described

here is by design highly modular and capable of a broad range of experiments that probe the influence of force on multi-motor protein dynamics.

Particular attention was given to sources of positional noise. Acoustic disturbances, air currents and particulates, vibrations, and temperature variations can all manifest themselves sources of noise in nanometer-scale position detection signals while also being problematic for long-term alignment and optimization of microscope optics. To alleviate these problems fiberglass acoustic treatments have been installed to reduce acoustic noise within the trapping room, air filtering equipment actively generates clean-room conditions, and both passive and active vibration isolation tables separate optics from ground vibrations. Microscope components are also housed within sealed boxes to quell stray air currents while sheltering optics that would otherwise be exposed. These combinations of techniques have produced an extremely stable instrument from which the study of motor motility can be performed. Stage drift as measured by detection of coverslip-fixed 0.5 micron diameter microsphere motions is < 5 nm/minute; the stage is held within a ±10 nm window over a time span of thirty minutes. Position of the optical trap focus is also strictly maintained, measured drift is < 1 nm/minute. Measurements of motor protein motility occur over only a few seconds (motor transport events are force-dependent, but most transpire in approximately 0.5 second); the effect of instrumental drift in these experiments is therefore negligible. To prove the ability of the system to measure cargo displacements on the nano-scale, fixed beads were stepped in one nanometer increments by the piezo-stage. Figure 2.2 demonstrates the ability to detect these one nanometer displacements, and

demonstrates that with fast data collection and averaging sub-nanometer events can also be resolved (data was collected at 30 kHz and averaged to 100 Hz).

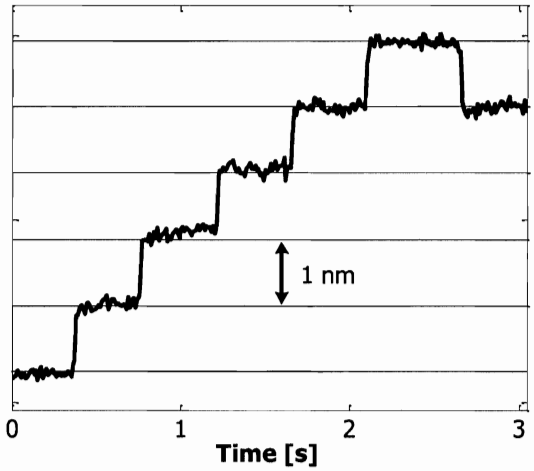

Figure 2.2: One Nanometer Microsphere Displacements Measured by the BFPDS

The force exerted on a particle within the optical trap is linearly dependent upon the laser power of the trapping beam (Svoboda, 1994). Experiments probing the motility of coupled two-kinesin assemblies will be explored over a biologically significant range of load forces induced by the optical trap (0 – 15 pN). It is therefore crucial for the trapping laser power to remain as stable as possible throughout the duration of motility experiments to avoid changes in force production by laser power fluctuations. To this end an electro-optic modulator (Conoptics, Inc.) running in a feedback loop is used to quiet power fluctuations originating from the laser head itself as well as transient changes in fiber coupling efficiency improving power noise from ~ 3.0 % RMS to < 0.20 % RMS. Because the optical trap produces forces as a function of distance from the trap center, uncontrolled positional variations of the trap center can bring

about unwanted fluctuations in the force applied to motor protein systems. Positional variations of the trap originate from vibrations and thermally-induced movements of optics as well as pointing instabilities inherent to the laser head. Both the trapping and detection laser are fiber-coupled to reduce pointing instabilities and the use of single-mode fibers also has the added benefit of cleaning laser mode structure, although this is at the expense of increasing the sensitivity of fiber coupling alignment and the corresponding sensitivity to power fluctuations. The TEM_{00} Gaussian-profile beams that exit the fibers produce high intensity laser light gradients that are desirable and necessary for optical trapping. Attention was also given to the optical mapping of essential components within the optical train. For example, the trapping laser source is located within a plane optically conjugate to the fiber coupler such that angular pointing variations at the source become variations in laser angle when entering the fiber and not translational motions across the fiber-end which would generate large losses in coupling efficiency and laser power causing fluctuations in applied trapping forces.

2.2. Application of Known Optical Forces to Motor Protein Systems

To apply defined forces to trapped microspheres it is necessary to know both the stiffness, k, of an optical trap and displacements from the optical axis, x, with nanometer accuracy to satisfy the trap force equation $F = kx$. Theoretical models exist to calculate the stiffness of an optical trap given a particular laser power, index of refraction for the suspending medium, and polarizability of the dielectric particle (Gordon, 1973). These models are applicable for ray optics approaches (Ashkin, 1992) -

when the trapped dielectric is much larger than the trapping light wavelength, the Rayleigh regime - when the dielectric is much smaller than the trapping light (Visscher, 1992), and in the intermediate region, when light wavelength is on the same scale as the trapped dielectric particle where electromagnetic theory has been applied (Barton, 1988; Rohrbach, 2001). However, despite these theories measurements of trap stiffness have not reliably coincided with predicted values. For this reason determination of trap stiffness must be accomplished empirically.

2.2.1. Determination of the Optical Trap Stiffness

Two approaches of stiffness calculation have been employed here, known as the power spectrum and equipartition theorem methods. The equation of motion for a trapped particle within a harmonic potential subjected to thermal forces can be calculated exactly; the dynamics of this system are given by a Lorentzian power spectrum (Wang, 1945) which describes Brownian motion within a parabolic potential well. The corner frequency of this spectrum, f_c, can be directly related to trap stiffness by the equation, $f_c = k(2\pi\beta)^{-1}$, where β represents the drag constant (Tolic-Norrelykke, 2006), and 'k' is the trap stiffness. In Figure 2.3, the power spectrum of thermally driven motions of a trapped particle (red data) detected with the BFPDS is fitted to a Lorentzian equation (blue curve) to yield a measurement of trap stiffness.

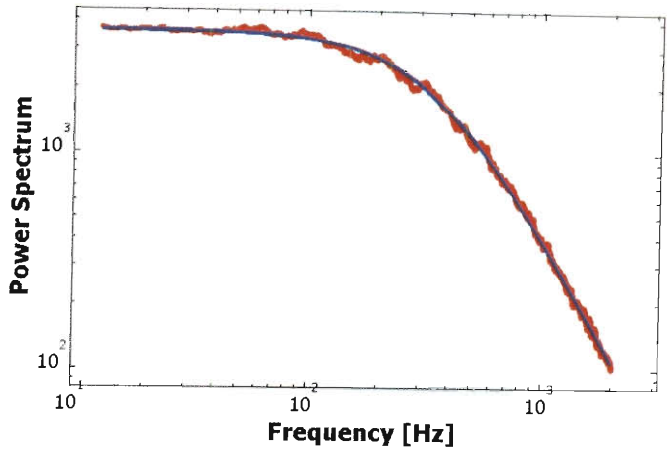

Figure 2.3: Trap Stiffness is Determined by Fitting a Lorentzian Equation to a Power Spectrum of Microsphere Motions

For the second method of trap stiffness calculation, the equipartition theorem assumes that in thermal equilibrium, potential energy of the trapped particle is equal to thermal energy, yielding the equation, $\langle x^2 \rangle = k_B T k^{-1}$, relating displacement of the particle, x, to temperature, T, the Boltzmann constant, k_B, and trap stiffness, k. The power spectrum and equipartition methods of calibration rely on different assumptions, giving to each its own advantage. When drag force can be readily measured as is the case for a spherical object, the power spectrum method gives accurate stiffness measurements (the solution to the equations of motion on which the power spectrum method relies is dependent on the ability to accurately measure the drag force on the trapped particle), with the added benefit that absolute calibration of the position detection system is unnecessary; the corner frequency of the power spectrum does not dependent on absolute measurements of particle displacement since it is based solely on the frequency information within the position fluctuation data. The equipartition method

conversely is independent of drag calculations, but is quadratically dependent upon absolute distance measurements. Simultaneous agreement in stiffness calculations between the two methods gives confidence in the accuracy of stiffness determination. However, in practice, the power spectrum method has proven to be far more reliable than the equipartition method; repeated power spectrum stiffness calibrations show agreement in calculated stiffness <± 1%, while equipartition-calculated stiffnesses often vary ± 10%. Consequently, for the experiments described in later chapters the power spectrum method alone was used to measure the stiffness of the optical trap.

2.2.2. Characterizing the Non-Linear Force Profile of an Optical Trap

While the force profile of an optical trap can be approximated by the equation for a linear spring, F = kx, this simplification is only valid for small lateral displacements from the center of the trap. For assays that require large force production or large displacements from the center of the trap a better characterization of the nonlinear force profile of the optical trap is often beneficial (see Figure 2.4). This characterization is also advantageous for application of forces when the trap is in force-feedback (force clamp) mode. In this mode, automated AODs actively position the trapping laser a set distance behind a target trapping particle to impose a constant load. If the trailing distance set point is selected near the maxima of the nonlinear force profile of the trap, constant loads are imposed with less force noise arising from positional error (see Figure 2.5).

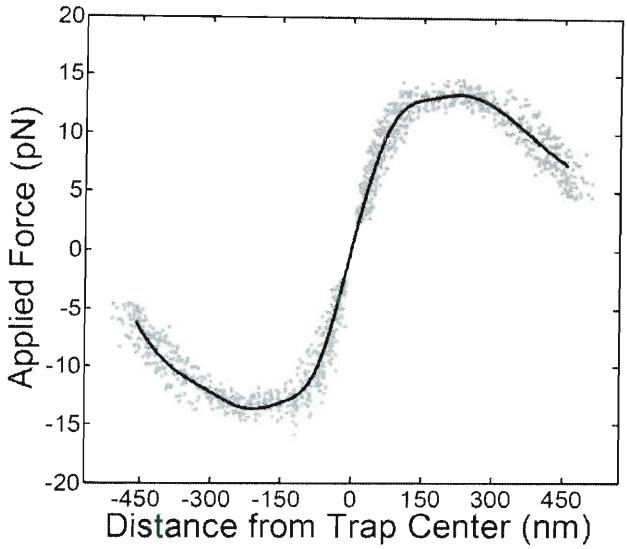

Figure 2.4: Measuring the Non-Linear Force Profile of an Optical Trap

The optical trapping force is given as a function of distance from the center of the trap. Similar to previous studies (Simmons, 1996), the force profile of the optical trap was calculated from the Stokes drag that arises as a trapped bead is drawn into an instantaneously displaced trap center (grey dots). The average of the experimental data is given by the solid black line. The absolute force exerted by the trap scales linearly with the laser power of the trapping beam. Trap stiffnesses determined experimentally by the power spectrum method approximate the linear range of this force profile at small displacements from the trap center.

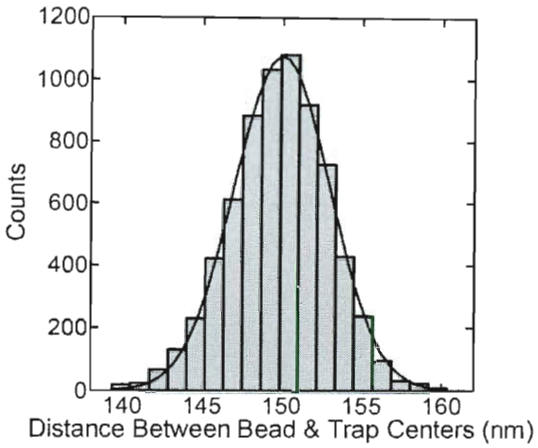

Figure 2.5: A Measure of Force Noise in the Optical Force Clamp

When the optical trap is in force clamp mode the desired applied force is achieved through a combination of optical trapping laser power (trap stiffness) and offset distance (distance between trap and target particle). Here, an offset distance of 150 nm was chosen (near the maxima of the trap's nonlinear force profile, see Figure 2.4) and the experimentally measured positional difference between the target and the trap is given as a histogram (i.e., the target is a bead with surface-bound kinesin walking along a microtubule filament, see Figure 5.3 for an example force clamp trace). The data is fit to a Gaussian function with a standard deviation of 3 nm. Therefore, at a common trap stiffness of 0.06 pN/nm, the optical trapping feedback routines produce a constant force of 9 ± 0.05 pN.

2.3. Calibration and Use of a Back-Focal-Plane Detection System

Optimization of the back-focal-plane detection system is the first step to obtaining reliable displacement data needed to apply known forces to motor systems. Included within the 830 nm detection laser beam path is a manual steering lens optically mapped such that translations of the lens allows sensitive placement of the detection laser focus relative to the optical trap center in three dimensions. Positioning of the 830 nm focus along the optical axis tunes sensitivity of the BFPDS; it alters how detection light strikes trapped particles as well as the lensing affect the particle has upon forward scattered light. XY positioning of the detection laser focus is crucial to obtain detection and trapping beams with a common axis. In this aligned configuration crosstalk in displacement measurements (XY signals generated by vertical microsphere motions – along the optical axis) is minimized; crosstalk in this system is measured as < 3% across the detection range.

Calibration of the detection system is accomplished in three steps. First, a one-time EMCCD camera pixel calibration is performed by fixing a fluorescent microsphere to the microscope coverslip surface and translating the bead known distances with the piezo-stage (the piezo stage is calibrated to specifications that demand nanometer accuracy in translations). Fluorescent signals from the microsphere are fit to two-dimensional Gaussian distributions to precisely localize the bead center. This computational approach, known as centroid fitting, has been shown to localize quantum dots with a precision of 1.5 nm in biological applications (Nan, 2005). Second, a trapped

fluorescent microsphere is shifted through solution by altering the AOD-driving sound frequency through equal intervals. Images of the fluorescent signal are again fit and demonstrate a linear relationship between sound frequency and position. These two processes provide a means to move trapped microspheres known distances on the nanometer scale by altering AOD driving signals. The last step in position calibration relates quadrant photodiode voltage signals to nanometer bead displacement through an automated AOD rastering scan of trapped microspheres containing bound motor protein complexes during motility assays (see Figure 2.6a; a top view of the rastering procedure displays the raster path (blue line), pause positions (blue dots), and a representative usable detection region (red circles)). This real-time calibration procedure allows subtle differences in position signals caused by slight microsphere variations, immersion oil and slide inconsistencies, and other day-to-day variables to be accounted. Data resulting from this rastering procedure is given in Figure 2.6b, which displays the QPD calibration curve for the y-direction. The calibration curve has many interesting features. When a trapped bead is centered in the x-direction (x=0), translations in the y-direction produce a pure near-linear y-response in the QPD signal, however, when a trapped bead is not at x=0 and y=0, x-translations are also capable of producing a QPD signal in the y-direction. For the special case of force-feedback experimentation, real-time calibration curves are fitted to fifth-order polynomials in two variables so that fast voltage-to-position transformations can be performed in order to drive dynamic positioning of the optical trap when the trap is operating in force-feedback mode.

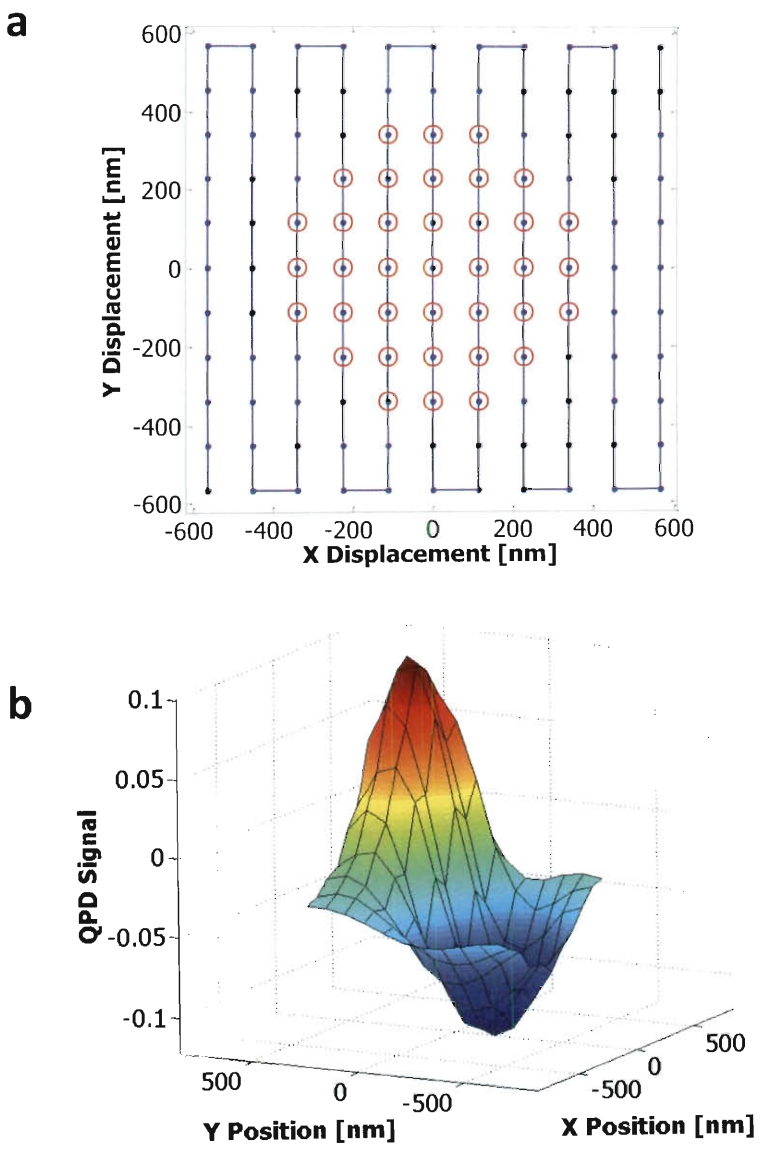

Figure 2.6: Calibration of the Back Focal Plane Detection System is Performed on Each Bead

2.4. Automation of Motility Assays

To standardize and expedite motility assays a series of LabView automation routines have been implemented. Careful positioning of trapped polystyrene beads above surface-bound microtubules and axonemes is advantageous to initiate motility events in a uniform manner. To this end, coverslip surface and microtubule/axonemes finding programs have been written. Bead height from the surface and lateral distance from the filament axis determine the off-axis forces experienced by transporting motors, therefore, automation routines that produce repeatable positioning of trapped microspheres help to provide a much more uniform set of motor assemblies for measurements. To find the surface, a trapped microsphere is manually brought near the coverslip through adjustment of objective height. The piezo-stage is then incrementally raised toward the microsphere; the surface ultimately pushes the bead away from its trapped equilibrium position changing the detection laser beam path and creating a measurable shift in the total light reaching the quadrant photodiode. Data from this surface-finding routine is given in Figure 2.7a, two lines (blue) are fit to the data corresponding to stage heights (black) before and after the bead interacts with the surface; their point of intersection locates the surface (dashed red line). Repeatability of this algorithm is within ±10 nm, far beyond what can be achieved by manual positioning of the objective or manual use of the piezo stage.

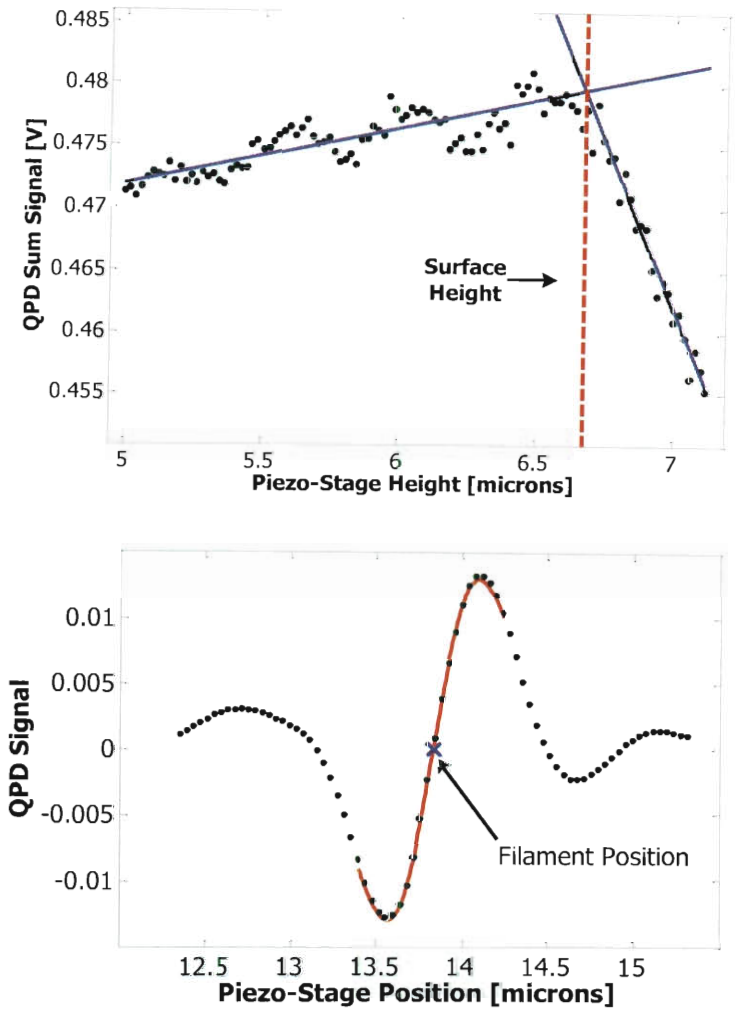

Figure 2.7: Automation Routine Data for Localization of Coverslip Surface Height and Filament Axis Position

To find the lateral position of microtubules and axonemes, filaments are scanned across the detection beam using the piezo-stage. As the microtubule or axoneme traverses the laser focus a shadow is cast upon the quadrant photodetector. The data collected from this type of scan (black) is given in Figure 2.7b and can be fit to the derivative of a Gaussian function (red); one of the fitting parameters corresponds to the center of the distribution and physically to the longitudinal axis of the filament (blue cross). This filament-finding approach locates microtubule and axoneme axes to within 5 nm repeatability. The combination of these surface and filament-finding tools allows for extreme precision in the initiation of motility assays. Additionally, a host of LabView tools have been developed to provide software control over equipment yielding laser shuttering, bright-field illumination, data acquisition parameterization and buffering, as well as other controls.

The instrument described above has provided a platform for detailed study of the transport dynamics of multiple motor protein systems. Great care was taken throughout construction to build a system as free from sources of noise as possible. Multi-motor assemblies display critical behaviors on length and times scales that demand sophisticated techniques for observation. Without the use of an optical trapping microscope that meets stringent performance specifications many aspects of collective motor transport could not have been surveyed. In the following chapters, the first measurements of multiple motor proteins with a known number and geometry are described. The use of this optical trap has revealed many multi-motor behaviors that

have the potential to drastically alter our understanding of intracellular transport as well as any other cellular process that utilizes many motors at the same time.

Summary of Chapter 2

This chapter describes the construction and design of an optical trapping instrument built to measure the dynamic behaviors of multiple-motor protein systems. The components of the trapping instrument chosen to address design criteria which require the ability to apply piconewton-scale forces and detect nanometer-scale motions on a millisecond time-scale are discussed. Because motor proteins operate on these small length and time scales special attention was given during the instrument design to avoid and/or reduce sources of noise. The positional detection limitations of the instrument and the methods used to calibrate the force application capabilities of the optical trap in both static and force-clamp modes are also presented. Further, software-based automation routines are described that perform calibrations and ensure consistency in the set-up of experimental assays.

Chapter 3

Two Kinesins Transport Cargo Primarily via the Action of One Motor

Microtubule motors are mechano-chemical enzymes that transport organelles and other important cargos in the cytoplasm of eukaryotic cells (Howard, 2001). Many motors in the kinesin and dynein families are capable of generating piconewton-sized forces while moving processively along their filament tracks (Carter and Cross, 2005; Hancock and Howard, 1999; Schnitzer et al., 2000). Although these properties imply that a variety of motors should be capable of transporting cargos as single unassisted molecules, cryoelectron microscopy and several *in vivo* studies have demonstrated that cargo motion is often driven by multiple kinesins and/or dyneins (Gennerich and Schild, 2006; Hirokawa, 1998; Kulic et al., 2008; Soppina et al., 2009). The combined action of motors is critical during specific transport challenges that require high-force production or long-distance travel. Other lines of evidence suggest that cargo motion can also be regulated by tuning the number of motors participating in transport (Levi et al., 2006).

The motions of neurofilaments, mitochondria, melanosomes, and certain vesicles are all known to be driven by both kinesin and dynein. Since these motors move in opposite directions along microtubules, regulating their stoichiometry should allow net directional transport to be achieved. However, despite increasing efforts to examine multiple motor behaviors, the sensitivity of most cargo transport parameters to motor copy number has been difficult to characterize, and overall, the precise impact of motor number on intracellular transport processes remains unclear.

A significant limitation of current studies of multiple motor dynamics is that the number of motors responsible for cargo motion is not rigorously known. Typically, only the average number of motors on cargos can be controlled *in vitro*, while the actual number on individual cargos is distributed across a range of values. Analogously, motor number can be manipulated *in vivo* by either stimulating cells with external cues (Levi et al., 2006) or controlling motor expression (Shubeita et al., 2008). In all of these cases, the precise number of motors responsible for specific transport behaviors must be determined from analyses of cargo velocities, run lengths, and detachment forces. Yet, the relationships required for such inferences have not been rigorously validated, and are commonly based on idealized model behaviors that do not account for how motors are arranged on their cargo or whether they interact with one another.

Understanding the effects of multiple motor organization and coupling is particularly important considering motor copy number has been found to influence cargo transport differently *in vitro* and *in vivo*. Despite reports of significantly different

average run lengths, beads coated with multiple motors are generally found to travel longer distances along microtubules than single motor molecules (Beeg et al., 2008; Vershinin et al., 2007). Such behavior is not necessarily found *in vivo*. Recent *in vivo* studies of lipid droplet motility suggest that cargo velocities and run lengths do not depend on kinesin copy number (Shubeita et al., 2008). Interestingly, bidirectional motions of melanosomes, and hence whether they aggregate or disperse in the cytoplasm, appear to depend on dynein, but not kinesin number (Levi et al., 2006). Given current *in vitro* observations and general notions of multiple motor mechanics, it has been suggested that there are yet undefined environmental and/or regulatory factors in living cells that reduce the impact of kinesin copy number on cargo transport. However, since critical aspects of collective motor mechanics remain unresolved, one cannot rule out the possibility that such behavior stems from inherent biophysical properties of multiple kinesin complexes.

In the experiments described below an optical trap was used to characterize the load-dependent transport properties of structurally-defined motor assemblies containing two elastically-coupled kinesin-1 molecules. These assemblies facilitate direct comparisons of multiple motor behaviors to those of single kinesin molecules, and allow examination of how a motor assembly's microtubule-bound configuration and motor number influences cargo motion. Overall, we show that single and small groups of kinesins exhibit remarkably similar detachment forces, velocities, and bead displacement sizes *on average*. Such behavior appears to stem from the fact that most microtubule-bound configurations of the motor system (1) prevent both kinesins from

participating simultaneously in cargo transport (due to an intrinsic difficultly with load-sharing) and (2) create conditions that promote detachment of the leading (*front*) motor within the assembly. Consequently, the net load-dependent transport properties of two-kinesin systems resemble the action of a single kinesin molecule much more than have ever been expected. Furthermore, the conditions that influence this behavior appear to be generic and should apply to a range of intracellular cargos and motor types. Thus, kinesin-dependent transport processes demonstrate behaviors that shown them to be intrinsically insensitive to kinesin number.

3.1. Engineered Multiple-Motor Systems are Needed to Investigate Intracellular Transport Dynamics

The study of multiple-motor motility requires strict control over motor assemblies. To accurately emulate multiple-motor systems as they exist within the cell, in groups ranging from 1 – 5 motors (Miller, 1985), it is of foremost importance to first have direct control over the number of motors within an engineered motor assembly. A two-motor kinesin system is a natural choice for initial studies and will serve as an appropriate test-bed to discover and interpret the form-function rules that govern multiple-motor modes of transport. Beyond a well-defined motor number it is important to have control over inter-motor spacing to produce a geometrically consistent system for study while preventing unwanted steric interference between motors from affecting transport activity (Lipowsky, 2001). The effects of molecular crowding have been observed in microtubule gliding assays where gliding velocities are

reduced 35% when kinesin motors are densely packed onto coverslip surfaces (Bohm, 2000). In cells, motor assemblies carry a wide range of cargos that have intrinsic variety in their mechanical properties. When motors transport soft-condensed materials such as vesicles and other macromolecular complexes within the cell; they are physically connected to each other by way of an elastic linkage defined by the material properties of the transported cargo (Duke, 2000). Consequently, within these engineered motor assemblies the elastic linkage between the motor protein and molecular scaffold must be well defined and controllably variable over a range of stiffnesses to represent transportation of various cellular cargos. Through a combination of several synthetic strategies and techniques (described in Section 3.2) DNA molecular scaffolds designed for this study have yielded the capability to dictate motor number as well as motor-motor spacing and elasticity, providing an amazingly versatile platform from which multiple-motor transport and the effects of inter-motor properties can be studied at the single assembly level through the use of single-molecule microscopy techniques. While several techniques to immobilize proteins onto DNA structures have been previously established, including streptavidin-biotin interactions (Yan, 2003; Niemeyer, 1994, 1999), covalent linkages to DNA (Lovrinovic, 2005), and aptamer-directed binding (Liu, 2005), the combination of physical criteria required to emulate motor protein systems (as described above) called for a new protein immobilization technique to be developed.

3.2. Synthesis of Two-Kinesin Systems

The entire two-kinesin system consists of three parts: a molecular DNA scaffold, an artificial protein DNA conjugate linker molecule, and genetically engineered truncated kinesin motors with structural motifs for chemical attachment (see Figure 3.1).

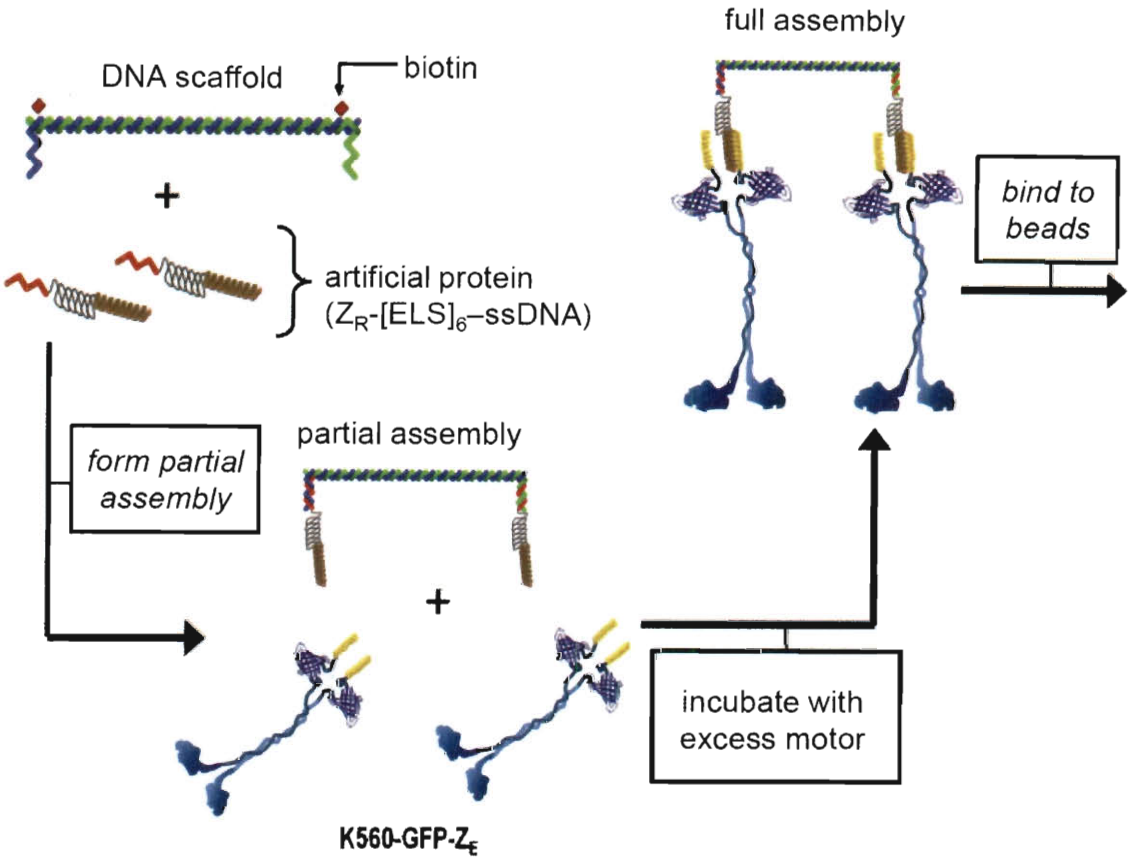

Figure 3.1: Synthetic Scheme Depicting the Formation of Partial and Full Two-Kinesin Assemblies

The molecular scaffold developed for this study is built upon a straight DNA duplex "backbone" with two single-stranded "over-hang" regions located at its ends. Because

DNA has a relatively large persistence length, roughly 50 nm, it is an appropriate system from which to construct a scaffold of sufficient length to separate two kinesin motors, each ranging in length from 10 – 30 nm depending on the portion of the stalk region that is retained, and pattern them onto the surface of a microsphere. Unhybridized DNA over-hang regions of the scaffold have unique twenty base sequences that serve as independent attachment points with a high specificity for their complementary DNA sequence. Any molecular system can be attached to the scaffold by inclusion of DNA sequences complementary to the scaffold over-hangs. Due to the helical structure of DNA, whole turns of the helix are used as the body of the scaffold to ensure that overhang points of attachment lie within the same plane (i.e. attached motor proteins will project from the scaffold body in the same direction, aiding in simultaneous microtubule binding and active force production for transport). The ends of the DNA scaffold are labeled with biotin, acting as binding sites for the entire scaffold-linker-motor structure (each motor is anchored to the microsphere by its nearest biotin-streptavidin-biotin complex). Fluorescent markers can also be localized to the scaffold ends, and through single molecule fluorescence microscopy techniques end-to-end length measurements of scaffolds have been confirmed.

Tunable elasticity can be introduced into the system by inclusion of an artificial protein based on a poly(VPGV$_{\alpha}$G) structural motif of the protein elastin (Urry, 1997). This motif has well defined elastic properties that can be altered through changes in either domain length, amino acid sequence, or both (Urry, 2002). Formation of the DNA-artificial protein conjugate (which acts as the linker molecule between the kinesin

motor and the DNA scaffold) is prepared by genetically engineering a single cysteine residue at either terminus of the elastin motif, $(ELS)_6$, (depending on whether an N- or C-terminal motor is desired) and then covalently attaching single-stranded DNA using heterobifunctional sSMCC labeling chemistry (Kukolka, 2004); the single-stranded piece of DNA confers specific attachment of the motor-DNA-artificial protein complex to the overhang region of the DNA scaffold. The second artificial protein of the linker molecule confers the ability to tightly bind a single motor protein through the heterodimeric coiled-coil association of acidic and basic leucine zippers. Leucine zippers are a pair of two peptides each 47 amino acids in length that contain four or five pairs of electrostatically attractive interhelical interactions (Moll, 2001). These zippers form strong heterodimeric complexes ($K_d \sim 10^{-15}$ M), but display much weaker homodimeric affinities ($K_d \sim 10^{-3}$-10^{-6} M). As a result, the arginine-rich basic half (Z_R) of the zipper heterodimer constitutes the final portion of the linker molecule, Z_R-$(ELS)_6$-ssDNA, while the other acidic half (Z_E) is genetically encoded onto the stalk-end terminus of an genetically engineered kinesin motor protein (K560-eGFP-Z_E-6xHis); motor proteins are expressed and purified separately as simple zipper-motor gene fusions. The leucine zipper is then the last link of the engineered two-kinesin-motor architectures, providing the technology to securely and selectively immobilize motor proteins onto the DNA scaffolds through the artificial protein DNA conjugates.

The human kinesin-1 motor construct (K560-eGFP-Z_E-His) was prepared by inserting a gene fragment encoding for the 238 amino acids of eGFP (Clonetech) and a 44 amino acid sequence of an engineered glutamic acid-rich leucine zipper (Z_E) and a

6xhistidine tag (6xHis) into the KpnI and Xho1 restriction sites of a human K560 motor construct (provided kindly by Ron Vale). Motors were purified using a standard native Ni^{2+}-NTA (nitrilotriacetic acid) purification method followed by a microtubule affinity purification procedure. Motor purity and concentrations were verified using SDS-PAGE analysis via comparison to a protein standard (BioRad), see Figure 3.2.

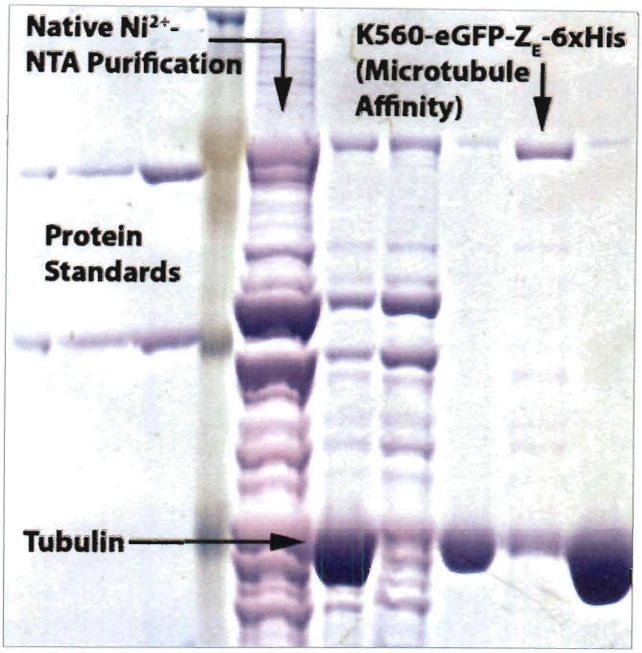

Figure 3.2: SDS-PAGE Analysis of Kinesin Motor Protein Purity and Concentration

Lanes 1-3: protein standards introduced at known ratios for use with custom image analysis software to calculate kinesin motor complex concentration, lane 4: protein ladder, lane 5: native Ni2+-NTA purification elution, lane 6-7: nickel elution bound/unbound to tubulin for affinity purification, lane8: motor bound to tubulin, lane 9: K560-eGFP-Z_E-6xHis product, lane 10: released tubulin.

The DNA-conjugated artificial proteins, Z_R-$(ELS)_6$-ssDNA, and the DNA scaffolds were synthesized as previously described (Schweller, 2008). However, the present DNA scaffolds contain a larger duplexed region and were formed from two 170 bp ssDNA. Once hybridized, the two strands form a complex consisting of a 50 nm long duplex (148 bp, 14 helical turns), flanked by single-stranded 'overhangs' that extend 22 bp from each end of the scaffold. The 'overhangs' contain complementary sequences to the oligonucleotides that were conjugated to the artificial protein linkers. Two thiamine bases were also placed between the junction of duplexed portion of the scaffold and the 'overhangs'. The thiamine bases remain unhybridized after the full assembly is formed and were introduced to provide a flexible linkage between the motor and scaffold. Two internal biotin molecules were also incorporated into the scaffold and are positioned 3 bp from the junctions between the duplexed and overhang regions of the scaffold (leaving 142 bp, 48 nm, between biotin molecules). A complete listing of the DNA strands used to construct the scaffolds is provided in (see Table 3.1, strands are listed 5' to 3'prime).

Table 3.1: DNA Oligonucleotide Sequences Used to Construct 50 nm DNA Scaffolds

DHR-2-Bio	CGTAGCAGGCACA/iBiodT/CGTTGGCTGGATAGACCGCATTCG
DHR-5-Bio	AGTCCG/iBiodT/GACTTGGCTGGATAGACCGCATTCG
DHR-1	GTCACGGACTGAGCGT
DHR- 3	CGATGTGCCT
DHR- 8	CGTATGGTAAGCGGCTCGCAATCAGCTCTGACGAGTCTGTAGGTGTCGGATGCCGAAC
DHR- 9	CTGAATAGGCGATACCGATTAGTGGACGTGGCGTGCGTAATGAGTTCACTGGCAGCAC
DHR- 10	GCTACGGTGCTGCCAGTGAACTCATTACGCACGCCACGTCCACTAATCGGTATCGCCTATTCAGGTTCGG
DHR- 11	CATCCGACACCTACAGACTCGTCAGAGCTGATTGCGAGCCGCTTACCATACGACGCTC

Optical trapping studies of this model DNA-mediated motor system are conducted through scaffold attachment to polystyrene microspheres. Therefore, microsphere surface chemistry forms the final connection in the completed model system. In these studies, polystyrene microspheres presenting surface carboxyl groups were covalently coated by NHS-ester chemistry to amine-PEG-3500 (molecular weight), BSA, and BSA-biotin molecules in defined stoichiometric ratios to produce a microsphere surface that presents biotin molecules, but primarily displays blocking agents. PEG chains do not readily exhibit specific interactions with biological chemicals and therefore act to passivate the bead surface, inhibiting aggregation of microspheres and other unwanted non-specific interactions. BSA plays a similar role as a common blocking agent used in biochemical applications. The BSA-biotin molecule introduces surface biotins to the microsphere while retaining the benefits of a blocking agent.

Incubation of the coated microspheres with streptavidin produces a surface that can be linked to the biotin sites of the molecular scaffold to complete the connection between motor and microsphere, creating the assay-ready assembly pictured in (Figure 3.3).

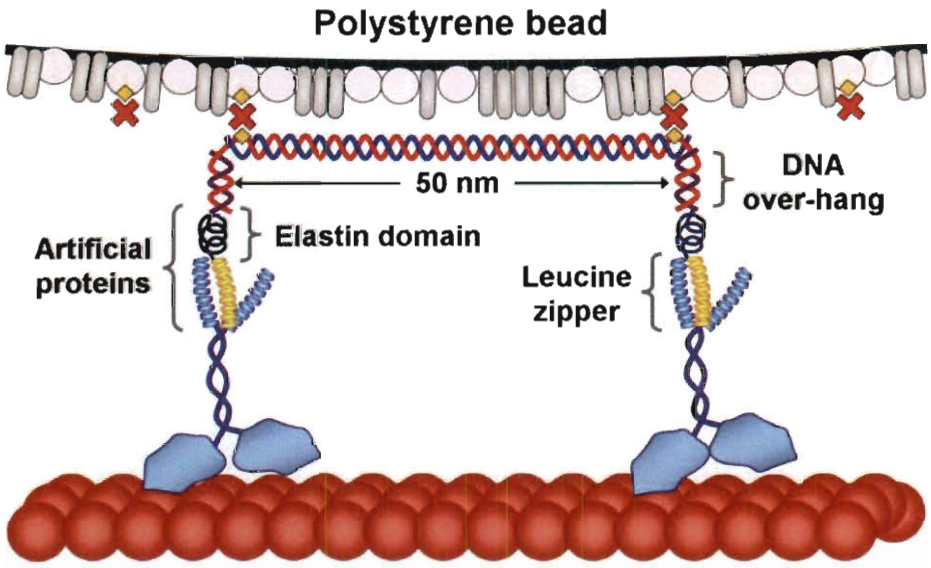

Figure 3.3: Illustration of a DNA-Templated Two-Kinesin Assembly Anchored to a Streptavidin-Coated Bead

Assembly components are drawn approximately to scale. Due to the relative scale of the polystyrene bead compared to the molecular motor assembly only a small portion of the microsphere is visible. BSA molecules are visualized as pink microsphere-bound spheres, streptavidins are represented by red crosses (with four sides corresponding to streptavidins four biotin binding sites), and biotins are pictured as orange diamonds. The motor assembly is shown bound to a small section of a microtubule (red spheres).

3.2.1. Self-Assembly of Two-Motor Complexes

Motor assemblies containing two coupled kinesin-1 motors were constructed by first preparing 'partial-assemblies' that contained the DNA scaffold hybridized to two artificial protein-based polymers. These complexes were created by annealing DNA scaffolds with the DNA-conjugated linker molecules at a 1:2 stoichiometry in Tris buffer and then incubating this mixture for 20 min. at room temperature. After confirming their quantitative formation via native PAGE gel intensity analysis, the 'partial-assemblies' were aliquoted and stored at -20° C. Complete motor assemblies were prepared immediately before each assay by combining solutions of the K560-eGFP-Z_E-6xHis motor with the 'partial-assemblies' using an eight- to ten-fold excess concentration of motor and incubating for 20 minutes at 4° C. The excess motor ensures that the vast majority of scaffold sites have a kinesin motor complex and reduces the likelihood of performing measurements on assemblies that only contain one motor. Subsequently, the entire assembly was diluted and mixed with streptavidin-functionalized beads (500 nm diameter, made from carboxylate-functionalized Bangs Beads). After incubating the motor assembles and beads together for an additional 40 min. at 4° C, the beads were further diluted approximately 50 fold into motility buffer to perform motility assays.

Single kinesins were selectively anchored to beads though a Z_R-$(ELS)_6$-ssDNA linker hybridized to a 20-bp oligonucleotide that incorporates a biotin (see Figure 3.4).

This convention mirrors the motor anchoring utilized in the two-motor assemblies. All other single-kinesin assay conditions were the same as the two-kinesin experiments.

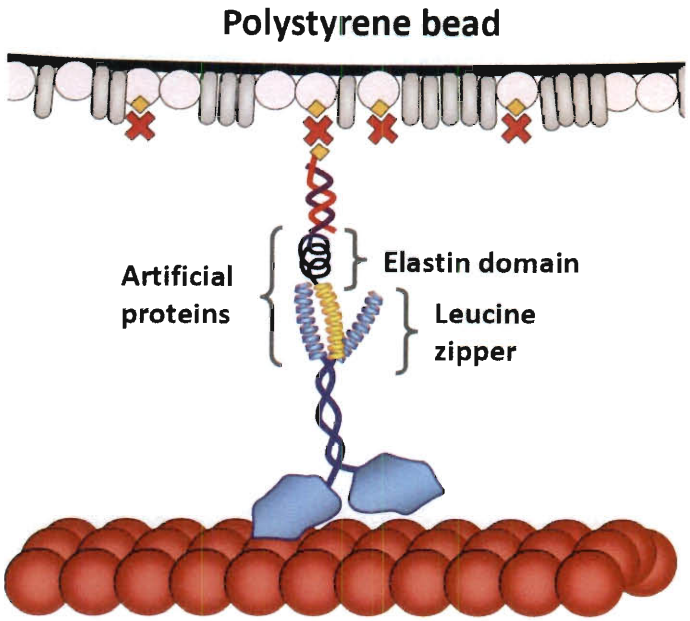

Figure 3.4: Illustration of a Single-Kinesin Assembly Anchored to a Polystyrene Bead

3.3. Optical Trapping Experimentation of Single-Kinesin and Two-Kinesin Assemblies

The aim of these optical trapping studies is to fully characterize the form-function rules that govern motility of two-kinesin systems. Multiple motor systems have the potential to exhibit enhanced motility as compared to the single motor case while providing a potential method for regulation of intracellular transport. The structure of these systems are precisely defined by the molecular architectures as described above, while motor protein activity can be characterized by force production and cargo transportation velocities, run lengths, and dwell times, etc.; quantities that describe the

ability of motor complexes to do work against applied loads and transport cargos within the cell. Highly sensitive instrumentation is necessary to probe these quantities at the single molecule level. To accomplish this task, two-kinesin systems attached to polystyrene microspheres were manipulated by a steerable optical trap operating with a back-focal-plane detection system. This type of instrument is capable of applying piconewton forces while measuring motor protein displacements at the nanoscale (Lang, 2003).

The overall goal of these experiments is to facilitate new understandings and clarify previous interpretations of multi-motor transport while testing and motivating theoretical models of critical intracellular processes. To begin, motile properties of single kinesin motors with the same leucine zipper and elastin motif attachment chemistries as the engineered two-motor system will be measured. In the single motor case, rather than connecting to the microsphere by way of a DNA scaffold, the linker molecule is conjugated to a biotinylated DNA strand providing attachment to the streptavidin-coated surface of the microsphere. Characterization of single kinesin motor transport properties when anchored by the artificial protein-ssDNA conjugate provides a structure to which direct comparisons with the two-kinesin systems can be made. In this way, enhanced motility in the two-motor case may be directly attributed to altered collective motor protein system dynamics by virtue of an increase in motor number and not to any dependence on structural or chemical attachment schemes.

Trapping experiments were performed in motility buffer (20 mM PIPES pH 6.8, 50 mM potassium acetate, 4 mM magnesium chloride, 1 mM EGTA, 2 mM DTT, 0.5 mg/mL α-casein or acetylated BSA, 2 mM ATP, and an oxygen scavenging system: 9 mg/mL glucose, 500 μg/mL glucose oxidase, 100 μg/mL catalase). When using immobilized microtubules motility buffer was supplemented with 10 μM taxol to maintain stable microtubule structures. Microtubules were either purified from bovine brain or purchased from Cytoskeleton. Alternatively, axonemes were purified from sea urchin sperm as previously described (Gibbons, 1979). Axonemes were immobilized directly on the surface coverslip slide, while microtubules were adhered to polylysine-coated coverslip surfaces. Axonemes and microtubules were visualized using bright-field and total internal reflection fluorescence modes of the trapping instrument respectively. Identical force-dependent behaviors were observed in assays employing immobilized axonemes and microtubules, and hence, "microtubule" and "axoneme" are used interchangeably in this text.

Experiments were performed on a custom-built optical trapping instrument based on previous designs. Trap stiffness was determined using the power spectrum method as described in Chapter 2.2. Bead assays were performed at room temperature ($23 \pm 1^{\circ}$ C). Data were digitized and stored at 30 kHz, after low-pass filtering at 10 kHz. All data analyses were performed using custom software written in MATLAB. Step size analysis was performed using a previously developed step-finding algorithm (Kerrsemakers, 2006). Before measurement, beads were positioned above the axis of microtubules using custom LabVIEW routines (see Chapter 2.4). Positional calibration of

the back-focal-plane detection system was carried out for each bead and measured through an AOD-controlled two-dimensional raster across the usable detection range. Due to the large displacements produced by the two-motor assemblies, once the direction of motion along a microtubule was determined, the center of the trapping beam was offset from the center of the detection beam to one end of the usable detection range in order to make full use of the calibrated detection region of the instrument. During two-kinesin assays, the beads were found to bind to microtubules in random intervals and multiple times over the time course beads were interrogated (~ 6 min). The probability of high-force detachment events (that can only be attributed to multiple kinesins from completely formed two-kinesin assemblies) was not found to depend on the time-course over which the motions of beads were examined, indicating the trapping of beads did not result in an appreciable loss of motor activity and that the assembly linkages remain intact during trapping assays.

In optical trapping assays, a two-kinesin assembly binds to a microtubule and pulls its bead in one direction against the increasing load of the trap until detachment occurs (see Figure 3.5). These two-kinesin optical trapping experiments produce traces with clear signatures of multiple motor functions (see Figure 3.6).

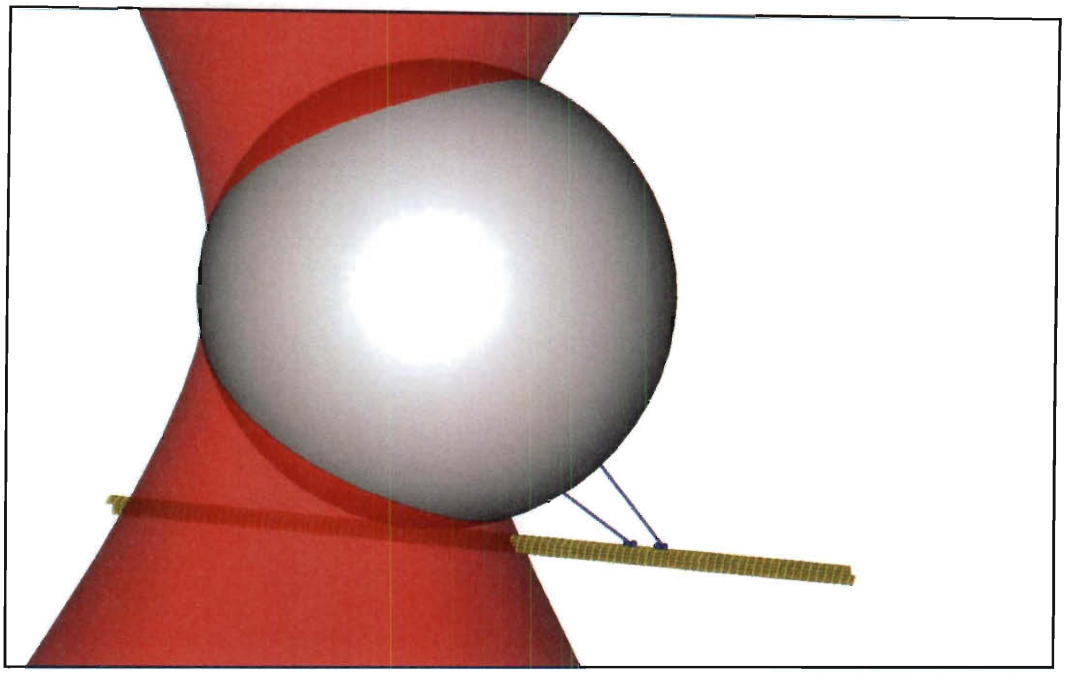

Figure 3.5: A Scaled Representation of a Two-Kinesin Assembly Pulling a Polystyrene Bead Along a Microtubule in a Static Optical Trapping Assay

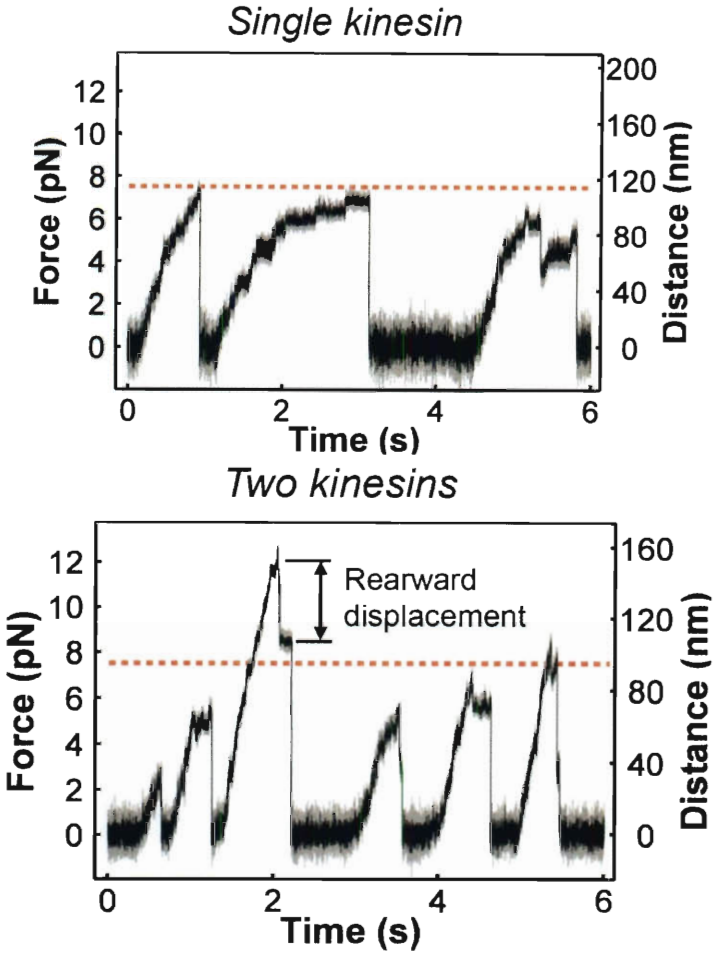

Figure 3.6: Optical Trapping Traces from Single- and Two-Kinesin Assemblies

Single kinesin motors repeatedly produce forces that approach the measured 7.6 pN stall force for a single kinesin (see Figure 3.7) as indicated by the dashed red line. Two-kinesin beads were observed to detach at forces that exceed the characteristic stalling force of a single kinesin, while also producing many events below the single kinesin stall force. A representative large rearward displacement that occurred prior to complete bead detachment is indicated in the two-kinesin data.

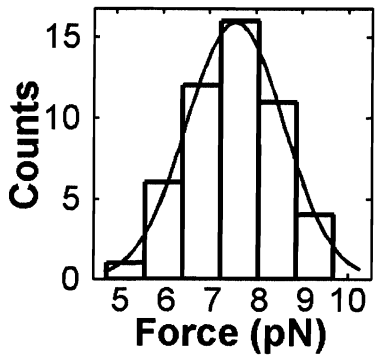

Figure 3.7: Histogram of Single-Kinesin Dwelling Events Lasting More than 150 ms

Stalling forces are a measure of the force capabilities of individual motors; they are calculated by building histograms of events where motors pause against an optical load for relatively long periods of time (in a pseudo-equilibrium state). The single-kinesin data above has been fit to a Gaussian equation centered at 7.6 ± 0.7 pN (mean ± s.d.).

In addition to producing large forces beyond the capacity of single kinesins, two-kinesin traces display features that arise from their structural architecture. More than 43% of two-kinesin trajectories contain instantaneous rearward displacements to positions other than the trap center upon microtubule detachment. Such behavior is clearly visible in individual traces (see Figure 3.8) and is indicative of a two-state unbinding process: the assembly partially detaches from the microtubule via the unbinding of only one motor before detaching completely.

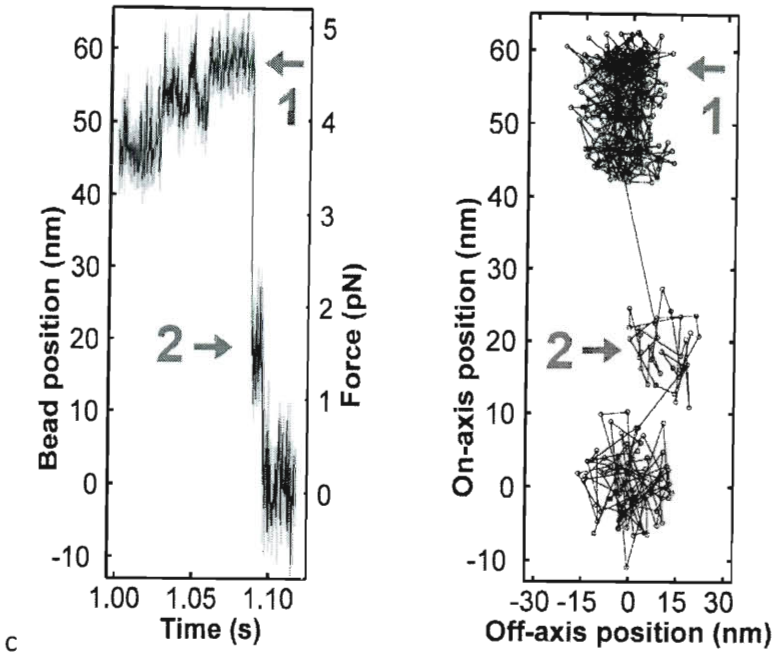

Figure 3.8: Two-State Unbinding Behavior of Two-Kinesin Assemblies

Representative position-time trace (*left panel*) and *x-y* trajectory (*right panel*) showing a large rearward displacement to a position other than the trap center upon bead detachment (several such rearward displacement events are also visible in the two-kinesin data of Figure 3.6). The positions prior to, and immediately after, the rearward displacement events are marked by the arrows and numbers in the position time and plots. In the x-y trajectory the linear structure of the microtubule filament is clearly visible along x=0. The shift in off-axis position from labeled states 1 and 2 indicate that the two-kinesins in the assembly were bound to different microtubule protofilaments.

When one motor in a two-kinesin assembly detaches from the microtubule filament, a sudden rearward displacement will occur of a magnitude related to the DNA scaffold length between the kinesins as well as their microtubule-bound states (inter-motor spacing). The rearward displacement magnitudes produced by these unbinding processes are distributed about a peak at 47 nm (Figure 3.9), indicating that the engineered DNA scaffolds have conferred distinct structural properties to the motor assemblies.

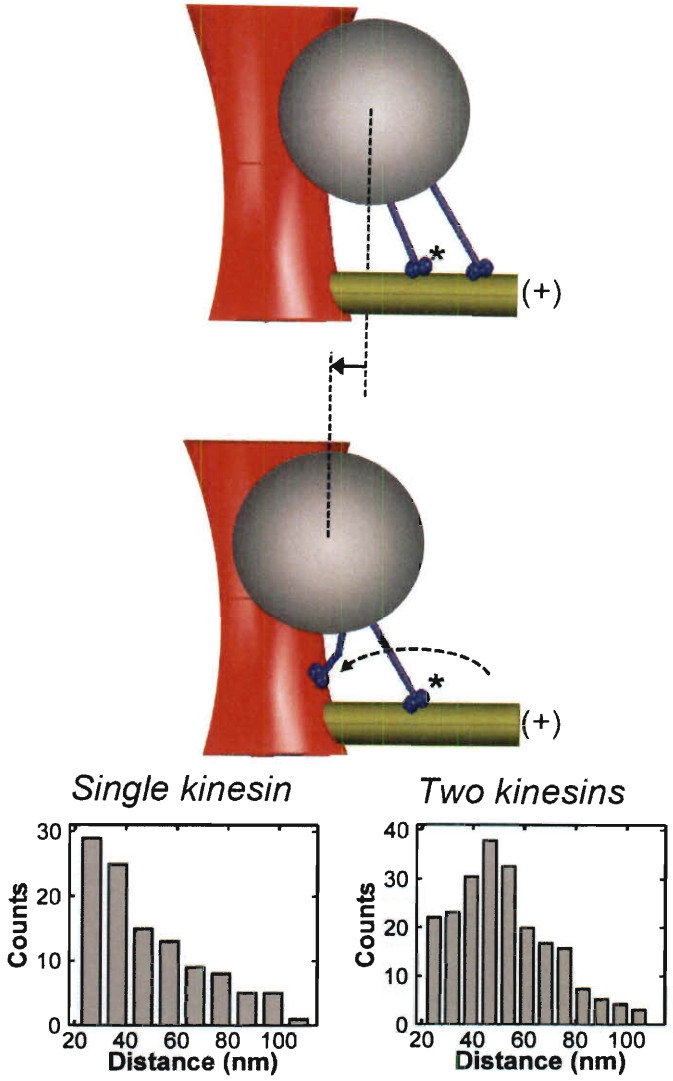

Figure 3.9: Rearward Displacement Events in Optical Trapping Traces Reveal Signatures of Engineered Motor Assemblies

An illustration of the two-state unbinding process is shown on top. Histograms of rearward displacement magnitudes that occurred during bead detachment are given for both the single-kinesin and two-kinesin cases. The two-kinesin histogram contains a peak centered at 47 nm, while the single-kinesin histogram decreases monotonically indicating only a reduced probability of observing a single motor rebinding after detachment.

3.3.1. The Statistics of Binding One Motor or One Motor Assembly to Microspheres

Before attempting motility measurements of a single kinesin or two-kinesin assembly it is important to establish that single motors or single motor assemblies are driving motion, respectively, and not collections of motors or two-motor groups. The assay conditions that support optical trapping of *individual* two-kinesin assemblies were determined by incubating beads with motor assemblies over a range of assembly/bead ratios and then measuring the fraction of beads that moved when brought into contact with microtubules (see Figure 3.10). Experimentally, the percentage of motile beads decreases with decreasing motor or motor assembly concentration in accordance with a Poisson distribution function that describes the probability that the beads are driven by one or more assemblies (Figure 3.11).

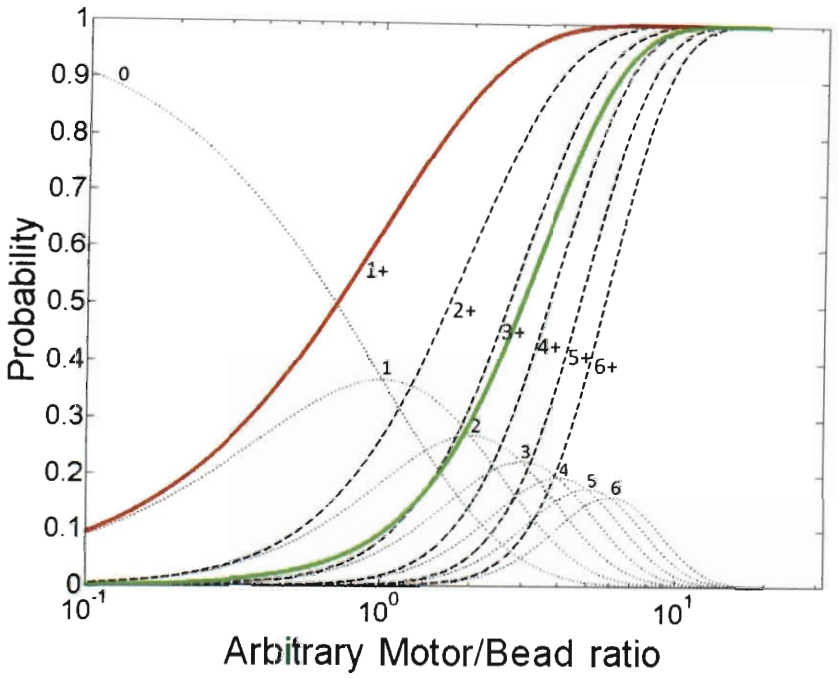

Figure 3.10: The Poisson Distribution is Used to Estimate the Number of Motors Driving Motility in Optical Trapping Assays

The Poisson distribution can be used to express the probability of having a given number of motors (or motor assemblies) bound to a polystyrene bead. The Gaussian-like nested curves are the probability mass function for the Poisson distribution given by:

$$P(C) = \frac{\lambda^C}{C!} e^{-\lambda},$$

Equation 1: Poisson Probability Mass Function

which describes the probability 'P' of having exactly 'λ' motors at a specified concentration 'C'. While the sigmoid-like curves describe the cumulative distribution function and is given by:

$$P(C) = e^{-\lambda} \sum_{n=0}^{C} \frac{\lambda^n}{n!},$$

Equation 2: Poisson Cumulative Distribution

which describes the probability of having 'λ' or more motors at a given concentration. The x-axis is in the figure can be expressed as a "Motor/Bead ratio" since this ratio is dependent on the motor concentration 'C' and bead concentration. The x-axis units are arbitrary in the sense that differing motor affinities for beads would shift these curves to higher or lower ratios. The figure may be read as follows: for example, at a motor/bead ratio of $x = 10^0=1$, Equation 1 shows there is a 37% chance of a bead having exactly 1 motor and a 20% chance of having exactly 2 motors bound to a bead. While Equation 2 shows that again at $x = 10^0=1$, there is a 64% of having 1 or more motors and a 27% chance of having 2 or more motors on a bead. For optical trapping studies, motor motility must be measured one at a time. When establishing the motor/bead ratios that are favorable for measuring one motor or one motor assembly, beads incubated with motors are brought into contact with microtubules to probe whether motility is observed or not. When motility is observed over a range of motor/bead incubation ratios this is confirmation that one or more motors is present on the bead and the data is fit to the one or more (1+) version of Equation 2 (shown in red). Optical trapping studies must always be performed under conditions where only one motor or motor assembly can interact with a microtubule at a time. This means that two motors or multiple two-kinesin assemblies can be bound to a bead as long as they are far enough apart such that they may not interact with a filament at the same time. The probability that multiple motors or multiple motor assemblies can simultaneously reach a microtubule can also be determined through a weighted sum of the Poisson cumulative distribution functions and is given by the curve in green.

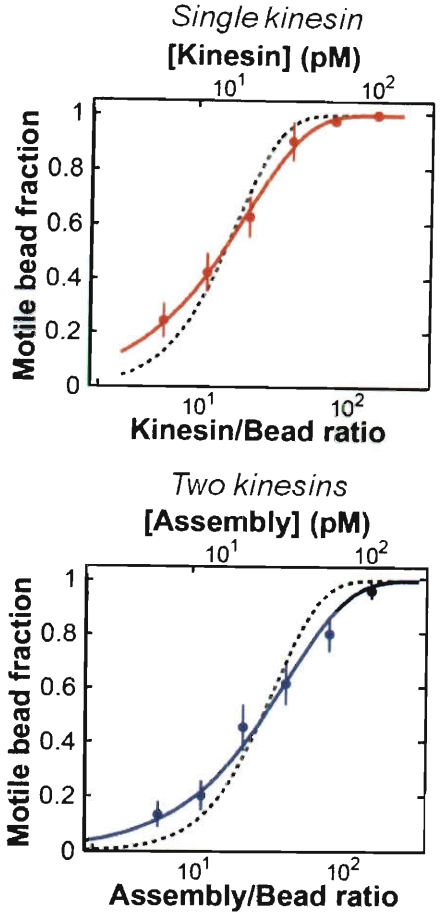

Figure 3.11: Motile Bead Fractions Obey a Poisson Cumulative Distribution Function for One or More Motor Assemblies Bound per Bead

Plots of the fraction of motile single-kinesin beads (*top panel*) and two-kinesin beads (*bottom panel*) measured at various motor/bead and assembly/bead incubation ratios (N_{beads} = 232), respectively. Data points are given as $f \pm (f(1- f)/n)^{1/2}$, where 'f' is the fraction of beads that moved along microtubules and the bead number 'n' varied between 26 – 59 from point to point. For the two-kinesin assembly case: the motile fraction data is fit to the Poisson probability that a bead is driven by one or more assemblies of kinesin motors, [$f(C) = 1 - \exp(-\lambda C)$], solid line, $\chi^2 = 0.714$, 5 degrees of freedom, P = 0.982). The dashed line indicates a fit to the probability that beads are driven by two or more assemblies: [$f(C) = 1 - \exp(-\lambda C) - \lambda C\exp(-\lambda C)$], $\chi^2 = 16.2$, 5 degrees of freedom, P = 0.006). In each case, 'C' is the assembly concentration and λ is a single fitting parameter. The solid line fit (corresponding to '1+' two-kinesin assemblies per bead) is significantly better than the dashed line fit (corresponding to '2+' two-kinesin assemblies per bead) indicating that one assembly is sufficient for bead motility.

To ensure that single-kinesin bead motion and two-kinesin bead motion were driven by only one motor or motor assembly, respectively, all assays were performed with bead-motor incubations that produced less than 35% motile fractions. Under these conditions, approximately 93% of beads should possess no more than one surface-bound kinesin or kinesin assembly, and the probability that two assemblies on a bead are positioned close enough such that both can bind a microtubule simultaneously is <2% (see Figure 3.10; Valentine, 2006). Therefore, the probability that measurements of single-kinesin motility contained two-kinesin contamination is <2% and, likewise, the chance of multiple two-kinesin assembly contamination in two-kinesin measurements is also <2%.

3.4. Detachment Force Distributions of Single Kinesin and Individual Two-Kinesin Assemblies

The ability to confidently trap individual two-kinesin assemblies allowed comparison of motor-microtubule detachment forces in single- and two-kinesin assays (Figure 3.12). For these comparisons, the distributions of the peak forces beads reached in the trap prior to detachment were evaluated regardless of dwell time; all recorded traces are included in these analyses (no data is omitted by any means of selection). Detachment forces of single kinesins are found to be asymmetrically distributed about a peak at 7.3 pN; events above 9 pN are rare. In contrast, two-kinesin bead detachments are more broadly distributed and contain events where microtubule unbinding occurred at forces up to 17 pN. Surprisingly, the histogram of two-kinesin

detachments contains a single peak at 5.6 pN (previous attempts to measure the detachment force distribution of multiple motors have reported distributions that show multiple peaks corresponding to multiples of the single motor stall force, i.e. peaks at 7 pN, 14 pN, etc.). This 5.6 pN peak persists even when two-kinesin detachment analysis is limited to trajectories that include 40-60 nm rearward displacements (Figure 3.12, inset), indicating that even the subset of events that have direct structural evidence for the engineered 50 nm DNA scaffold have a nearly identical detachment force distribution. Further, trapping data collected from each individual two-kinesin beads also reflect this detachment behavior; low-force detachments occur more often than high-force detachments (Figure 3.6). Since the assay conditions dictate that a large majority of two-kinesin beads should possess a single surface-bound assembly (Figure 3.10 and Figure 3.11), the detachment events recorded from a single bead can be reliably attributed to the same assembly. Therefore, there is great confidence that the distributions plotted in Figure 3.12 represent the detachment behavior of a two-kinesin assembly in an optical trap. Finally, it is important to note that the detachment force histograms of kinesin-driven lipid droplets have displayed a similar low-force peak detachment behavior (Sims and Xie, 2009). This finding suggests that the force distribution histograms found here for assemblies of two kinesins may indeed be representative for they way motor groups behave *in vivo*.

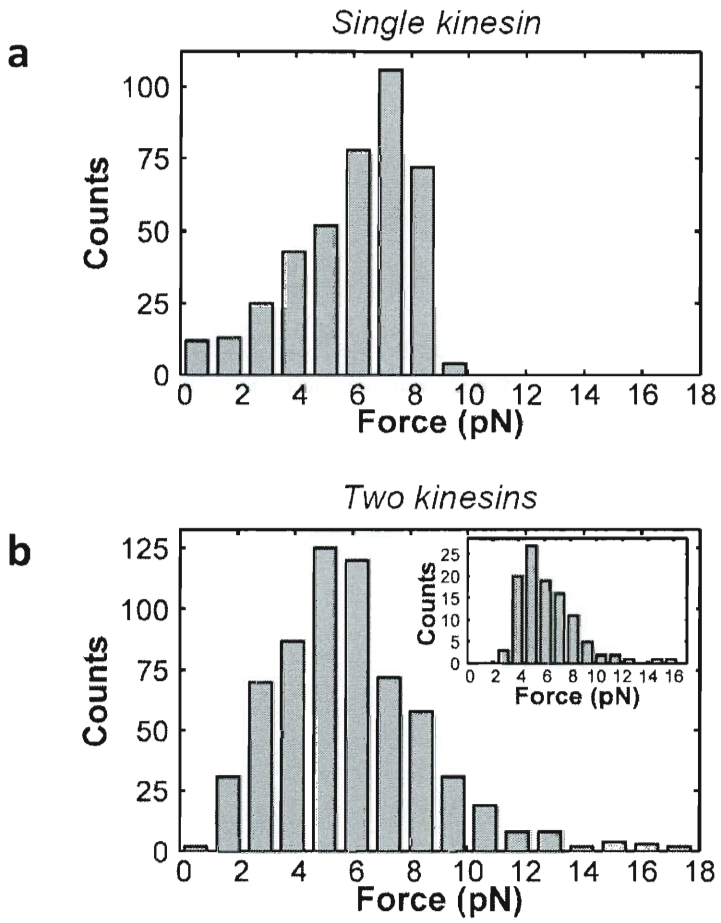

Figure 3.12: Forces Produced by Single Kinesins and Individual Two-Kinesin Assemblies

(a) Histogram of the peak forces observed prior to bead detachment in single-kinesin assays (n = 405 events). (b) Distribution of two-kinesin detachment forces (n = 640 events) observed in all traces (*main panel*) and in traces where detachment is accompanied by a rearward displacement that ranged between 40 and 60 nm in size (*inset*).

Overall, analyses of bead detachments show that two kinesins are capable of producing much higher forces than a single kinesin. However, the average detachment force measured in our single- and two-kinesin assays are surprisingly similar (6.0 ± 2.0 pN and 5.9 ± 2.6 pN respectively, mean ± s.d.). One might expect that a group of two independently functioning motors would remain associated with a microtubule for longer periods of time than a single motor and therefore detach on average at higher forces. Yet, these observations suggest that multiple kinesins do not function independently (i.e., without influencing each other's dynamics), and that such deviations from idealized collective motor behaviors can enhance the rate that a cargo will release from its microtubule track. Furthermore, the nearly identical average detachment forces observed between the two populations reveal that extreme caution should be exercised when attempting to assign experimental data to a specific motor number. Many bulk measurements of single- and multiple-kinesin dynamics should be expected to produce similar averages and behaviors when observed at a large scale. Therefore, detailed knowledge of transport behaviors at fast time scales (less than tens of milliseconds) is needed to correctly identify and attribute cargo motions to a particular motor number.

In these data sets detachment forces are reported as the peak force produced in a trace prior to detachment. The majority of two-kinesin detachment events (> 75%) were preceded by only a short (<<200 ms) dwell, generating 'sharp' peaks such as those displayed in Figure 3.6. Thus, all detachment events were recorded so that the full distribution of peak forces produced by the two-motor assemblies could be compared

more easily to single-kinesin data (i.e. the lifetimes of single-kinesin and two-kinesin motility events are inherently different, therefore all detachment events must be recorded and analyzed, not just events that dwelled beyond a specific threshold dwell time as is common in many motor stall analyses, see Figure 3.7). Rare events, (e.g., the left side of Figure 3.14) possess longer two-kinesin dwells coupled with backward motions that can be attributed to super-stall behavior of one kinesin within a two-kinesin assembly (i.e. two kinesins work together to generate a force larger than a single kinesin can produce, then when one motor detaches the remaining motor is faced with a "super-stall" force which it cannot overcome and so it is pulled backward towards the trap).

3.4.1. Stall Force Analyses of Single and Coupled Kinesins

The so-called "stall force" is a commonly measured and often quoted parameter in single motor protein biophysical studies that aims to describe the force-production capabilities of an individual molecular motor with a single force value. The stall force of a single kinesin is often determined by constructing histograms of motor dwelling events (times where a motor pauses its forward motion for a relatively long period of time) surpassing a time threshold prior to microtubule detachment. These histograms produce Gaussian-like distributions of events that estimate the stall force of single motors. The stall force for a single kinesin was determined by evaluating detachment events where beads dwelled for more than 150 ms immediately prior to detachment. Consistent with previous work (Kojima, 1997; Carter, 2005; Visscher, 1999; Nishiyama,

2002), this analysis produced a Gaussian distribution of detachment events peaked at 7.6 pN (see Figure 3.7). As with other kinesin motors, the behavior of single human kinesin constructs against forces is characterized by relatively short dwell times prior to detachment (88 % are shorter than 150 ms). In two-kinesin assays, dwells of this length of time prior to detachment were not observed in any of the two-kinesin assays at high forces (>10 pN), where two-kinesin stalling behavior might be expected. This result indicates that two-motor states are relatively short lived under high-force conditions and that dwell time analysis of this type is not well-suited for determination of a two-kinesin stall force. One would expect this short dwell time behavior for multiple motor assemblies whether the motors function non-cooperatively or exhibit negative cooperativity as in the present assays. Even for non-cooperating motors, the force-dependent (F) detachment rate (k_{off}) of motors in an assembly should increase with motor number (n) according to $k_{off}(F,n) = n_{bound} \times k_{off}(F,n=1)$. Consequently, dwell times prior to detachment should then become increasingly short as motor number increases, making dwell time analysis of multiple-motors an inadequate measure of multiple-motor stall force.

However, an alternative definition of stall force is better suited to multiple motor cases. When stall force is defined as the force at which forward and backward stepping rates are equal (and hence motor assemblies net zero forward motion), then the stall force is decoupled from a dwell time dependence and an estimate can be made (see Figure 3.13). In this figure the forward/backward stepping ratios for two-kinesin assemblies are calculated for forces greater than 8 pN. As we will see in later sections,

states where both motors in a two-kinesin assembly are bound to the microtubule are only dominant at forces above the single kinesin stall force (7.6 pN); consequently this kind of stepping ratio analysis is only appropriate at such super-stall forces. The data shows that up to forces of 16 pN the forward/backward stepping ratio does not approach unity to meet the criteria of the stall force definition, however, the data does follow a linear trend on a semi-log plot along the y-axis which can be extrapolated to estimate a stall force of approximately 22 pN for the two-kinesin assembly.

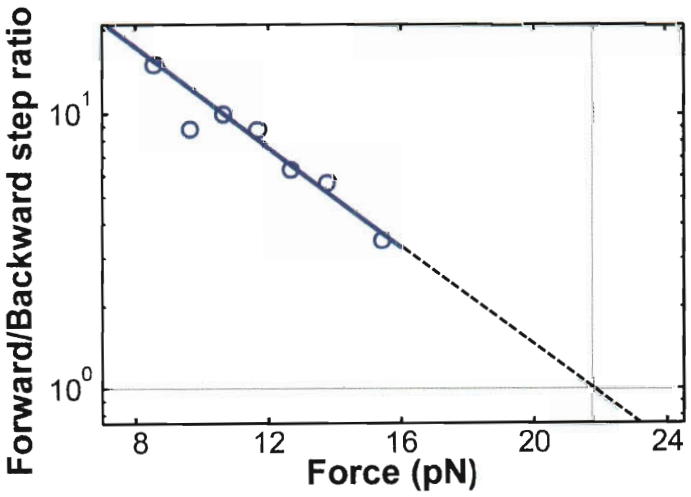

Figure 3.13: Characterizing a Two-Kinesin Assembly Stall Force

The significance of a multiple motor stall force is unclear. While the estimated 22 pN stall force may be representative of the force that two kinesins are capable of producing in theory, no experimental two-kinesin data was observed above 18 pN; this could be the result of the inherent difficulty two-kinesins have in simultaneously sharing load and not because two-kinesins are incapable of producing forces of this magnitude. Still, it is interesting to note that earlier studies (Schnitzer, 2000) have predicted that

single kinesins would be able to produce 11 pN alone were it not for a loss in mechanochemical efficiency (see Section3.6). It is possible that by coupling two kinesins together their mechanochemical coupling of ATP hydrolysis into productive forward motion may be increased such that higher force production is possible. In any case it is clear that by this definition the two-kinesin stall force must be >16 pN, which is still larger than what is expected from twice the single kinesin stall force. However, caution should be exercised in attributing meaning to (or making estimates of) a multi-motor stall force given that motor systems can adopt a large number of microtubule-bound configurations that affect their activity under imposed loads.

3.4.2. Estimating Single-Motor Contamination in Two-Kinesin Assays

The frequency of stalling events in single- and two-kinesin assays provides a simple means of estimating an upper bound for the contamination of single kinesin measurements in two-kinesin assays. In single-kinesin assays <12% of all microtubule detachments include a 'long-dwell' (>150 ms) centered at the stall force of a single kinesin prior to detachment (see Figure 3.7). Dwells of this relatively extended period of time constitute only 2% of detachments in two-kinesin assays. Given that: (1) these long-dwell time events occur interspersed between high velocity and force events that could not be supported by a single kinesin and (2) more than 93% of beads measured have no more than one surface-bound assembly (see Figure 3.11), the vast majority of these detachment events likely correspond to a single kinesin within a two-kinesin assembly undergoing stalling behavior. However, if the possibility that single-motor

contamination in two-motor assays produced the 2% of long-dwelling events observed in two-kinesin assays is considered it is still expected by a simple ratiometric estimate that at least 83% of measured two-kinesin detachments come from complete assemblies (~12% of single kinesin events can be expected to stall, therefore 88% do not stall, the 2% of long-dwells in two-kinesin assays would then mean that up to 17% of two-kinesin events were generated by only one kinesin). This level of single-motor contamination would not influence the measured detachment force distribution for two-kinesins very significantly, and again, this calculation completely disregards the possibility of one motor within a two-motor assembly displaying stalling behavior. As is described in a later section, the motor-microtubule detachment rates for the two-kinesin assembly are much higher than the binding rates of individual kinesins within the assembly (see Figure 3.36). Therefore, motor assemblies are expected to spend the majority of their time with a single kinesin bound, and so this level of long-dwelling events at the stall force of a single kinesin are expected.

3.5. Two-Kinesin Assemblies Transition between Microstates with Different Numbers of Load-Bearing Motors

The force-velocity (*F-V*) relationships for single-kinesin and two-kinesin assemblies describe their ability to transport cargos against an external load. Importantly, a two-kinesin assembly can adopt different microtubule-bound configurations (*microstates*) that are primarily distinguished by the number of microtubule-bound motors, and when both motors are bound, by the spacing between

their microtubule-binding sites. When a two-kinesin assembly assumes a configuration where both kinesins bear a significant portion of the applied load, beads should move faster than when only one assembly motor drives transport. This behavior was examined by calculating instantaneous bead velocities using a procedure that applies a 200 ms sliding linear regression window to position vs. time traces from static optical trapping data(Coppin, 1997). This data was then used to construct load-dependent velocity distribution histograms for the two-kinesin assemblies (Figure 3.15).

While calculating two-kinesin *F-V* relationships, clear transitions were observed within most trajectories where beads either accelerated or decelerated between distinct non-zero bead velocities (Figure 3.14). These transitions can be used to identify portions of trajectories where bead motion is driven by one or two motor molecules. To do so, a threshold acceleration rate ($\left| dV/dF \right| > 125$ nm·s^{-1}·pN^{-1}) was used to determine the forces at which velocity transitions occurred, and then separate traces into 'low' and 'high' velocity segments depending on whether beads decelerated or accelerated into a segment, respectively. The resulting trace components were then pooled into 'low' or 'high' velocity sub-populations and plotted on top of the raw velocity distribution data (Figure 3.15).

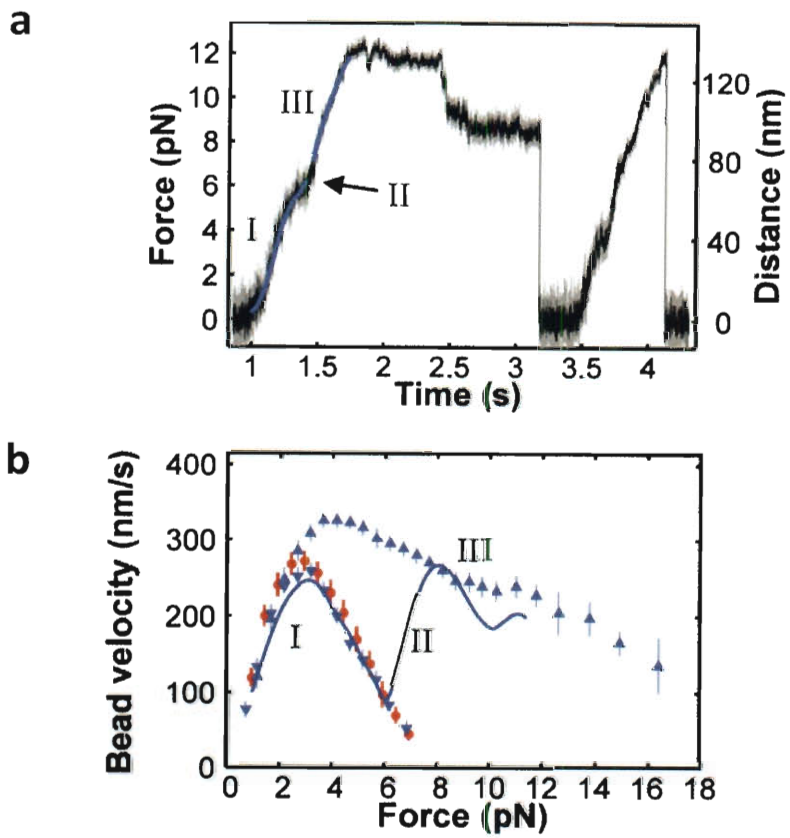

Figure 3.14: Detection of Transitions Between Distinct Two-Kinesin Assembly Microstates

(a) A two-kinesin bead trajectory showing a transition (II) between assembly microstates with 'low' (single load-bearing motor, I) and 'high' (two load-bearing motors, III) velocities. The corresponding trajectory components are indicated by roman numerals in the position-time and force-velocity plots. (b) The lower *F-V* plot displays the average velocities measured from trajectories where bead detachment occurred at an applied trapping load greater than 10 pN (*blue triangles*). Throughout this document force production greater than 10 pN is considered a signature of multiple-kinesin motility, single kinesin events of this magnitude have not been observed in the literature. The upward-pointing triangles indicate the average segment velocities for the 'high' velocity (two load-bearing kinesin) configurations of the assembly. The downward-pointing triangles correspond to 'low' velocity components (one load-bearing kinesin). The red circles denote the measured *F-V* relationship for a single kinesin. Velocities are displayed as mean ± s.e.m.

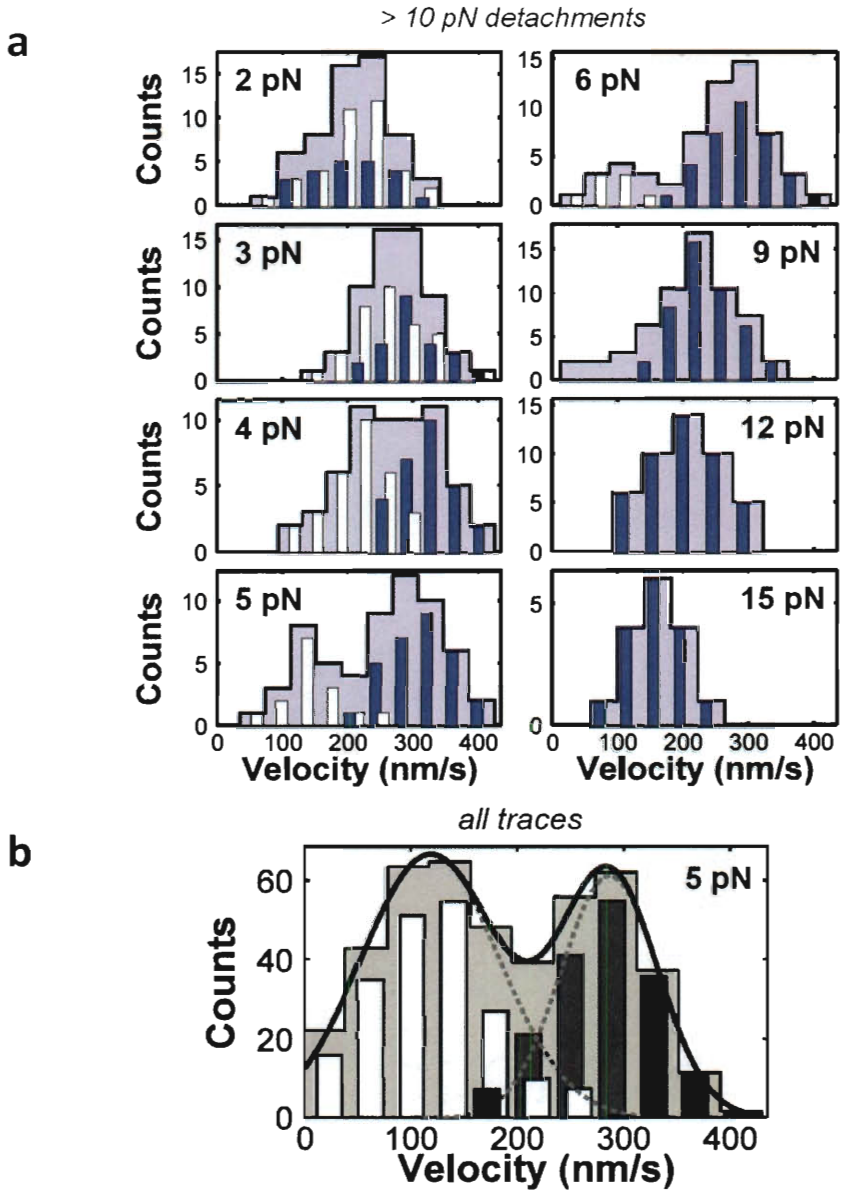

Figure 3.15: Load-Dependent Velocity Distributions for Two-Kinesin Assemblies

(a) Histograms of two-kinesin bead velocities analyzed in traces where bead detachment occurred at high forces (>10 pN). The white and blue bars indicate the velocities of the two-kinesin beads when their trajectory components were assigned to either single load-bearing or two load-bearing kinesin sub-populations respectively. The light blue background indicates the velocity distributions for all measured events before microstate identification. (b) Velocity distributions of two-kinesin beads at 5 pN using all measured two-kinesin trajectories (i.e. two-kinesin bead trajectories that detached from the microtubule at any force greater than 5 pN).

Between loads of 4-8 pN, two-kinesin velocity histograms contain two distinct peaks, regardless of whether they are constructed using trajectories where bead detachment occurred above 10 pN (under loads that require two kinesins, Figure 3.15a), at lower forces (4.5-6.5 pN, corresponding to the peak two-kinesin detachment forces found in Figure 3.12), or using all recorded traces (Figure 3.15b). The Gaussian-like shape and overlap of each distribution with the peaks found in the raw (untouched) velocity histograms demonstrates that this method correctly assigns bead trajectory components to their appropriate microstates (one load-bearing or two load-bearing kinesins). Yet, this method does not distinguish between microstate configurations that yield similar velocities (i.e., beads should move with similar, 'single-kinesin', velocities when only one of the assembly's kinesins is bound to the microtubule and when both assembly kinesins are bound but only one motor assumes the applied load of the trap). Therefore, the velocity histograms in Figure 3.15 are best described as a distribution of two classes of two-kinesin assembly microstates where either one or both assembly kinesins bear the applied load of the trap.

To further examine how two kinesins transport beads when they adopt specific microtubule-bound configurations, the velocities of each microstate sub-population were averaged and two distinct curves describing the *F-V* dependence for each detected assembly microstate were generated (Figure 3.14b). One curve follows the *F-V* relationship measured for a single kinesin (red data), while the second curve extends to greater forces and displays higher velocities. In this plot, bead velocities are attenuated by the stretching of microtubule-bead linkages as they move against the increasing load

of the trap (this effect is most significant at low forces, < 3 pN, and gives rise to the concave-downward curvature of each plot). Indeed, the close agreement of the 'low-velocity' curve with the single-kinesin *F-V* data indicates that the two-kinesin trace segments assigned to the 'low-velocity' population can be reliably attributed to events where only one assembly motor drives bead motion. The second, 'high-velocity' curve therefore stems from microstates where both assembly motors worked together as a team.

3.6. Two-Kinesin Force-Velocity Relationships Deviate from Non-Cooperative Motor Models

Measurements of single- and two-kinesin elasticities were next used to construct *F-V* plots that account for the stretching of microtubule-bead linkages (see Figure 3.16 and Figure 3.17). The resultant curve for single kinesins (*red circles*) was then fit to a previously reported *F-V* relationship for single kinesin motors (Schnitzer et al., 2000), which allowed a theoretical two-kinesin curve to be generated assuming that each motor simply experiences half of the applied load on the bead and that the motors do not interact. At low loads, two-kinesin microstate *F-V* relationships generally follow their respective theoretical curves. However, when two-kinesin beads moved with single-load-bearing motor velocities, their average velocity tended to be lower than their corresponding single-kinesin values; a Welch's t-test shows there is a significant velocity difference ($p < 0.001$ between the two data sets from 2-5 pN). Given these deviations, our results further indicate that motors within the two-kinesin assembly

have the potential to interact and that these interactions lower the average velocities of beads and the forces at which they detach.

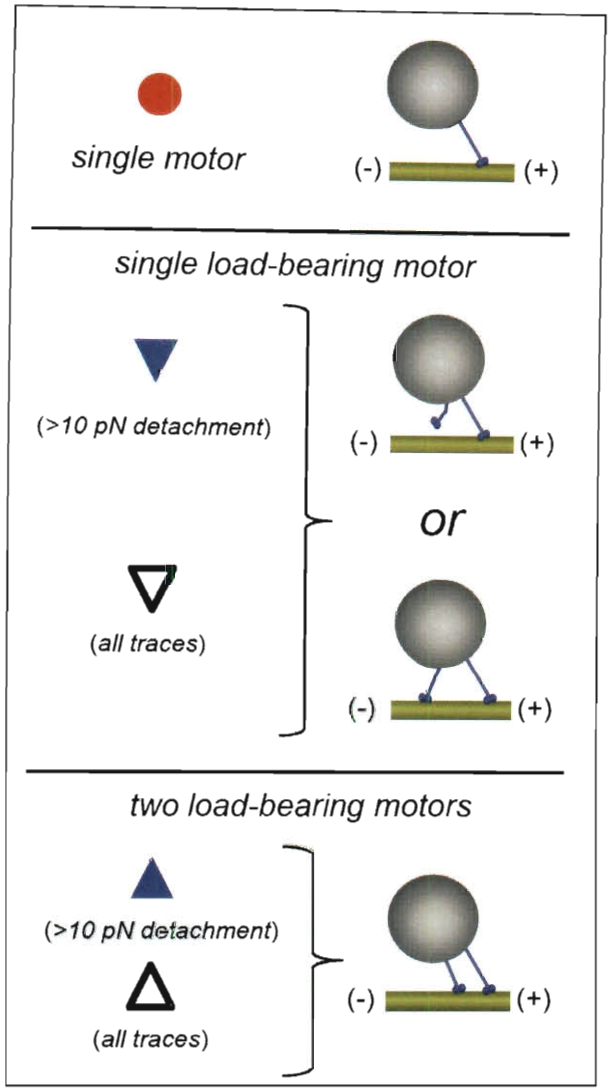

Figure 3.16: Legend Describing Two-Kinesin Microtubule-Bound and Load-Bearing States

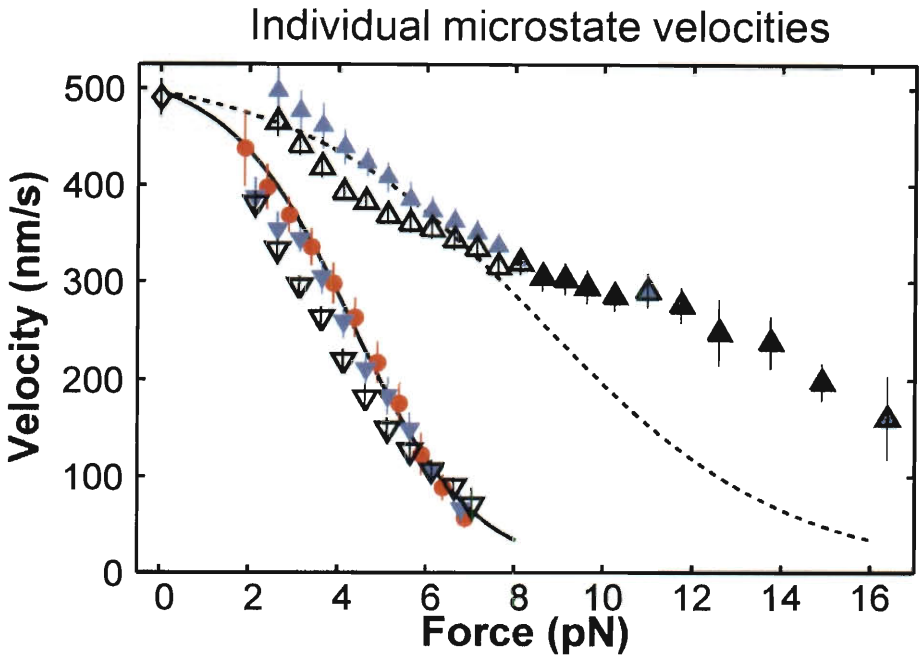

Figure 3.17: Force-Velocity Relationships for Single- and Two-Kinesin Assemblies

Force-dependent velocities of two-kinesin beads that account for motor construct stretching during bead advancement. The solid and dashed lines denote a fit to single-kinesin *F-V* data and predicted two-motor velocities assuming assembly motors share the applied load of the trap equally, respectively. The red circles denote single kinesin *F-V* data. Triangles represent the average velocities of traces segments that were assigned to different microstate configurations as indicated by the legend in Figure 3.16. Error bars are given as the s.e.m.

The overall lower velocities of two-kinesin assemblies in single load-bearing motor states as compared to single kinesin velocities may be indicative of non-productive force interactions between the two motors in an assembly (this possibility will be investigated in more detail in 3.8). Nevertheless, the velocity difference between these two cases is approximately 50 nm/s; given the slope of the single kinesin F-V data, this kind of velocity depression can arise from just an additional 1 pN of rearward force, perhaps caused by a trailing motor in a two-kinesin assembly. Alternatively, the observed drop in velocity might be the result of an increased detachment rate of the load-bearing motor as a result of greater upward load perpendicular to the microtubule axis or other loading conditions known to augment kinesin's detachment force properties.

Deviations from predicted *F-V* behaviors were also observed at high applied loads (above the stall force of a single kinesin). Surprisingly, two-kinesin beads moved with appreciably higher velocities than those in the theoretical curve (where motors are assumed to share applied load equally). The enhancement of bead velocities observed at high forces may be indicative of a synergistic collective effect, where coupling motors together results in a load carrying capacity that is more than additive. Although this extra gain in motor activity could stem from several sources, a cooperative mechanism where nearby motors in an assembly assist each other in force production by maintaining kinesin's intrinsic tight-coupling between ATP hydrolysis and motion seems most promising. Previous measurements of a single kinesin's mechanics have shown that load lowers the molecular motor turnover rate while also reducing the rate at

which ATP binds and commits to a productive kinesin step in the reaction pathway. The mechanochemical coupling ratio, defined as the number of ATPs hydrolyzed per kinesin step, has been measured as 1:1 from zero load to approximately 5.5 pN (Schnitzer, 2000). Above a rearward force of 5.5 pN tight mechanochemical coupling is lost, meaning non-productive ATP hydrolysis becomes much more prevalent. This loss of coupling means that a single kinesin exhibits a "stall force" of 5.5-7.5 pN (depending on ATP concentration), whereas without this effect a single kinesin should be capable of producing forces as large as 11 pN. It is also interesting to note that, perhaps not coincidentally, the average opening force of the neck coiled coil of kinesin-1 has been measured as 11 pN (Bornschlogl, 2008). The enhanced two-kinesin velocities at high loads suggests that the communication of forces or ability to share loads between multiple motors in an assembly allows kinesin to maintain its tight coupling over a larger range of applied loads, and hence permits multiple motors to better tap their potential for force production. In any case, the fact that these transport events occur relatively infrequently, as indicated by Figure 3.12, suggests that specific conditions (e.g., motor assembly orientations and/or motor-microtubule binding configurations) are required for a two-kinesin assembly to produce large forces.

3.7. Two Kinesin Assemblies Tend to Transport Cargos via a Single Load-Bearing Motor

Two-kinesin assemblies were evaluated to determine whether they tend to adopt particular microstate configurations during cargo transport by examining the time that beads spent moving with either 'low' (single load-bearing motor) or 'high' (two-load-bearing motor) velocities as a function of the optical trap's applied load (Figure 3.18). In general, single load-bearing motor microstates are much more prevalent at low applied loads; below the single-kinesin stall force motor assemblies spend >76% of their time moving with single-kinesin velocities. Yet, above kinesin's stall force, one-load-bearing motor microstates become extremely rare since a single kinesin cannot easily transport beads against such loads without the assistance of a partner.

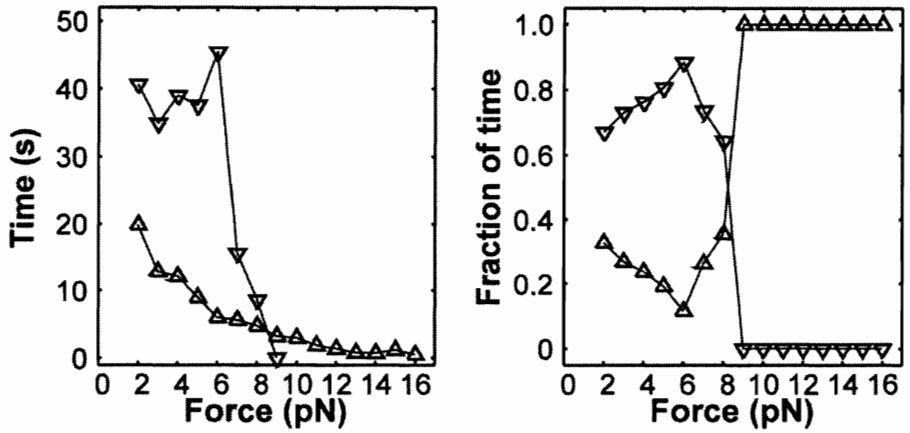

Figure 3.18: Bead Transport is Most Commonly Driven by a Single Motor in a Two-Kinesin Assembly

Total experimental time (*left*) and proportion of time (*right*) two-kinesin beads spend moving with single motor velocities (downward pointing triangles) or two load-bearing motor velocities (upward pointing triangles).

The prevalence of 'low-velocity' microstates seen in Figure 3.18 also influences the ensemble- and time-average velocities of the two-kinesin beads (Figure 3.19). At low applied loads, ensemble-average velocities largely follow the measured single-kinesin force-velocity curve: this concordance is even stronger when the average microstate velocities are weighted by the time they are found to occupy each velocity sub-population. As a result, microstates possessing two load-bearing kinesins appear to be relatively rare and short lived, and hence, make minor contributions to the overall cargo velocity at low applied loads.

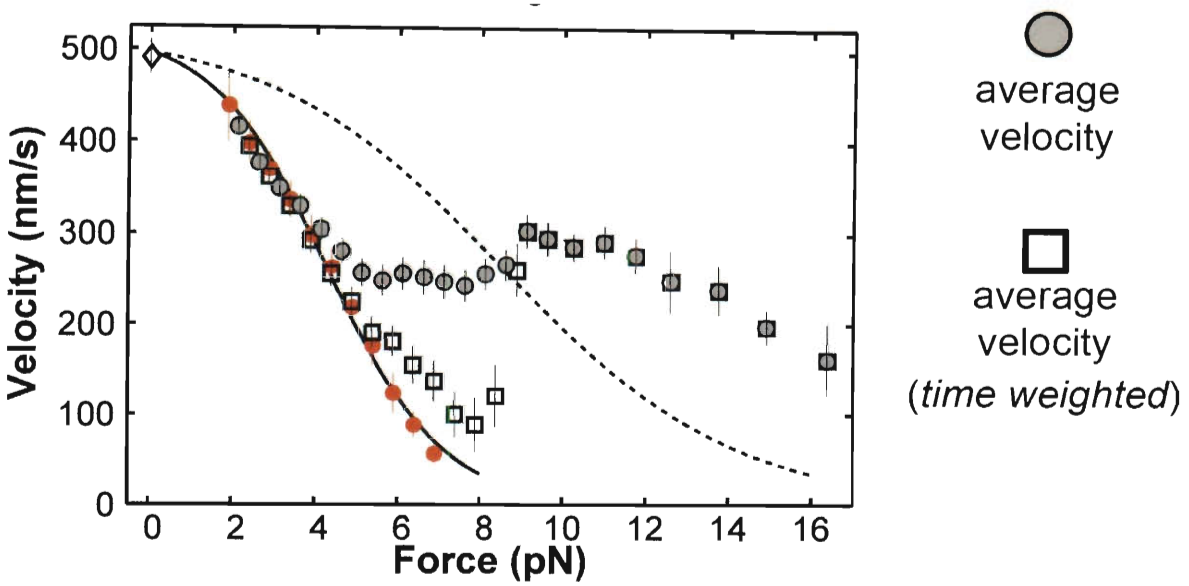

Figure 3.19: Time-Averaged Two-kinesin Force-Velocity Curves Demonstrate the Dominance of Single-kinesin States in Mulit-Motor Motility

The average velocity (*grey circles*) and the time-weighted average velocity (*squares*) of two-kinesin beads plotted as a function of the applied load. The zero-load velocities (*diamond*) of single kinesins and two-kinesin assemblies were found to be nearly identical, as previously determined (Rogers et al., 2009). Error bars are given as the s.e.m.

3.8. Composite Elastic Properties of Two-Kinesin Assemblies Suggest Non-Equal Load Sharing Among Constituent Motors

To gain mechanistic insight into how an assembly's microtubule-bound configuration influences two-kinesin force production and velocity, the elastic properties of two-kinesin assemblies were characterized when both motors were microtubule-bound and engaged in transport by analyzing positional fluctuations of beads over a range of applied optical loads (see Section 3.8.1). In order to facilitate comparison of single-kinesin and assembly elasticities both data sets were calculated using identical methods except that assembly stiffness were measured exclusively from trace components where both motors were responsible for bead motion (i.e., two load-bearing motor states as identified by the transition analysis described in Section 3.7). The results from these analyses are displayed in Figure 3.20.

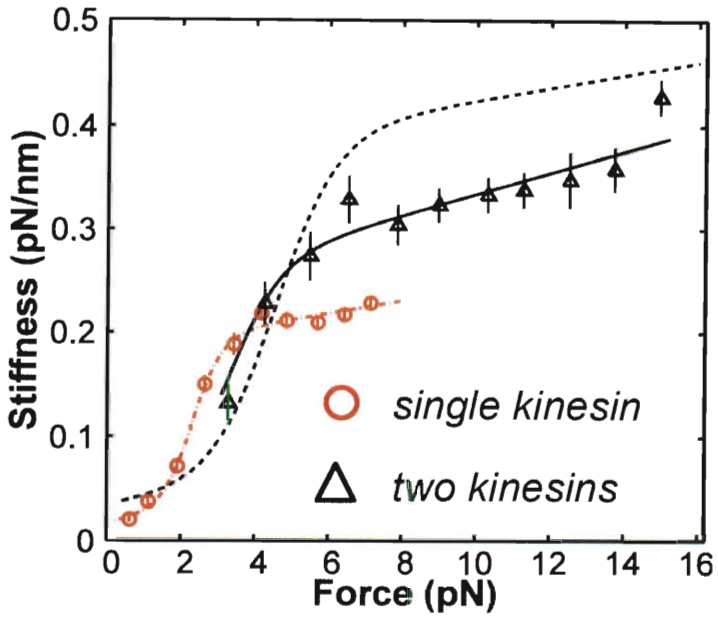

Figure 3.20: Analyses of Single-Kinesin and Two-Kinesin Assembly Elasticities

Measured elasticities (stiffnesses) of single kinesins (κ_{mot}, red circles, dash-dot line) and two-kinesin assemblies ($\kappa_{assembly}$, black triangles, solid line). The dashed black line is the expected two-kinesin stiffnesses when both motors in a two-kinesin assembly share the load of the optical trap equally as calculated from a parallel-springs analysis of the single kinesin stiffness data (see Equation 3). All data is given as mean ± s.e.m.

As with previous studies, single motor stiffness (κ_{mot}) is found to increase non-linearly with increasing force (Kojima et al., 1997). However, the net elasticity of the K560-eGFP-Z_E-6xHis construct is smaller than that of wild-type kinesin motors since the artificial protein linkers employed here include a compliant poly(VPGVG) domain (Diehl et al., 2006). Nevertheless, the dependence of κ_{mot} on the applied load could be fit by a sigmoid function (see Section 3.8.1), and this function can be used to approximate the composite stiffness of a two-kinesin assembly ($\kappa_{assembly}$), assuming the two motors behave as parallel springs that share the applied load of the trap equally:

$$\kappa_{assembly}(F_{trap}) = 2\kappa_{motor}(F_{trap}/2),$$

Equation 3: Parallel Springs Analysis of Motor Stiffness

where κ denotes stiffness. Overall, significant deviations were observed from a parallel-springs behavior. There is a general shift of the assembly stiffnesses from the predicted curve towards the trend measured for a single-kinesin; the values lie in between the predicted two-kinesin and single-kinesin curves. This result indicates that motors in a two-kinesin assembly will be stretched to different extents when both motors are filament-bound and will not be able to share the applied load of the trap equally (see Section 3.8.2).

3.8.1. Fits to Single- and Two-Kinesin Assembly Stiffness Data

The stiffnesses of single kinesins and two-kinesin assemblies were determined by analyzing positional fluctuations in traces at a fixed bead position between motor

stepping events. This analysis is similar to previously reported methods (Coppin, 1997) and yields the composite stiffness for the motor-bead system in the optical trap (κ_{tot}) as a function of the applied load. When analyzing single-kinesin data, κ_{tot} is the sum of the motor elasticity and the optical trap's spring constant:

$$\kappa_{tot}(F_{trap}) = \kappa_{mot}(F_{trap}) + \kappa_{trap},$$

Equation 4: Total Stiffness Equation for Static Optical Trapping Assays

In two-kinesin assays, κ_{tot} is sum of the composite, or effective, stiffness of the entire two-motor assembly and that of the optical trap $\kappa_{tot}(F_{trap}) = \kappa_{assembly}(F_{trap}) + \kappa_{trap}$. Measured values for κ_{trap} were determined for each bead via power spectrum analyses. The data in Figure 3.20 represents the average stiffness for single-kinesins and two-kinesin assemblies calculated using the equations described above. As presented in Figure 3.20, $\kappa_{mot/assembly}$ is the effective motor/assembly stiffness as measured along the microtubule axis rather than along axis of the kinesin molecule(s) (i.e., positional fluctuations are measured along the microtubule axis whereas the kinesin molecule's stalk axis is constantly changing direction depending on the loading and geometry being experienced by a motor).

Fits to single-kinesin stiffness data in Figure 3.20 were determined using a mechanical modeling / non-linear regression routine programmed in MATLAB. In this routine, the axial (along the motor-axis) force-extension properties of the kinesin-1 / polymer construct were approximated empirically using a sigmoid function. The unstretched length of the motor is assumed to be ~52 nm (accounting for the motor,

the GFP, the artificial protein, and the DNA overhang of the scaffold). With these parameters, the routine models the mechanical state of a trapped bead that is bound to the microtubule via a single kinesin molecule. The equilibrium center position of the bead, the stretched length of the motor, and the angle the motor projects from the microtubule are all determined via a force-balance and/or energy minimization procedure. The component of the single-motor stiffness projected along the microtubule axis (κ_{mot}), which corresponds to the data presented in Figure 3.20 can then be calculated directly from the modeled mechanical equilibrium state of the motor by evaluating the change in the force imposed on the bead by the motor when the bead position is modulated. To fit the single-kinesin stiffness data, a regression algorithm was employed that reiteratively modifies the initial sigmoid function, and repeats the mechanical modeling routine until a function describing the force-dependent single-kinesin stiffness is found. With the fitted single-kinesin force-extension behavior (see Figure 3.21) that results from this procedure load distributions within all possible two-kinesin assembly microtubule-bound states can also be calculated (Section 3.8.2).

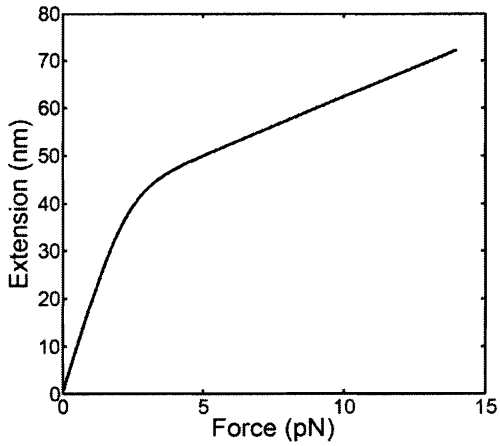

Figure 3.21: Fitted Force-Extension Relationship of a Single K560-eGFP-Z_E Construct

Calculated single-kinesin stiffness values were also used to make a theoretical prediction of the stiffness that an idealized two-kinesin assembly would exhibit if both assembly motors shared their applied load equally, as described above. However, the true composite stiffness of a two-kinesin assembly is dependent on its microtubule-bound configuration, and hence, the experimental two-kinesin stiffness data plotted in Figure 3.20 represents an average of assembly stiffnesses across a range of assembly configurations. As shown in Figure 3.22, fitting this elasticity data requires explicit knowledge of the relative probabilities of specific assembly configurations. Thus, a trend-line that approximates the average two-kinesin assembly stiffness by fitting the data to the sum of a sigmoid and a line was generated for continuity and also to create correction factors described later in Section 3.9.4.

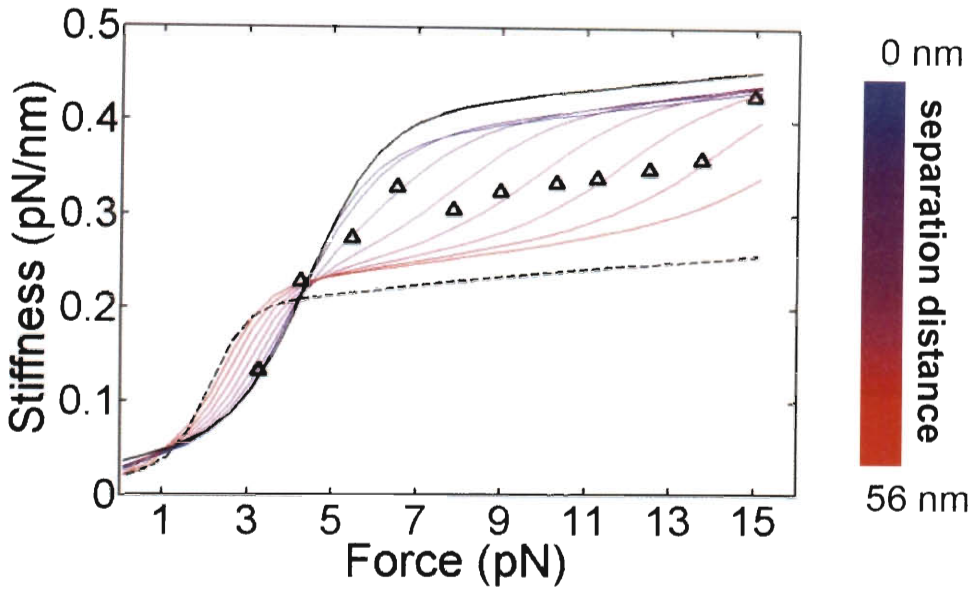

Figure 3.22: Configuration-Dependent Two-Kinesin Assembly Stiffnesses

The composite two-kinesin assembly stiffness ($\kappa_{asssembly}$) is plotted as a function of the applied trapping load. Measured two-kinesin stiffnesses are denoted by the triangles. The dashed and solid lines represent the fits to the single kinesin data and the predicted curve that assumes equal load sharing by the both motors in a two-kinesin assembly, respectively. The colored lines indicate the stiffness calculated by mechanical modeling of assemblies over the range of separation distances indicated in the legend (separation distances are increased in 8 nm increments, corresponding to each motor protein binding position on a microtubule filament).

3.8.2. Modeling Load Distributions within Two-Kinesin Assemblies and Two-Kinesin Bead Displacement Magnitudes

To evaluate the influence of two-kinesin assembly-microtubule binding geometry on the distribution of forces within motor assemblies, the force-balance / energy minimization procedure (see Section 3.8.1) was used to determine the mechanical equilibrium position of a bead under the applied load of the trap when both assembly motors are attached to the microtubule under various binding configurations. In these calculations the axial stiffness of each motor is assumed to follow the functional dependence found via the single-kinesin fitting routine described above. A force equilibrium state solution was then used to calculate the forces experienced by each motor and the composite stiffness of the two-kinesin system over a range of motor-motor separation distances (Figure 3.22). The results show that the composite two-kinesin assembly stiffness depends on both the applied load and the distance between the two microtubule-bound assembly motors. The elasticity of a two-kinesin complex is found to largely follow the single-kinesin stiffness when separation distances are large (i.e., when one motor bears the load of the trap), and stiffnesses increase toward the idealized, equal load-sharing model as the motor separation distance decreases. The experimental data falls between these two regimes, suggesting the two-kinesin stiffness data is a measure of the average mechanical compliance of the two-motor system over a range of microtubule-bound configurations, many of which do not allow motors to share their load equally.

How the assembly-microtubule binding configurations influence the load distribution between two microtubule-bound kinesins was examined next. If the elastic linkages within a two-kinesin assembly are assumed to reach their mechanical equilibrium states in between motor stepping events, (Leduc et al., 2007), distributions of loads between motors can be evaluated via a modeling procedure that calculates the equilibrium position of the bead given a specified load, the force dependence of κ_{mot}, and the separation distance between the two microtubule binding sites (Figure 3.23 and Figure 3.24). To capture generic elastic properties of the two-kinesin assemblies, load distributions were calculated for assemblies bound in an 'in-line' configuration (i.e., both motors are bound to the same microtubule protofilament, one motor in front of the other). The predominance of such configurations to bead motion is implied by the two-kinesin stiffness analysis (the composite two-kinesin stiffnesses in Figure 3.22 are in a regime that fits configurations where one motor is tens of nanometers in front of the other) and evidenced more directly by evaluations of rearward displacements during partial assembly detachment events (Figure 3.8).

An illustration of a representative two-kinesin assembly configuration at mechanical equilibrium is depicted in Figure 3.23 (F_{trap} = 5 pN, binding-site separation distance = 32 nm). Here, significant deviations from equal-load-sharing behaviors are clearly found. The 'leading' motor must stretch a larger distance than the 'trailing' motor in order to reach the microtubule, and consequently, must assume a significantly higher portion of the load imposed on the bead than its 'trailing' partner (F_x = 3.4 pN and 1.6 pN for the 'leading' and 'trailing' motor respectively when F_{trap} = 5 pN).

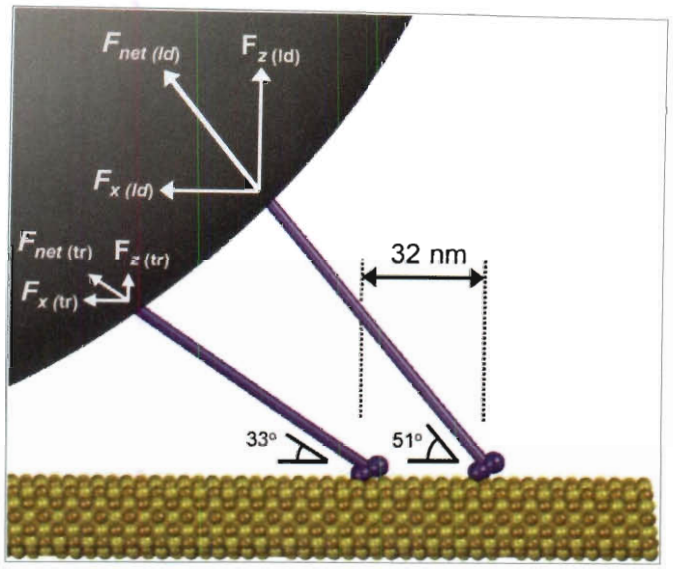

Figure 3.23: Illustration of a Two-Kinesin Assembly Configuration in Static Equilibrium

The two-kinesin assembly pictured is under a 5 pN load and has a binding site separation distance of 32 nm. The leading motor experiences substantially larger axial and perpendicular forces than the trailing motor: $F_{x(ld)}$ = 3.4 pN, $F_{z(ld)}$ = 4.2 pN; $F_{x(tr)}$ = 1.6 pN, $F_{z(tr)}$ = 1.0 pN.

Overall, two general trends were identified that describe how applied loads are distributed between kinesins in an assembly. First, when both motors are bound to a microtubule and bear load, the presence of the 'trailing motor' causes the angle between the 'leading motor' stalk and the microtubule axis to increase relative to that of a single kinesin experiencing the same applied load, which should affect motor velocity (Fehr, 2008). Concomitantly, the leading motor experiences a larger upward force (perpendicular to the microtubule axis) which will influence motor-microtubule detachment rates (Gittes, 1996). Second, the difference between the axial (rearward) loads assumed by each motor is very sensitive to the distance between the microtubule-binding sites of the two motors (Figure 3.24). An 'optimal' separation distance can be found where the applied load of the trap is distributed near-equally between the two motors, but deviations from this distance by even one unit of motor step size (8 nm) can lead to pN-sized differences in the loads imposed on the motors. Together, these results imply that there are consequences if motors within an assembly deviate from specific microtubule-bound configurations that optimize the way forces are distributed within the motor system. Importantly, such constraints appear to be significant over a range of assembly structures (scaffold lengths or inter-motor distances, bead diameters or cargo sizes, and assembly elasticities, see Figure 3.25 and Figure 3.26).

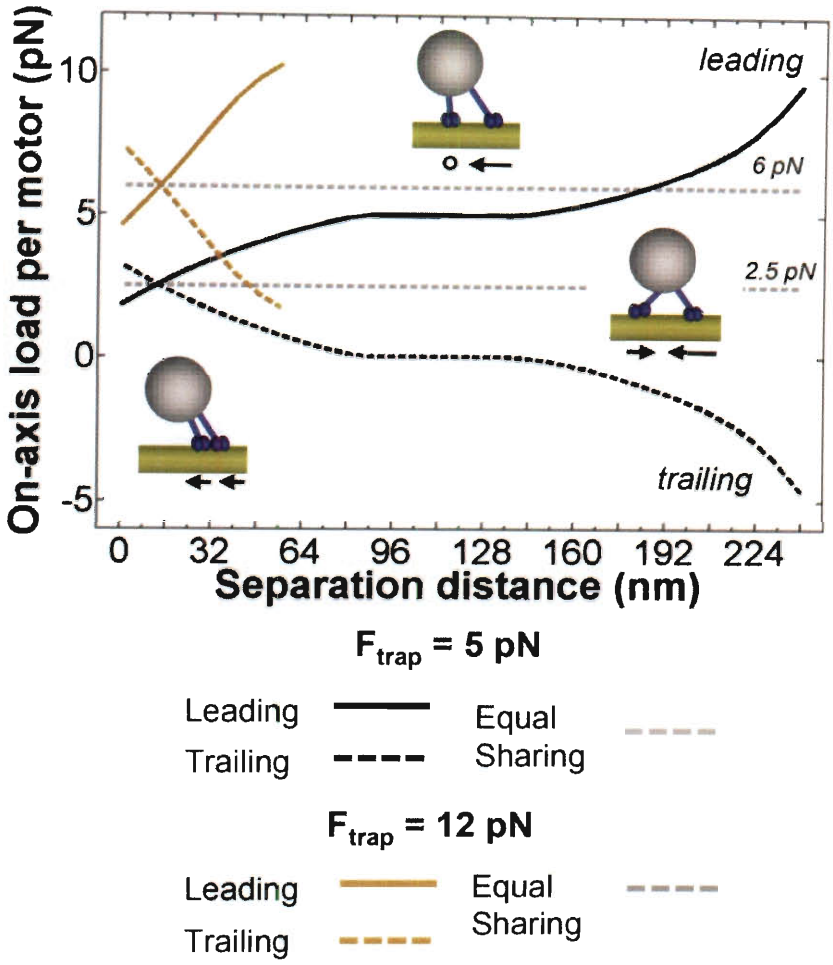

Figure 3.24: Configuration-Dependent Load Distributions among Motors in Two-Kinesin Assemblies

Model predictions of the rearward component of applied load imposed on the leading and trailing assembly motors plotted as a function of motor-microtubule binding site separation distances. Calculated force trends for total applied loads of 5 pN (*black*) and 12 pN (*tan*) are shown.

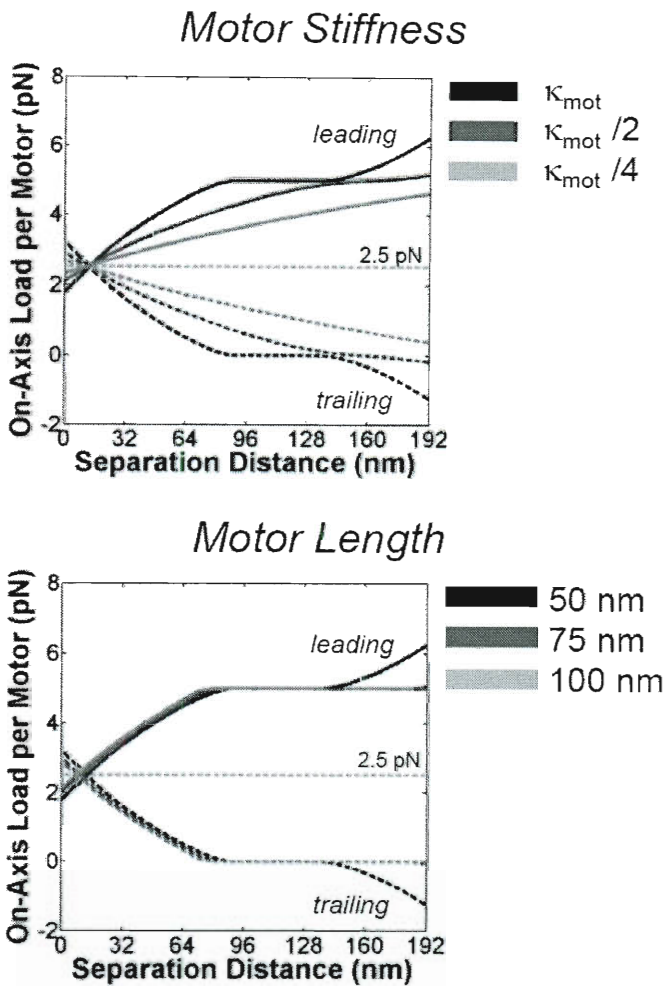

Figure 3.25: Load-Sharing within Two-Kinesin Assemblies: the Effects of Motor Stiffness and Length

Calculated forces imposed on the leading and trailing motors in two-kinesin assemblies as a function of motor separation distances. Non-equal load sharing is found for a wider range of motor stiffnesses (κ_{mot}), inter-motor distances, motor lengths, and bead sizes. The black line in each plot corresponds to the values presented in Figure 3.24.

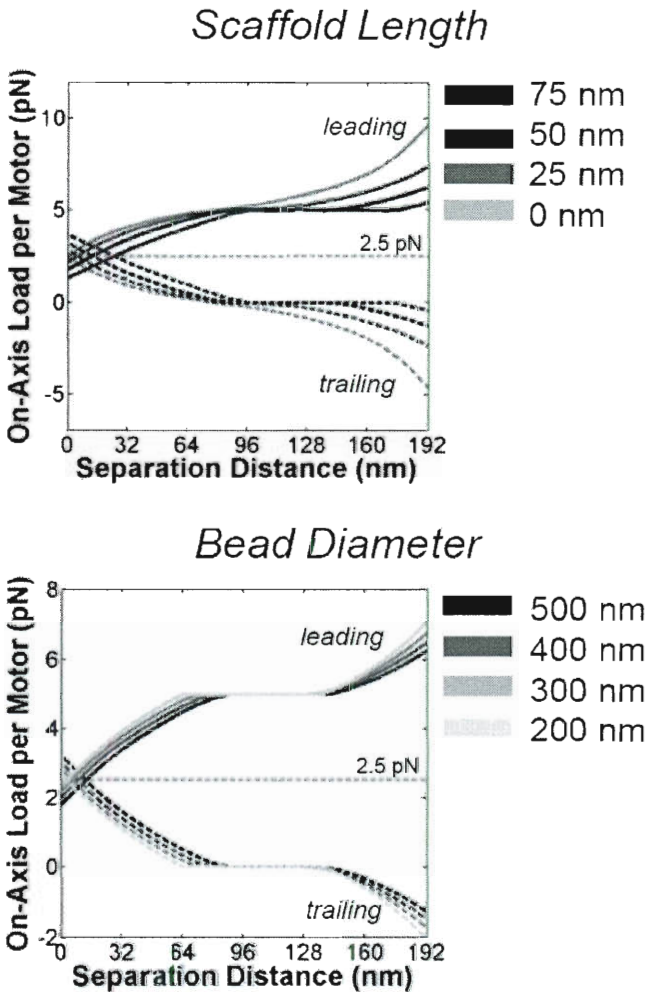

Figure 3.26: Load-Sharing within Two-Kinesin Assemblies: the Effects of Scaffold Length (Inter-Motor Separation) and Bead Diameter

3.9. Cargo Displacement Magnitudes Depend on Microtubule-Binding Configuration

To further characterize how a motor assembly's microtubule-binding configuration influences cargo motion, two-kinesin assembly stepping behaviors were examined under the applied load of the trap. Single kinesin molecules are known to advance in discrete 8 nm steps (Figure 3.27and Figure 3.28; Svoboda, 1993; Yildiz, 2004). Unless a group of kinesins synchronize their stepping, cargo displacement magnitudes are expected to be smaller than 8 nm (Leduc, 2007; Rogers, 2009). Furthermore, actual cargo displacement sizes should depend on how multiple motors are bound to their filament track.

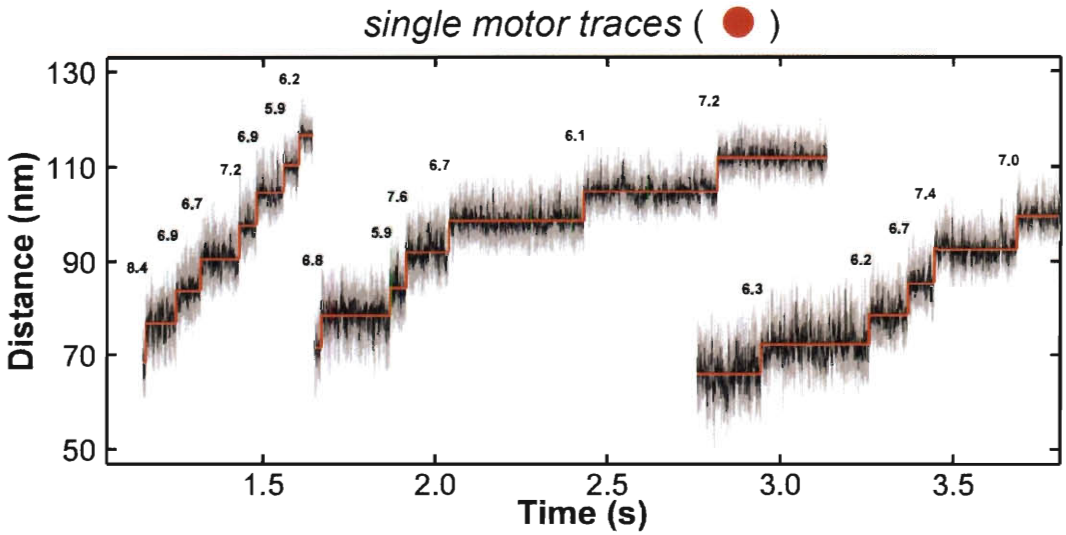

Figure 3.27: Single Kinesin Example Bead Displacements

Single kinesin stepping traces and steps using a step finding algorithm (Kerrsemakers, 2006). Individual fitted step sizes are indicated next to each trace identified step.

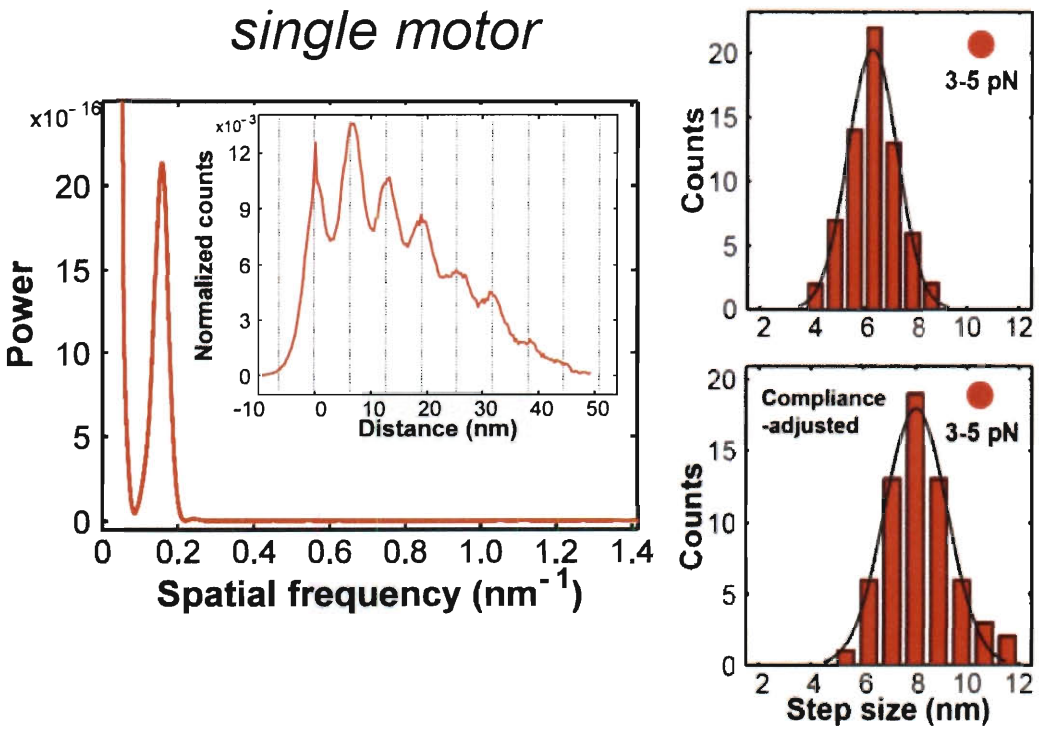

Figure 3.28: Analyses of Single Kinesin Displacement Sizes

A pairwise distribution histogram constructed from single-kinesin traces (e.g., Figure 3.27) and the corresponding spectral analysis is shown in the left panel (see Section 3.9.1 for a description of the analytical methods). Displacement sizes found using a step-finding algorithm are also presented, both with (lower panel) and without (upper panel) adjustments that account for the stretching of microtubule-bead linkages (see Figure 3.33 and Section 3.9.4). The peak in the bottom plot corresponds to the kinesin motor step size: 8.2 ± 0.3 nm, mean ± s.e.m.

To understand the influence of an assembly's microtubule-binding geometry on bead advancement, a mechanical modeling procedure was used to calculate the distances beads move under load when the binding-site separation distance between assembly motors changes by 8 nm; a simulation of asynchronous stepping. These analyses revealed that beads can advance in unitary (8 nm) or attenuated (< 8 nm) increments depending on: (*i*) the separation distance between the assembly motors' microtubule binding sites, (*ii*) whether the 'leading' or 'trailing' assembly motor steps forward, and (*iii*) the total applied load imposed on the bead (Figure 3.29). Despite these complications, three characteristically different types of stepping behaviors can be identified that largely depend on the microtubule-binding site distances between the assembly motors as described below.

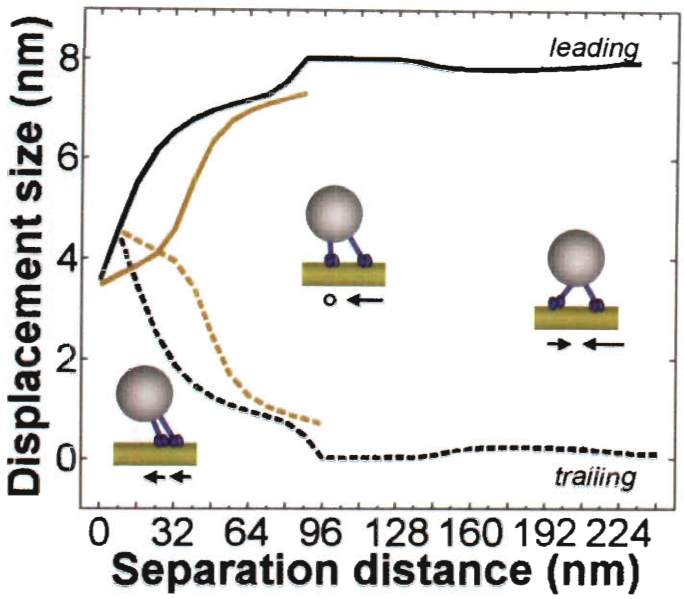

Figure 3.29: Predicted Displacement Sizes for Two-Kinesin Beads as a Function of Separation Distance

The total applied load in these model calculations was either 5 pN (*black lines*) or 12 pN (*tan lines*) for the leading motor (solid lines) and trailing motor (dashed lines) stepping forward as part of a two-kinesin complex.

When the kinesins are bound in close proximity, bead displacement magnitudes are significantly smaller than 8 nm. Under these conditions, both assembly motors adopt a portion of the applied load imposed on the bead. When a motor steps, the microtubule-bead linkages in the assembly will stretch or relax as the distances between the motors change, and the assembly center of mass moves forward a fraction of kinesin's unitary step size. Yet, at intermediate separation distances (approximately 100 nm), the model predicts that the displacement sizes of single-kinesin and two-kinesin beads will be nearly identical. In this regime, the 'leading' motor bears almost the entire applied load on the bead, and should be able to advance as a single motor with a partner that largely does not contribute to bead motion. A similar circumstance is found when motor binding site distances are large (approximately 150-250 nm), except that in this case, the 'trailing' motor 'lags' behind the motion of the bead and imposes a resisting load on the 'leading' motor. Although one might expect attenuated displacements to be produced in this circumstance, we found that beads rotate forward in these motor-microtubule binding conditions and this rolling motion contributes significantly to displacement sizes in this regime, consequently, the beads still tend to advance forward in increments equivalent to kinesin's step size; attenuated displacement sizes (at large inter-motor separation distances) are found when the center position of the scaffold is instead used as a reference point (Figure 3.30).

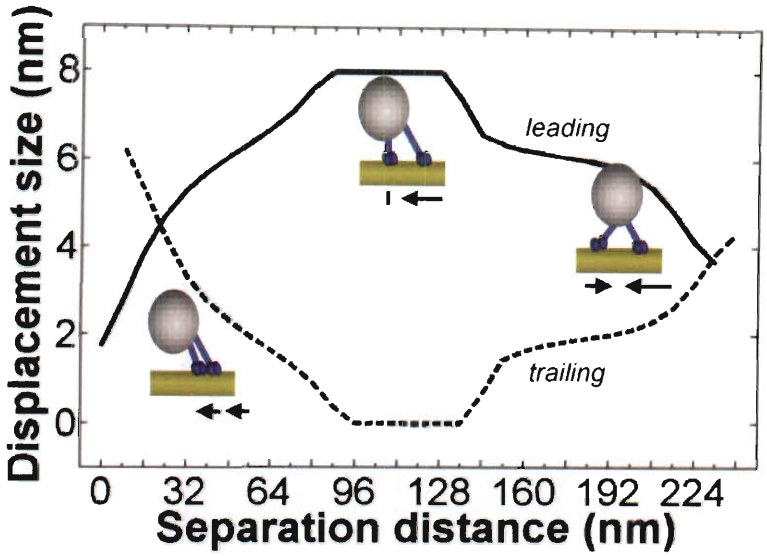

Figure 3.30: Predicted Displacement Sizes of the Center of Geometry for Two-Kinesin Assemblies as a Function of Separation Distance

The total applied load in these model calculations was either 5 pN (*black lines*) or 12 pN (*tan lines*) for the leading motor (solid lines) and trailing motor (dashed lines) stepping forward as part of a two-kinesin complex. In this figure the center of geometry of the two-kinesin assembly is used as a reference for displacements rather than the center of the attached microsphere. These displacements do not represent lateral motions of the transported bead but rather forward displacements of the assembly itself (i.e., not accounting for bead rotations that occur concomitantly).

3.9.1. Analytical Approaches to Interpret Bead Displacements

To analyze bead displacement sizes for single-kinesin and coupled-kinesin assays full pairwise distributions were computed. In these distributions the distance between every pair of points in bead displacement time traces were calculated and histograms built to display the frequency of point-to-point distances. Bead trajectories that are composed of repeated steps of a single size will display a clear periodicity in the pairwise histogram (Svoboda, 1993) with peaks occurring at multiples of the underlying step size (e.g., beads driven by a single kinesin show a periodicity of ~6.4 nm in our assays corresponding to the characteristic kinesin step size before compliance adjustment). In contrast, bead trajectories that contain multiple step sizes will produce pairwise distributions with multiple periodicities that are not as visually apparent (e.g., beads driven by two kinesins move forward with a variety of step sizes). It is also important to note that the appearance of a pairwise distribution is highly dependent on the time traces selected; the relative height and width of distribution peaks depends on the relative dwell times of steps and their location with a time trace. Therefore, for these analyses the pairwise distribution of several time traces (4-6) were summed and normalized to generate distributions representative of each data set.

The underlying bead step size(s) in time traces can be determined by computing the power spectra of pairwise distributions. To compute each power spectrum the pairwise distribution magnitudes were multiplied by a Modified Bartlett-Hanning window and the discrete Fourier transform was determined using a fast Fourier

transform algorithm. The resulting power spectra display peaks at the inverse of the step size(s) present in the bead displacement data (e.g., 4 nm steps in displacement data would produce a peak at 1/4 nm = 0.25 nm^{-1}).

Bead displacement magnitudes were also examined using a previously developed step-finding algorithm based on a chi-squared minimization technique (Kerrsemakers, 2006). The standard deviation of bead position dwells between identified steps was measured as an indicator of experimental noise. Single-kinesin steps have a measured positional standard deviation of 2.3 nm (Figure 3.27 and Figure 3.28). Low-velocity and high-velocity microstates of coupled-kinesin traces have a measured s.d. of 2.3 nm and 1.6 nm respectively (Figure 3.31 and Figure 3.34). Importantly, a previous evaluation of step-finding algorithms using simulated data has shown that at the noise levels observed in these experiments and with the step-finding algorithm utilized approximately 90% of full kinesin steps should be correctly identified (Carter).

3.9.2. Bead Displacements Reveal Dominant Asynchronous Stepping of Two-Kinesin Assemblies

Analyses of two-kinesin stepping behaviors largely confirm the calculated theoretical predictions. First, pairwise distributions and step-size histograms of two-kinesin bead displacement sizes within trajectory components assigned to single-motor microstate configurations ('low' velocity components) contain a clear periodicity / step-size corresponding to 6.4 nm (Figure 3.31 and Figure 3.32). Note that similar results are

found in the single kinesin pairwise distribution and step size histograms, which exhibit a dominant periodicity/step-size of 6.3 nm (Figure 3.27and Figure 3.28). When single-motor elasticity data is used to adjust displacement sizes for the stretching of motor-bead linkages, a displacement magnitude of 6.3 nm equals kinesin's intrinsic 8.2 nm step size (see Figure 3.28 and Figure 3.33).

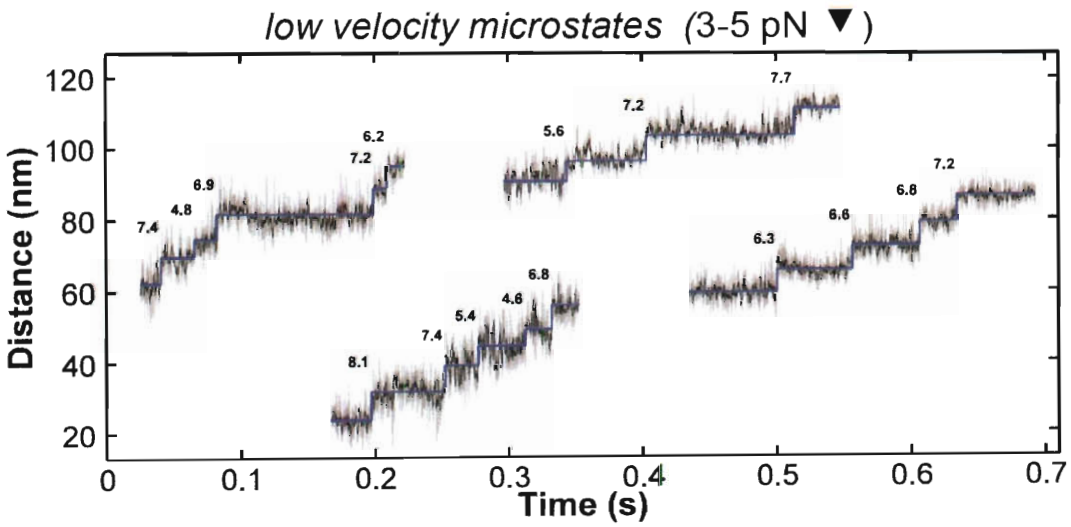

Figure 3.31: Example of Two-Kinesin Bead Displacements at Low-Velocity Microstates

Individual fitted step sizes are indicated next to each identified step.

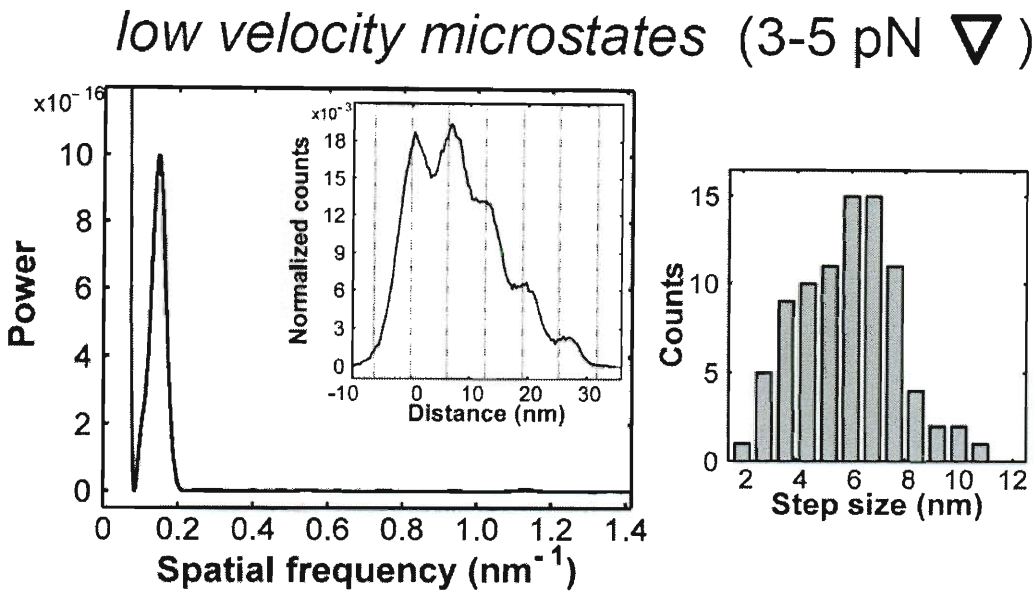

Figure 3.32: Analyses of Two-Kinesin Bead Displacement Magnitudes in Low-Velocity Microstates

Step-size distributions for two-kinesin assemblies when they move with 'low' (single load-bearing motor) velocities from 3-5 pN (corresponding to the forces for identified steps in single-kinesin traces). A bead displacement histogram, pairwise distribution and the corresponding spectral analysis is given. The inverse of spatial frequencies corresponding to spectral peaks indicates the dominant periodicities (step sizes) present in the pairwise distributions.

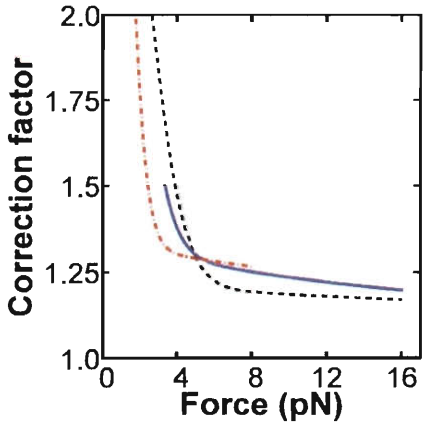

Figure 3.33: Compliance-Dependent Correction Factors for Single and Two-Kinesin Driven Beads

In a static-trapping assay beads are acted upon by the opposing forces of the optical trap and kinesin motor(s), each operating as a nonlinear spring. Using the power spectrum method, the stiffness of the entire system (k_{tot}) observed during static trapping assays was determined (see Figure 3.20) and the equation $k_{motor}(F) = k_{tot}(F) - k_{trap}$ was applied to find the load-dependent motor stiffness, similar to previous studies (Coppin, 1997). With k_{motor} known, the expression:

$$x_{motor} = x_{bead}((k_{motor} + k_{trap})/k_{motor}),$$

Equation 5: Definition of Correction Factors from Measurements of Trap and Motor Stiffness

where 'x' denotes position, can be used to determine *motor* position and velocity from experimental measurements of *bead* position, accounting for the mechanical compliance of the motor-bead linkage. The expression, $(k_{motor} + k_{trap})/k_{motor}$, is then a 'correction factor', which when multiplied by the measured bead displacement, x_{bead}, yields a measure for the displacement of single motor (or center of geometry for a two-kinesin assembly), x_{motor}. Note that with increasing force k_{motor} increases and the correction to x_{bead} correspondingly decreases. The figure shows the correction factor for single kinesins (red dash dot line), two-kinesins (solid blue line), and the theoretical correction for two-kinesins in a parallel-arrangement equal load sharing configuration (black dashed line). See Section 3.9.4 for further information on displacement and velocity corrections.

The agreement seen between single-kinesin bead displacements and low-velocity two-kinesin assembly bead displacements is expected, as displacements equivalent to kinesin's unitary step size should be produced when two-kinesin assemblies adopt configurations where only one assembly motor bears the applied load of the trap, regardless of whether one or both motors are microtubule-bound (see Figure 3.29 and Figure 3.30). Note that there appears to be some broadening in both pairwise displacement and step size distribution histograms of the low-velocity two-motor stepping data. This likely reflects variability in two-kinesin bead displacement magnitudes that arises from a percentage of events where assemblies adopted configurations in which the applied load is partially shared between the motors, but predominantly so by a single motor.

Significant agreement between calculated and measured two-kinesin bead displacement sizes (Figure 3.34) is also found at high forces (>12 pN), where motors must share the applied load of the trap to produce high-velocity forward motion.

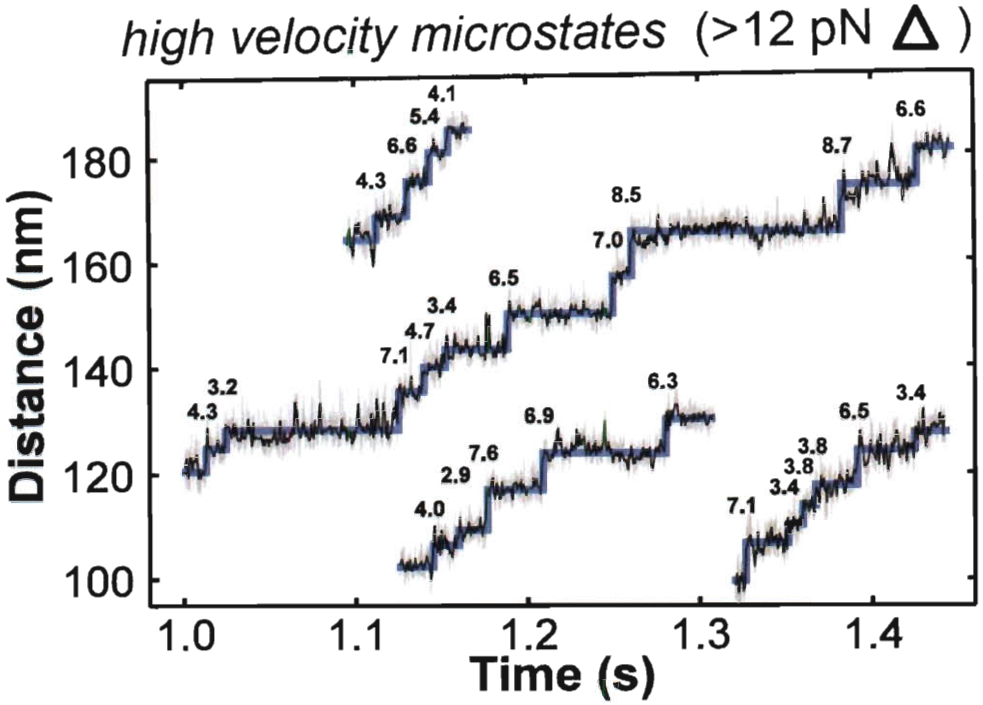

Figure 3.34: Representative Position Versus Time Traces for Two-Kinesin Assemblies in Two Load-Bearing Motor States

Each trace was median-filtered to 3 kHz (black) from 30 kHz raw acquisition (grey). The blue lines denote the average position of beads between instantaneous displacement events identified using a step-finding algorithm; corresponding step sizes are also displayed.

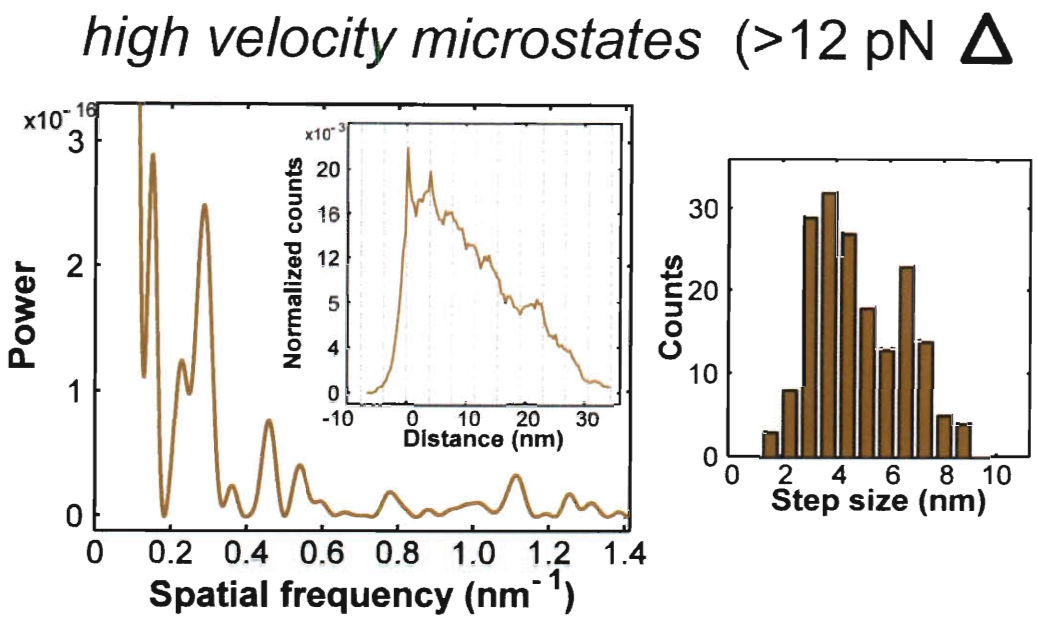

Figure 3.35: Analyses of Two-Kinesin Bead Displacement Magnitudes in High-Velocity Microstates

Step-size distributions for two-kinesin assemblies when they move with 'high' (two load-bearing motors) velocities above 12 pN. For each case, a bead displacement histogram, pairwise distribution and the corresponding spectral analysis is given. The inverse of spatial frequencies corresponding to spectral peaks indicates the dominant periodicities (step sizes) present in the pairwise distributions

Pairwise distribution histograms of high-velocity/high-force two-kinesin bead displacements possess a spectrum of small step sizes and also have a dominant 3.7 nm periodicity (Figure 3.35). Histograms of bead displacement magnitudes contain an equivalent 3.7 nm peak. In addition to the dominant ~4 nm peak in the step-size histogram, a second smaller peak at 6.8 nm is also observed; when this second peak is corrected for assembly compliances it corresponds to kinesin's intrinsic full 8 nm step size. However, this behavior suggests that either (1) single kinesins are stepping forward under super-stall conditions (which have never been observed in the literature) or (2) both kinesins in a two-kinesin assembly are stepping synchronously. Multiple kinesins are not known to step simultaneously and no mechanism has been identified which might facilitate communication between motors in a multi-motor system. To further examine the possibility that full (~ 8nm) displacement sizes are present in two-kinesin traces at high-forces, the step-finding algorithm was evaluated using simulated data (at the same noise level as the actual experimental data). This analysis revealed that approximately 15% of multiple motor "half-steps" (~ 4 nm) will be misinterpreted as larger full steps by the step-finding algorithm. Thus, a portion of this peak's magnitude (~50%) likely stems from undercounting of small stepping events and the dominant peak observed in the step size histogram displayed in Figure 3.35represents a lower bound for the probability that a two-kinesin assembly will advance forward by attenuated (<8 nm) steps.. While the possibility that two kinesins can coordinate / synchronize their stepping mechanics to some extent cannot be fully ruled out, it must be concluded that a group of two kinesins moving against large applied loads will

advance primarily via asynchronous stepping, in agreement with previous studies of membrane pulling (Campas, 2008). In fact, evaluation of the step-finding algorithm combined with integration of the spatial power spectrum for high velocity microstates indicates that > 85% of two-kinesin assembly steps will be asynchronous. Importantly, coupled with the analyses of load distributions within motor assemblies, this result highlights why it is so difficult for two-kinesin beads to sustain transport against large loads. Asynchronous stepping will lead to fluctuations in binding-site separation distance, and hence, create transient conditions that promote motor detachment.

3.9.3. The Probability of Two Stochastic Kinesins Spontaneously Stepping in Unison

An analysis of single kinesin motor dwell times was used to estimate the probability of the both motors within two-kinesins assemblies spontaneously stepping at the same time. The probability of two steps occurring simultaneously was calculated by the following equation:

$$P = \sum_{i,j=1}^{N} P(T_i)\left(\frac{t}{T_i}\right)P(T_j)\left(\frac{t}{T_j}\right),$$

Equation 6: The Probability of Two Kinesins Stepping Simultaneously

where '*N*' is the total number of single kinesin dwell times (*T*) in an experimentally measured distribution, 't' is the duration of a stepping event, and $P(T_i)$ is the probability of the i^{th} dwell time occurring within the distribution. In this analysis, dwell times correspond to steps reported in the single kinesin step size histogram found in Figure 3.28 and $P(T_i) = (1/N)$. This calculation is done in terms of the discontinuous probability

distribution of the experimental data set rather than a continuous exponential fit to the dwell time distribution (which would require the integral of a continuous dwell time probability function rather than summation of a discontinuous experimental histogram), due to a fit's dependence on data binning and for ease of calculation. While earlier reports show that a single kinesin stepping event lasts approximately 30 μs (Carter, 2005), the temporal resolution of these position vs. time traces is 0.34 ms after low-pass filtering and averaging. A t = 0.34 ms is therefore used to produce an estimate of the probability of simultaneous steps of 0.024%. By using the experimental temporal resolution in place of the actual duration of a stepping event the statistically expected occurrence of simultaneous steps is surely overestimated. Nevertheless, the 0.024% of stepping events expected to be simultaneous is many times less than the observation of 15 -35% simultaneous steps identified (calculated using the areas under the Gaussian fits in Figure 3.35 and the step-finding algorithm simulation described in Section 3.9.2). The apparent enhancement of simultaneous steps observed experimentally may be indicative of force communication between the two kinesins of an assembly, making one motor in an assembly more likely to step immediately after the other. This kind of communication would serve to balance the load shared between the two motors, particularly under large loads, where many asynchronous steps have the potential to increase the microtubule-bound distance between the motors and effectively impose super-stall forces against one motor within the assembly.

3.9.4. Compliance-Dependent Adjustments to Bead Velocities and Displacements

Measured stiffness values for a single kinesin (κ_{motor} as shown above in Figure 3.22) were used to calculate a correction factor $CF_{mot} = (\kappa_{mot} + \kappa_{trap})/ \kappa_{mot}$ that adjusts for motor compliance to determine a motor's step size and velocity from measurements of bead displacement ($x_{mot} = x_{bead} \bullet CF_{mot}$) as previously reported (Svoboda, 1994). The two-kinesin correction factor $CF_{assembly}$ was calculated using two-kinesin stiffness data as described above by substituting $\kappa_{assembly}$ for κ_{mot} in the CF calculation. These values were used to adjust bead velocities for motor/assembly stretching and to generate the compliance-corrected *F-V* plots in Figure 3.17. Note that in Figure 3.33 with increasing force, due to increased motor and assembly elasticities the correction factors correspondingly decreases, and therefore, corrections are small (<25%) in both cases when the applied load is larger than 5 pN.

3.10. Kinetic Transition Rates between Two-Kinesin Assembly Microstates

How rapidly two-kinesin assembly can transition between microstates with different numbers of load-bearing motors was evaluated by combining a method to analyze motor-microtubule detachment kinetics (Coppin, 1997) with the ability to identify transitions between velocity sub-populations (Figure 3.36). Again, the above analyses show that low (single load-bearing motor) velocities can be produced regardless of whether one or both two-kinesin assembly motors are attached to the

microtubule. When both motors are microtubule-bound, their binding-site separation distances dictate load distributions, and hence whether the system will move with low (single load-bearing motor) or high (two load-bearing motors) velocities. There are a number of configurations where both kinesins in an assembly are microtubule-bound yet move forward with single-kinesin (or slower) velocities. Thus, the measured rates must be considered as effective transition rates between different classes of assembly microstate configurations wherein either one or two motors bear the applied load, and are not purely defined as the rates at which the number of microtubule-bound kinesins change. That is, these rates are effective in the sense that they are not purely binding/unbinding rates that are based on the number of microtubule-bound motors. Rather, these rates (by virtue of the velocity transition analysis described in Section 3.5) are a measure of the frequency at which two-kinesin assemblies transition in and out of 'slow' and 'fast' (non-productive/non-load-sharing and productive/load-sharing) two-kinesin bound microstates. A 1→2 motor transition can result from an additional motor binding to the microtubule or from the lagging motor in the assembly catching up to decrease the inter-motor separation. Conversely, a 2→1 motor transition can be the result of a single motor detaching from the microtubule or a significant increase in the inter-motor separation that caused a decrease in assembly

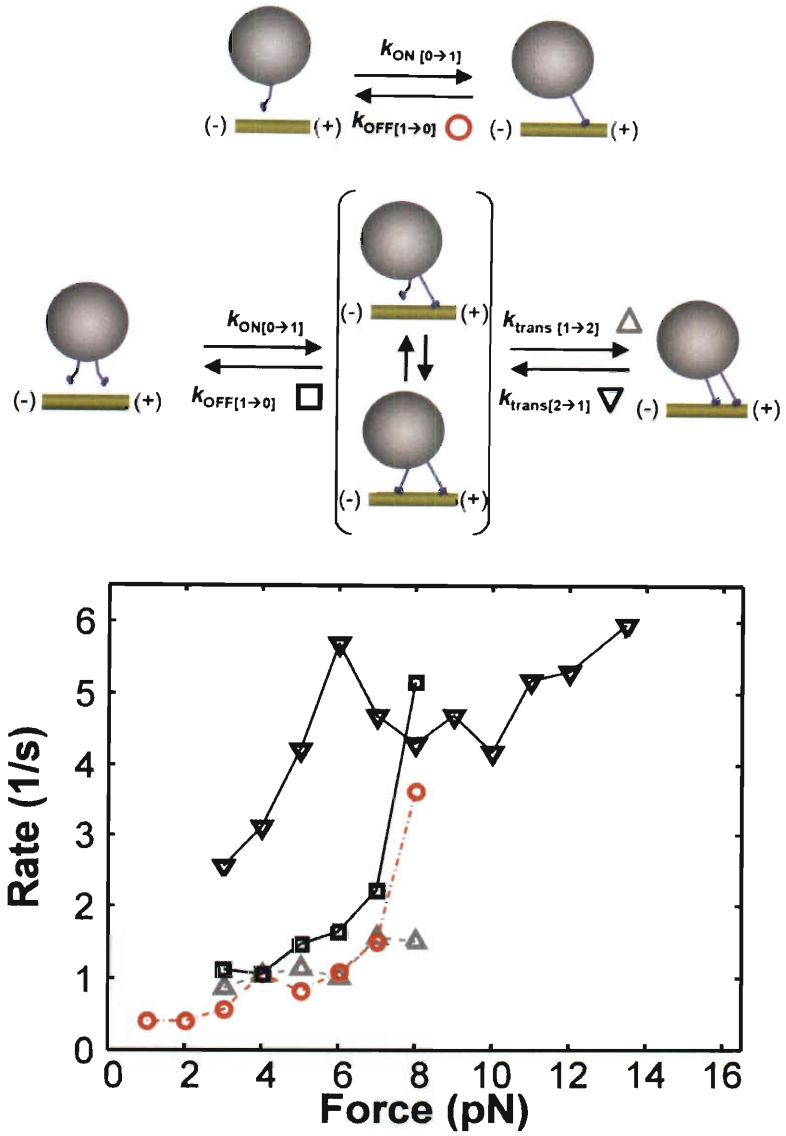

Figure 3.36: Single- and Two-Kinesin Binding/Unbinding Kinetics

A schematic of the microstate transitions for a two-kinesin assembly is given in the top of the figure. The subscript indices of each rate, *k*, specify the number of load-bearing motors present before and after the transition. In general, transition rates below 3 pN can not be identified because single-and two-motor load-bearing states at these velocities are too similar to readily identify velocity transitions. The symbols in the figure correspond to the specific transitions labelled in the upper schematic.

Summary of Chapter 3

Characterization of the transport capabilities of multiple-motor systems requires explicit knowledge of the structural arrangement of motors on their cargo. Engineered multiple-motor complexes were synthesized using DNA as a molecular scaffold and artificial protein linkers to connect two kinesin-1 motors together. By allowing several geometric and mechanical properties of the system to be defined, this system can serve as an experimental model for mechanistic studies of multiple motor functions. Optical trapping experiments that monitor the dynamics of the complexes demonstrated that two kinesins could generate forces in excess of the measured single-kinesins stall force (~7 pN). However, the complexes tended to detach from the microtubule at much smaller (sub-stall) forces. The generic inability of two kinesins to regularly generate large forces and transport with fast velocities is the result of the many microtubule-bound configurations these assemblies can adopt, most of which are not amenable to significant load-sharing among the two molecular motors. These effects are inferred from analyses of load distributions within the motor complexes. Here, experimental measurements of the elastic properties of single-kinesin and multiple-kinesin motor assemblies were used to evaluate how forces are distributed between the motors of the complexes over a range of microtubule configurations. Load-sharing only occurs if the motors are position closely together on the microtubule, an effect that applied to multiple motor complexes possessing a range of motor lengths/stiffnesses, inter-motor separation on cargos, and cargo sizes.

Analyses of cargo displacement sizes and the transition rates describing how fast a complex can change its microtubule-bound configuration also confirm this behavior. Cargo 'step' size analyses show that, under most loading-conditions (i.e. below the stall force of a single kinesin), two-kinesin assemblies spend the majority of their time in one several single load-bearing motor states. Yet, under super-stall conditions motors are found to step asynchronously. Further, assemblies are found to transition between single load-bearing and two load-bearing states much more slowly than the reverse transition. Thus, these results suggest groups of kinesin motors are largely incapable of cooperating effectively as a group. Such a weak sensitivity of transport processes to kinesin motor number has important ramifications for biological transport settings and offers an explanation for previously observed in vivo experimental results which find that several key transport activities are relatively independent of kinesin number.

Chapter 4

Productive Cooperation among Processive Motor Proteins Depends Inversely on Their Mechanochemical Efficiencies

Cytoskeletal motor proteins are molecular machines that consume ATP as fuel in order to produce the forces necessary to move vesicular and protein cargos directionally within the viscous and crowded environments of eukaryotic cells (Howard, 2001). Motor proteins are therefore central participants in mechanisms that control the spatiotemporal distributions of subcellular commodities in the cytoplasm and support normal cellular functions. Many microtubule motors are highly processive, and can transport cargos against piconewton-sized forces and over micron-scale distances before disassociating from their filament tracks (Carter, 2005;Hancock, 1998), suggesting they can function efficiently when acting independently as single motor

molecules. Yet, despite these properties, processive motors often operate in groups *in vivo* (Ally, 2009; Klumpp, 2005; Kulic, 2008; Holzbaur, 2010, Hirokawa, 1998), which raises questions regarding the extent to which collective motor protein dynamics influence intracellular transport processes. It is likely that cells rely on the combined action of multiple motors to surmount transport challenges requiring high-force production or long distance transport (Klumpp, 2005). This presupposition is even more marked given that there is evidence that some transport defects associated with motor mutations can be more pronounced when cargo transport is driven by large numbers of motors (Ori-McKenney, 2010). Moreover, beyond being the primary effectors of transport, collective motor dynamics itself may also help to regulate cargo motion (Levi, 2006; Hendricks, 2010). Motor teams composed of multiple, oppositely-directed kinesin and dynein motors transport cargos bidirectionally (cargos switch spontaneously between anterograde and retrograde transport directions). Bidirectional motility has been implicated in playing critical roles in higher-order physiological functions as well as error-correction mechanisms that ensure cargo is delivered to the appropriate location (see Section 1.2.1), and the net transport direction of these cargos can be controlled if the number of kinesins and dyneins that are engaged in transport is regulated such that one motor team has a net advantage over the other (Levi, 2006; Hendricks, 2010; Soppina, 2009). Together these insights into collective motor function highlight the potential role of motors in regulatory mechanisms.

The role multiple-motor dynamics play in intracellular transport naturally depends on the extent to which grouping motors together enhances motor function (i.e., increased force production, velocity, or cargo-filament affinity over single motor molecules). Until recently, characterizing the force-dependencies of multiple-motor motility has been challenging since it is difficult to determine the number of motors bound to moving cargos. However, several groups have developed experimental methods that facilitate more detailed studies of the impact of motor number and various biochemical and mechanical factors on cargo transport (Leduc, 2007; Rogers, 2009; Jamison, 2010; Shubeita, 2008; Ali, 2008). In two of these studies, our laboratory examined the collective dynamics of structurally-defined motor complexes composed of two kinesin-1 molecules (Rogers, 2009; Jamison, 2010). Overall, this work showed that molecular assemblies of two kinesins tend not to transport cargos over the distances or produce the forces that are expected of a cooperative team. Instead, despite kinesin's efficiency and high processivity, the complexes tended to transport their cargos while primarily using only one motor at a time (i.e., the motors cooperate negatively).

Although the weak dependence of cargo transport on kinesin copy number can be attributed to geometric effects that reduce the ability of multiple motors to share their applied loads (Jamison, 2010; Korn, 2009), the reason such effects are so pronounced for multiple kinesins remains unclear. Motors on a cargo's surface can bind to a range of different microtubule filament lattice sites, many of which are positioned far apart from one another (tens of motor step size units). The distance separating the

motors dictates how applied loads are distributed between them. When motors are far apart, the leading (front) motor bears the majority of the applied load, and load sharing only occurs if motors occupy closely-spaced microtubule lattice site positions, this is especially the case for spherical cargos. To cooperate productively, trailing kinesins therefore face the challenge of catching up to their continually-advancing leading partners before either motor releases from the microtubule. Naturally, a motor's microtubule-bound lifetime will influence this process (Korn, 2009). However, both the mechanical (elastic) and mechanochemical properties of molecular motors are known to vary nonlinearly with force, and the evolution of a motor group's microtubule-bound geometry should also depend on interdependent relationships between these properties. Furthermore, applied loads imposed on cargos in cells may either be relatively static or highly dynamic, as is the case when antagonistic motors compete and stretch their cargos (Soppina, 2009). In the latter circumstance, the role of loading rates that cargos impose on motor groups must also be considered. Thus, understanding the cooperative dynamics of multiple kinesins and that of other processive motor types ultimately requires detailed and accurate parameterization of transport models that account for competing factors that influence motor dynamics.

In this chapter a model of multiple-motor dynamics that predicts the load-dependent transport properties of cargos from detailed measurements of single-kinesin velocities, detachment rates, and elasticities (see Chapter 3) is presented. Using these data, the model can account for single-motor stepping behaviors, steady- and non-

steady-state kinetics describing motor-filament detachment, and strain-induced stiffening of motors and their resultant nonlinear, force-dependent elasticities in predicting collective motor behaviors. As a test case, the transport properties of structurally-defined two-kinesin complexes were evaluated s compared to model predictions. The model reproduces key signatures found in optical trapping experiments; namely, multiple-kinesin transport complexes are typically driven by a single unassisted kinesin motor molecule. Although this behavior arises from generic kinetic and geometric constraints, the model predicts such effects are enhanced when the applied load on a cargo increases in time. In contrast, processive motors whose stepping mechanism is less efficient than kinesin's are found to cooperate much more productively regardless of the loading rate and even while the same geometric constraints that promote negative cooperativity among multiple kinesins still apply. Thus, 'weaker' processive motors (e.g., dynein) may cooperate more productively as a team, making cargo transport more sensitive to their number than to that of kinesin.

4.1. A Discrete-Microstate Model for Multiple Motors

4.1.1. Defining Microstate Energies of Multiple-Motor Systems

In this modeling procedure, a system of master equations describing the time-dependent progression of cargos against an applied load are computationally solved as multiple-motor complexes transition between different microtubule-bound configurations (microstates; see Figure 4.1).

As expected, all forms of two-kinesin assembly and single-kinesin detachment rates are found to increase as a function of applied load. Importantly, the transition rates $k_{OFF[1\rightarrow 0]}$ measured for two-kinesin beads are higher than the corresponding single-kinesin detachment rates, indicating inter-motor interactions enhance motor detachment in the two-kinesin system. Furthermore, below kinesin's stall force, the transition rate $k_{trans[2\rightarrow 1]}$ describing how rapidly assemblies switch from 'high-velocity' (two load-bearing motors) microstates to 'low-velocity' (single load-bearing motor) microstates is found to be significantly larger (> 3x) than the rates of single-kinesin detachment. Moreover, the rate $k_{trans[2\rightarrow 1]}$ is much faster than the rate assemblies transition back into microstates where both motors assume a portion of the applied load ($k_{trans[1\rightarrow 2]}$). Together, these measurements of $k_{trans[2\rightarrow 1]}$ and $k_{trans[1\rightarrow 2]}$ further confirm that assembly configurations where both motors are engaged in transport are rare and short lived ($k_{trans[2\rightarrow 1]}$ demonstrates that assemblies quickly lose two load-bearing motor states while $k_{trans[1\rightarrow 2]}$ reveals that assemblies much less frequently bind or walk into load-sharing states), and this again supports the conclusion that two kinesins primarily transport their cargo through the action of a single load-bearing motor.

The transition rates describing the addition of a second load-bearing motor, $k_{trans[1\rightarrow 2]}$, were also found to be significantly lower than the values commonly used to approximate the rates at which motors bind to microtubules ($k_{on[1\rightarrow 2]}$). This rate is often assumed to be load-independent at ~5 s^{-1} (Klumpp, 2005). Yet, when considering the effects of motor-microtubule binding geometry, the attachment of a second assembly

kinesin does not necessarily result in load sharing or high cargo velocities, since the motors must close any gap between their microtubule binding sites that prevents them from both contributing to force production. It is therefore possible that when defined purely by motor binding, the rate $k_{on[1\rightarrow 2]}$ can be significantly larger than the observed transition rate $k_{trans[1\rightarrow 2]}$.

3.10.1. Calculation of Transition Rates between Different Microstate Configurations of Two-Kinesin Assemblies

Transition rates were determined by a method analogous to previous reports (Coppin, 1997) with some exceptions. The different rates at which two-kinesin assemblies transition between distinct classes of microtubule-bound configurations (*defined by whether beads move with 'low' or 'high' velocities in the optical trap, and hence, whether one or two motors bear the applied load*) were determined as follows: the force-dependent rate at which assemblies switched from microstates with a single load-bearing motor to those where both motors bear the applied load, $k_{trans[1\rightarrow 2]}$, was determined by dividing the number of measured low-to-high velocity transitions by the total amount of time spent in a low-velocity state within any force bin. Correspondingly, the reverse rate, $k_{trans[2\rightarrow 1]}$, was determined by summing the number of high-to-low-velocity transitions and the number of complete microtubule dissociations that occurred when beads moved at high velocities, and then dividing by the total amount of time spent at high velocity within a force bin. The rate that a single load-bearing kinesin detached, $k_{OFF(1\rightarrow 0),}$ was calculated separately for both single-motor and two-kinesin

data. While $k_{OFF(1\rightarrow 0)}$ was determined from all detachment events recorded in single-kinesin assays, the two-kinesin $k_{OFF(1\rightarrow 0)}$ rate was determined from analyses of complete two-kinesin bead detachments. Again, it is important when analyzing these transitions to remember that the above rates are effective in that they describe transitions between states where zero, one, or two kinesins drive transport, regardless of the number of microtubule-bound kinesins within a state.

3.11. Implications of Optical Trapping Experiments on Interpretations of Endogenous Intracellular Transport

By studying the load-dependent properties of structurally-defined assemblies of two kinesins, collective kinesin dynamics have been resolved that provide new insight into the dependence of cargo transport on kinesin number. Importantly, several lines of evidence presented here confirm the successful examination of *individual* two-kinesin complexes. In particular, two-kinesin beads were observed to: (1) regularly produce forces greater than the single kinesin 'stall' force (see Figure 3.7 and Figure 3.12), (2) detach via a two-state unbinding process that reflects the engineered assembly architecture (see Figure 3.8), and (3) display bi-modal velocity distributions under low loading conditions where one or two kinesins can produce forward motion and a single-Gaussian distribution of velocities at large loads that require the simultaneous action of two kinesins to produce forward motion (see Figure 3.15), among other signatures.

The ability to attribute transport events to a kinesin complex with a defined number of motors allows the average behaviors of multiple-motor systems to be examined with minimal complications originating from variability in the total number of motors and/or their organization on the surface of cargos. Overall, such analyses show that, despite a capacity to produce large forces and move with high velocities, two kinesin-1 motors will tend to transport their cargo using only one load-bearing motor molecule at a time. Thus, grouping kinesins does not necessarily result in appreciable gains in cargo velocities and detachment forces on average, and hence, cargo transport may depend weakly on kinesin number, at least when the total number of motors is small.

Noncooperative multi-kinesin function of the kind observed in this study is not unprecedented in early experimental investigations. Some *in vitro* experimental data supports this type of motor recruitment. For example, while *in vitro* gliding assays conducted on kinesin-coated surfaces show no velocity dependence on surface motor density over the range of 1 – 1000 kinesins/μm^2 (Vale, 1985), gliding assays conducted in highly viscous media demonstrate that at correspondingly higher loads greater surface motor density generates increased gliding velocities (Hunt, 1994). These experiments describe a condition where greater transport demands may have the potential to cause the enlistment of motor proteins to bring about increased performance. From an energetics viewpoint it would be beneficial if motor proteins evolved to recruit additional motors for cargo transportation only when additional force-generation is needed. Such a mechanism would prevent wasteful consumption of

ATP for movement of cargos when a single motor can suffice. The multi-motor behaviors observed in this study meet this description; while high-velocity/high-force transport is rarely seen, cargos facing an obstruction impassable by a single motor can expect the recruitment of additional motors after many repeated attempts to occur on a time scale of minutes.

3.11.1. Models for the Weak Dependence of Cargo Transport on Kinesin Number

Foundational models of collective motor dynamics have been established (Klumpp and Lipowski, 2005), and this framework has been extended to evaluate the effects of structural and mechanical properties of cargos as well as inter-motor interactions (Constantinou, 2009; Kunwar, 2008; Rogers, 2009). However, most model predictions to date have not been unambiguously confirmed by experiments. In general, existing theories suggest that grouping motors increases the average time that a cargo will remain microtubule-bound, yielding enhanced transport properties. However, these expectations are largely contingent upon assumptions that multiple motors do not interfere with one another and that they share their applied load equally. In contrast, the results presented here indicate that inherent properties of multiple-kinesin systems can result in unexpectedly weak collective motor behaviors and that such effects largely stem from the fact that the motors influence each other's dynamic properties.

Overall, the configuration in which a kinesin assembly binds to a microtubule was found to be the most important factor in determining how a group of kinesins will

transport cargos under load. As evidenced by the mechanical modeling efforts described here, two kinesins cannot easily produce forces or move with velocities in excess of those expected for single kinesins unless the distances between their microtubule binding sites are maintained within a narrow range (e.g., <24 nm, at an applied load of 12 pN, which is a span of only three microtubule-binding sites between motors). Otherwise, the 'leading' motor will assume the majority of the applied load and its detachment rate will significantly increase relative to an idealized case where the motors share the applied load equally. Furthermore, the transition rate analyses, particularly of rate $k_{on[1\rightarrow 2]}$, suggest that when an assembly switches between microstates via the attachment of a second motor, this motor will most likely bind to a site where it cannot contribute significantly to cargo motion (and most often does not close the distance between itself and the leading motor partner to share in the cargo load). Thus, a newly bound motor faces the challenge of catching its load-bearing partner before either motor releases from the filament track. This challenge is exacerbated by the fact that as the 'trailing' motor moves forward the leading motor will accelerate as its portion of the applied load decreases and experience increasingly larger upward forces that will lower its microtubule affinity. Thus, while possible, it may be difficult for two kinesins to perform the precarious balancing act required for a motor assembly to exhibit its full mechanochemical potential.

3.11.2. Implications for Transport of Endogenous Cargos

There are several significant similarities between the results presented here and those from recent *in vivo* studies of cargo transport (Levi, 2006; Sims, 2009). In particular, behaviors where grouping kinesins does not result in appreciably enhanced motility are consistent with studies of lipid droplet motility in drosophila embryos where motor copy number does not influence cargo transport significantly (Shubeita, 2008). Since these studies recapitulate such effects *in vitro*, this work suggests that the tendency for a group of kinesins to function while only using a small portion of their motors applies to a variety of kinesin-dependent processes in cells, and that the action of environmental or regulatory factors may not be necessary to produce this behavior *in vivo*.

Given the influence of multiple motor binding geometries on cargo transport, the role of a biological cargo's size, shape, and elasticity as well as how motors and motor types are anchored to their surfaces must still be considered. The two-kinesin assembly-bead artificial cargos in this study approximate the structural and mechanical properties of many natural cargos that are known to be transported by small groups of motors. In particular, the stiffness of the present kinesin assembly constructs, which is roughly half of the values reported for a full-length, wild-type kinesin motor (Kawaguchi, 2003), is designed to account for the compliance imparted to motor systems by biological cargos. The assemblies used for these experiments should approximate the mechanical properties of multiple kinesin systems bound to sub-cellular cargos with an

elastic modulus of approximately 10^6 Pa (this is the cargo surface elasticity that would impart the same overall assembly stiffness between two wild-type kinesins as measured in our motor constructs). Elasticities of this magnitude are found in many biological cargos such as: melanosomes (Bruno, 2008), certain vesicular cargos (Laney, 1997), and potentially ribonucleoprotein particles. Furthermore, analyses of the influence of cargo size, motor spacing and assembly elasticity (see Figure 3.25 and Figure 3.26) indicate that the effects of non-equal load sharing among motors will remain significant even if the molecular-scale properties of a motor assembly and its cargo deviate from those in the present system.

3.11.3. Implications for Intracellular Transport Regulatory Mechanisms

The similarities between single and multiple kinesin transport behaviors may largely exclude kinesin number from actively serving as a regulatory control point for cargo transport beyond the simple presence or absence of motors. However, such behavior is still significant and important to mechanisms that regulate cargo motion. For example, the average force that a group of kinesins detaches from a microtubule will significantly influence bidirectional cargo motility, where multiple kinesins and dyneins participate and compete in transport. There is some evidence that mammalian dyneins stall at significantly lower forces than kinesin-1 (Mallik, 2004), implying that extremely large groups of dyneins would be needed to compete with much smaller groups of kinesins (*by some accounts ~14 dyneins if only 2 kinesins are present*). Insensitivity to kinesin number can serve to mitigate this apparent imbalance between

dynein and kinesin motor capabilities and allow dynein number to act as a more sensitive control parameter to regulate bidirectional cargo motion. Of course, this prediction assumes that several aspects of multiple dynein mechanics will differ from those found with multiple kinesins. Indeed, there are unique features of dynein mechanochemistry (as is described in Chapter 4) at the single-motor level that can result in different collective behaviors (in terms of motor stepping, F-V trends, microtubule proto-filament tracking, and the role of accessory factors; Gennerich, 2007; King, 2000; Mallik, 2004). While understanding these aspects of intracellular transport requires further investigation, the ability to create structurally-defined assemblies of multiple motor molecules and assay their collective function at the single-assembly level should greatly assist these efforts.

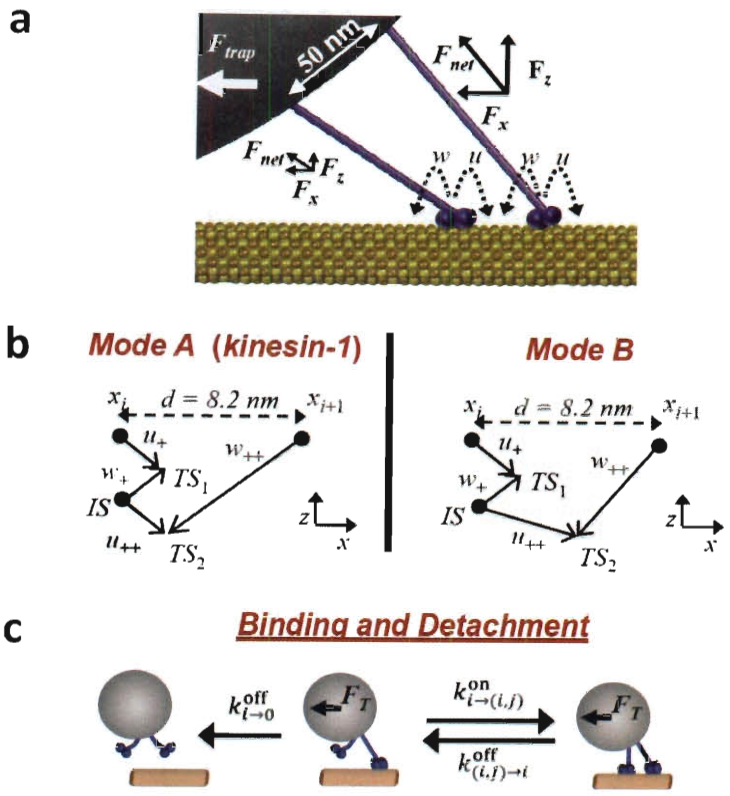

Figure 4.1: Stepping, Binding, and Detachment Transitions Enumerated in the Discrete-Microstate Model

(a) Illustration depicting a two-kinesin complex in a specific bound configuration with an inter-motor spacing = 32.8 nm, bead spacing = 50 nm, and F_{trap} = 5 pN. The bound geometry dictates how loads are distributed, which in turn affects the forward (u) and backward (w) stepping rates of each motor. (b) Two types of reaction coordinates used to calculate two-state motor stepping rates. Sub-steps involve displacements both along and perpendicular to the microtubule axis. For stepping mode A (corresponding to kinesin-1 motors), the positions of transition states (TS_n) for each sub-step and the intermediate state (*IS*) correspond directly to those previously reported (Fisher, 2005). For stepping mode B, the position of the second transition state (TS_2) was moved toward the final microtubule lattice site position (x_{i+1}). Importantly, this alteration causes the total forward stepping rate to decrease more rapidly with increasing load than is found with kinesin-1. (c) Illustration depicting microstate transitions involving motor binding and detachment. Subscripts are used to designate the lattice site positions of each motor (*i* specifies the position of motor 1 and *j* specifies the position of motor 2).

A key component of the modeling procedure lies in accurately defining the total strain energy of multiple-motor complexes in different microtubule-bound geometries (referred to as configurational energy: E_{config}). Since cargos transported by multiple motors advance in discrete increments (steps) characterized by extremely brief periods of motion (30 μs) between comparatively long dwells (Carter, 2005; Leduc, 2007), multiple-motor complexes were assumed to adopt persistent microtubule-bound configurations in between cargo displacement events. All linkages within a complex are also assumed to reach their mechanical equilibrium rapidly relative to the lifetime of the discrete microtubule-bound configurations of multiple motor systems (Leduc, 2007), and forces within a motor complex are therefore expected to be balanced and in static equilibrium in-between motor stepping, binding and detachment events. With these assumptions, microstate configurations of the motor complex can be designated by the number of bound motors and their positions along the microtubule. Complexes will transition between microstates stochastically, and the rates of these transitions will depend on the resultant difference in free energy between the initial and final configuration of the motor system (ΔE_{config}). The temporal evolution of the system can therefore be modeled probabilistically by enumerating all of the significant microtubule-bound configurations of the system and specifying the rates of transition between them.

To calculate E_{config} for each enumerated microstate, the microtubule-bound geometry of a motor complex and the center position of the bead are first determined using a modified version of the mechanical modeling procedure reported in Chapter 3.

Two-dimensional microtubule-bound geometries of the motor complexes are defined by specifying the positions of the motors on the bead and microtubule, as well as the axial (head-to-tail) elasticity of an individual motor unit. After making an initial estimate of the bead's position and orientation $\langle x_{B,o}, \theta_{B,o} \rangle$, the bead is 'relaxed' to its equilibrium position programmatically $\langle x_{B,eq}, \theta_{B,eq} \rangle$ by reiteratively moving it in the directions of the net forces imposed on it by the motors and the trap until a threshold is reached (< 0.001 pN), at which point the system is considered to be in equilibrium.

The above mechanical modeling procedure can also be used to fit single-motor stiffness data to determine a function $\kappa_M(\ell)$ describing the force-dependent elasticity of a single kinesin when it is stretched a distance, ℓ, along its head-to-tail axis. As a result, the effects from strain-induced stiffening of motor linkages observed in previous assays (Figure 4.2b and Figure 3.20; Fehr, 2009) can be accounted for in the calculation of E_{config}. Here, the unstretched length of the motor (ℓ_o) is assumed to be 50 nm (see Section 3.8.1). The function $\kappa_M(\ell)$ is found via a reiterative, nonlinear regression routine that uses the mechanical model to determine the component of $\kappa_M(\ell)$ along the microtubule axis over a range of applied loads. Errors between the predicted and measured motor stiffnesses are computed during each iteration of the fitting routine. The function $\kappa_M(\ell)$ is then adjusted to better approximate the data, new $\langle x_{B,eq}, \theta_{B,eq} \rangle$ and ($\kappa_{M,x}$) values are calculated, and the entire process is repeated until a best fit is achieved. The single-kinesin elasticity $\kappa_M(\ell)$ can be approximated by a sigmoid function,

which reflects that kinesins are anchored to beads via multiple mechanical elements (see Figure 3.1).

With $\kappa_M(\ell)$ known, values of E_{config} are then calculated as the sum of the potential energy of the bead in the trap and the work required to stretch each motor from its unstrained length to the extended length found in each microtubule-bound configuration of a complex:

Potential Energy of Optical Trap Strain Energy of a Motor

$$E_{config} = \overbrace{\frac{1}{2}\kappa_T(x_T - x_b)^2}^{\text{Potential Energy of Optical Trap}} + \overbrace{\sum_M \int_{\ell_o}^{\ell_o+\Delta\ell_M} \left\|\vec{F}_M\right\| d\ell}^{\text{Strain Energy of a Motor}},$$

Equation 7: Definition of Configurational Energy for Multiple Motor Sytems with an Applied Optical Load

where κ_T is the spring constant of the trap (κ_T = 0.055 pN/nm), $(x_T - x_b)$ is the displacement of the bead from the trap center, $\vec{F}_M$ is the force along the stalk of that motor from its tail to its head, and $\Delta\ell_M$ is the magnitude of a motor's extension from its unstretched length (ℓ_o).

4.1.2. Modeling Configuration-Dependent Motor Stepping Rates

The angles of the stalks of the motors (relative to the microtubule filament) within two-motor assemblies can differ greatly from the angle of single motor's stalk when it experiences the same applied load (see Section 3.8.2). Since stalk angles can affect motor velocity (Fehr, 2009; Gittes, 1996), motor stepping rates must be calculated using a model that accounts for the work done against a vectorial load. The model developed by Fisher and Kim assumes that kinesin's forward and backward stepping motions consist of two separate biochemical transitions (sub-steps) corresponding to displacements of the molecule in two dimensions (x and z; Fisher, 2005). Because the sub-steps involve motions of the molecule perpendicular to the axis of the microtubule (see Figure 4.1b), loads in this direction affect stepping rates. The position of the transition state in each sub-step determines the splitting of the work done along the reaction coordinate between the forward and reverse transitions. For each transition, conservation of energy allows the work to be calculated from the difference in E_{config} from the beginning to the end of the motor stepping path via:

$$u_{+} = u_{+}^{0}\, e^{-\Delta E_{config}(i \rightarrow TS_{1,i})/k_b T}, \qquad u_{++} = u_{++}^{0}\, e^{-\Delta E_{config}(IS_i \rightarrow TS_{2,i})/k_b T},$$

Equations 8: Definitions of Forward Sub-Step Transition Rates

$$w_{-} = w_{-}^{0}\, e^{-\Delta E_{config}(IS_i \rightarrow TS_{1,i})/k_b T}, \quad w_{--} = w_{--}^{0}\, e^{-\Delta E_{config}(i+1 \rightarrow TS_{2,i})/k_b T}.$$

Equations 9: Definitions of Backward Sub-Step Transition Rates

In these equations, u and w refer to forward and backward sub-step transition rates as defined in Figure 4.1. The notation $i \rightarrow TS_{1,i}$ indicates a partial step of the motor from position i to the transition state at $TS_{1,i}$, so that $\Delta E_{config}(i \rightarrow TS_{1,i}) = E_{config}(TS_{1,i}) - E_{config}(i)$. From these rates, effective full-step transition rates and subsequently average motor velocities can be calculated:

$$u = \frac{u_+ * u_{++}}{u_+ + u_{++} + w_- + w_{--}}$$

$$w = \frac{w_- * w_{--}}{u_+ + u_{++} + w_- + w_{--}}$$

$$V_M = d * (u - w),$$

Equations 10: Calculation of Full-Step Transition Rates from Sub-Step Transition Rates

where d is the full step size of the motor molecule (d = 8.2 nm for kinesin).

Assuming motors step asynchronously (see Section 3.9.3), their load-dependent stepping rates are calculated using the predetermined ΔE_{config} values describing transitions of motor complexes between different microtubule-bound configurations as each motor proceeds through all of its sub-step transitions, without any movement of the other motors. Thus, the only difference between this treatment and that of single motor molecules is that some of the change in configuration energy is stored in the motor's partner(s) according to the definition of E_{config}.

4.1.3. Specifying Distinct Motor Stepping Behaviors

To specify stepping rates for multiple kinesins, it was assumed that the positions of kinesin's stepping intermediate (IS) and transition states (TS_1 and TS_2) correspond to the values previously reported (Fisher, 2005; stepping mode A in Figure 4.1b). Forward and backward stepping rates for stepping mode A were determined from fits to measured single-kinesin optical trapping data (Figure 3.20 and Figure 4.2).

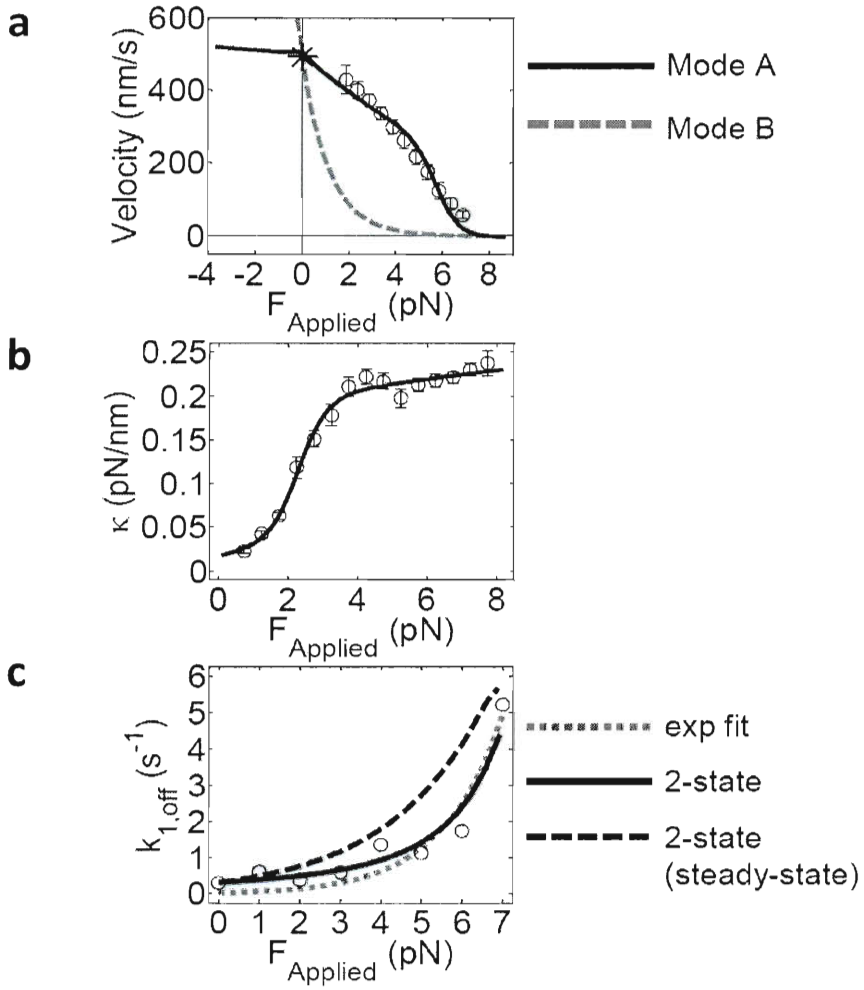

Figure 4.2: Parameterization of Motor Stepping, Elasticity, and Detachment Kinetics

(a) Single-motor *F-V* curves determined via a best fit of the kinesin-1 optical trapping data (see Figure 3.17) using stepping mode A (solid line through the data). Stepping mode B (dashed line) is plotted using the same parameters. (b) Experimental measurements (see Figure 3.20) and a best fit describing the force-dependent elasticity $\kappa(\ell)_x$ of a single-kinesin motor. (c) Single-kinesin detachment rates measured in an optical trap (κ_T = 0.055 pN/nm). Best fits are shown using a two-state detachment model describing load-rate-dependent motor unbinding (solid line), the corresponding steady-state detachment behavior (dashed line), and Kramer's theory (dotted line).

Here, the mechanical modeling procedure was used to calculate force-dependent ΔE_{config} values for a single motor moving along its stepping path through each IS and TS position. These calculations were performed over a range of forces such that the load on the bead (F_{ap}) spanned the single-kinesin F-V data. F_{ap} values and their corresponding load-dependent ΔE_{config} values are recorded during this procedure. Single-kinesin data can then be approximated using a fitting algorithm where the unloaded transition rate pre-factors in Equations 8 and Equations 9 are used as fit parameters. The truncated kinesin-1 constructs should possess the same basic stepping mechanism as wild-type kinesins, but their zero-load sub-step transition rates describe all biochemical aspects of the reaction that could be affected by other experimental factors.

The single-kinesin F-V fit presented in Figure 4.2 shows reasonable agreement with the measured trend and yields unloaded motor transitions rates that reflect kinesin's strong directional stepping bias: ($u_{+}^{0} = 1.59 \times 10^{14}$; $u_{++}^{0} = 61.7$; $w_{-}^{0} = 0.654$; $w_{--}^{0} = 1.69$). To evaluate how the curvature of a motor's F-V relationship influences multiple-motor behaviors, a F-V curve was also generated for motors possessing a slightly modified stepping reaction coordinate (Figure 4.2b; stepping mode B) where the position of the second transition state TS_2 in the original coordinate was moved towards the final lattice site of the step (i+1) by a distance of 3.0 nm. This alteration increases the amount of work performed during the second forward sub-step,

and primarily increases the sensitivity of the composite forward stepping rate to load, decreasing velocity (see Figure 4.2a).

4.1.4. Microstate Transitions via Motor Binding and Detachment

Average motor-microtubule detachment rates are commonly assumed to follow a load dependence described by Kramer's theory: $k_{off} = k_{off}^{0} \exp(F_{ap} \cdot \Delta s_d / k_b T)$, where Δs_d is the distance that a motor must move in order to release from the microtubule. However, this function does not reproduce our measurements of single-kinesin detachment rates (Figure 4.2c; dotted line). This disagreement likely occurs since the applied load changes in time during static trapping experiments according to the nonlinear force profile that is characteristic of optical traps; measurements of bond affinities between biomacromolecules typically increase with increasing loading rate (Evans, 2001). To address this, motor-microtubule detachment was treated as a two-state process that occurs along a reaction coordinate possessing two different energetic barriers. Such behavior is consistent with observations that kinesin motors bind to microtubule filaments in either weakly- or strongly-bound states (Mori, 2007). Barrier heights and the IS / TS positions along the motor unbinding reaction coordinate were determined by fitting single-kinesin detachment data using a procedure that solves a system of rate equations describing the time-dependent probability that a motor will be tightly- or weakly-bound. Since this method allows the reaction coordinate for motor detachment to be approximated, both steady- (constant load) and non-steady-state (load-rate-dependent) detachment rates can be calculated. Here, the predicted steady-

state curve can be approximated using Kramer's theory if the quantity $k_bT/\Delta s_d = F_d$ is 2.4 pN (Figure 4.2c; dashed line).

Capturing the load-rate dependence of motor detachment for multiple-motor systems ultimately requires detailed and cumbersome simulations to calculate the probability that a motor will occupy the different intermediate states along its unbinding reaction coordinate. These probabilities depend on the time-dependent progression of the loads motors experience as they bind to and step along the filament, and hence, the different trajectories taken by motors within a multiple-motor system. Nevertheless, load-rate dependencies can be approximated by considering generic constraints that dictate load-sharing behaviors. Since leading motors are expected to bear the majority of the applied load, their detachment rates will largely correspond to the non-steady-state (load-rate-dependent) curve in Figure 4.2c. Analogously, trailing motors will tend to follow the steady-state (constant load) trend until they assume an appreciable portion of the applied load, at which time, loading rates will become appreciable. Furthermore, average cargo velocities also influence loading rates and can also be used to choose between both behaviors accordingly. This reasoning was implemented for the simulations described below. Overall, these approximations allow a much simpler model of multiple-motor dynamics to be developed that incorporates the influence of load rates on multiple-motor microstate transitions.

Unloaded motor-microtubule binding rates were given their previously reported values, $k_{on}(F_{ap}=0) = 4.7\ s^{-1}$. However, as in an earlier discrete state transition rate model

(Driver, 2010), these rates were also assumed to depend on the difference in the configuration energies of a motor complex before and after individual motors bind the microtubule filament (microtubule lattice sites that require less motor stretching to be reached are more probable sites for unbound motors within multi-motor assemblies to bind into). These energy differences are calculated via the same procedure used to determine ΔE_{config} for motor stepping and detachment. Of note, the energy difference between the initial and final microstate configurations of a motor complex is split between motor binding and detachment as reported in the lab's earlier work (Driver, 2010). However, motor binding rates are now also influenced by bead displacements that arise from shifts of load-distributions between the microtubule-bound motors within a complex. Thus, binding rates are reduced by the work required to produce these displacements.

4.2. Theoretical Modeling Reveals Molecular Motor Efficiency Determines Collective Transport Behaviors

4.2.1. Comparisons Between Motor Theory and Experiment

The present model reproduces several key results found in the static optical trapping studies of two-kinesins assemblies (Chapter 3). First, two-kinesin complexes most commonly detach at forces near the 7 pN stalling force of a single kinesin motor (Figure 4.3a). The detachment behaviors of multi-kinesin complexes are presented as a breakdown of various categorical detachment events (Figure 4.3a): those caused by the release of a leading, trailing, or singly-bound motor within a complex, as well as the sum of all events. This distribution shows that partial/full complex detachments are most prevalent at or near the stalling force of a single kinesin. Note that it is necessary to be cautious when making comparisons between the experimentally measured and theoretically predicted detachment behaviors of multiple-motor complexes since theoretical events can detach partially during a run prior to full detachment (e.g., when two motors are motile at single-kinesin super-stall forces and one motor detaches the assembly can still remain bound and be counted as part of the single-motor distribution while at super-stall forces), while experimentally, such events are not and cannot be included in detachment distributions. In general, the experimental analyses presented in Chapter 3 only count events that produce forward motion. In experimental data two-kinesin data at super-stall forces are binned as two-kinesins only when forward motion

is produced, any segments of pauses in motion or rearward motion in these traces cannot be reliably attributed to any particular motor-assembly population and are therefore not counted. These differences account for the lower proportion of two-motor detachments events at super-stall forces observed experimentally (compare Figure 3.12 and Figure 4.3a), as well as the correspondingly smaller experimental two-kinesin population fractions above super-stall forces (compare Figure 3.18 and Figure 4.3b).

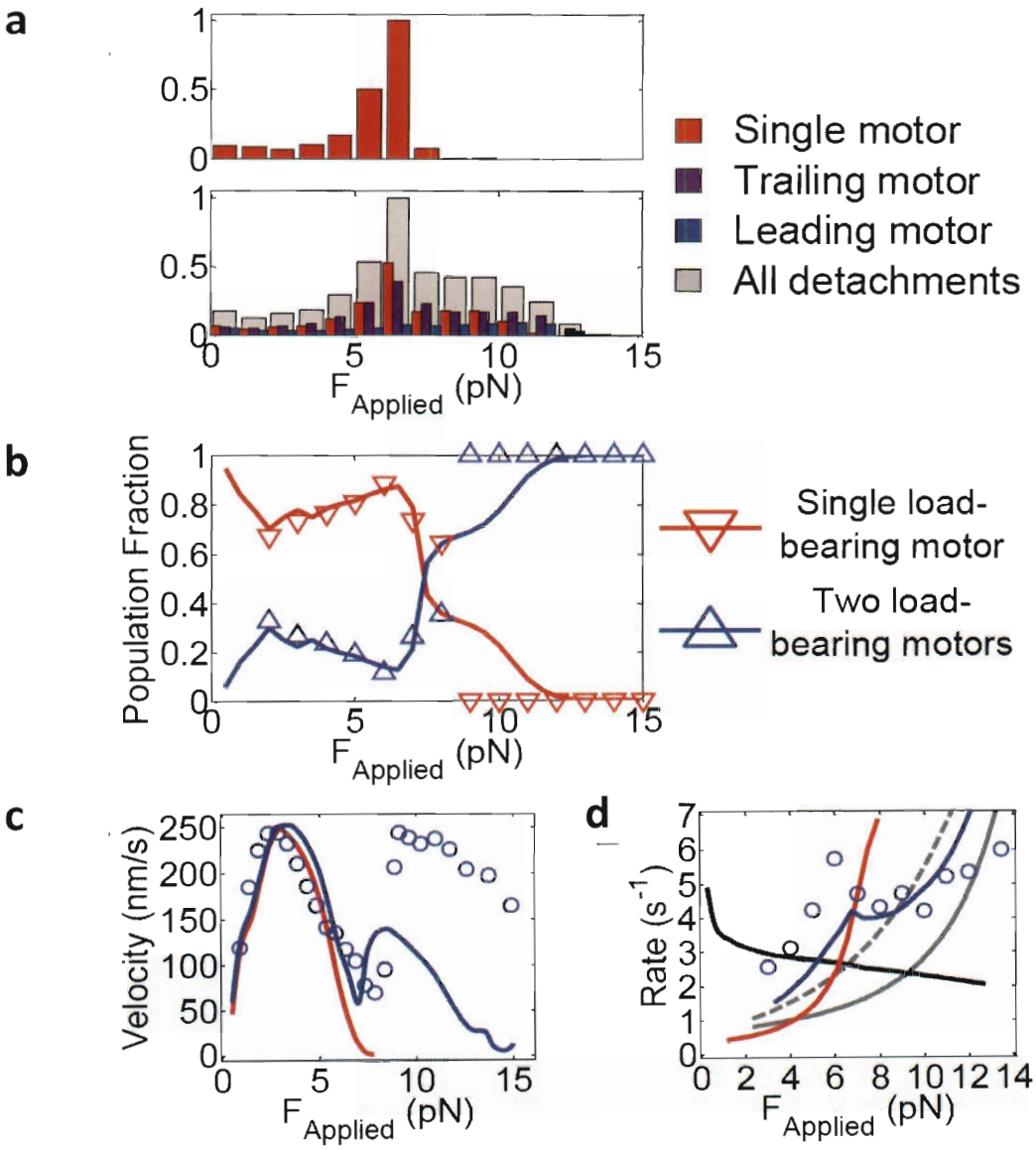

Figure 4.3: Predicting Two-Kinesin Behaviors in an Optical Trap

(a) Simulated histograms describing the force-dependent detachment distributions for two-kinesin complexes. Histograms of events originating from the detachment of motors in single-motor-bound microstates (red), as well as detachment of the trailing (purple) and leading (blue) motors in two-motor-bound microstates are superimposed on a cumulative histogram of all events (grey). (b) Simulation of single load-bearing motor population fraction (red line) with data (downward-triangles) and two load-bearing motors population fraction (blue line) with data (upward triangles) as a function of applied load in the static trap. In simulations, the load-bearing population is calculated as the fraction of beads at a given force that are driven by two microtubule-bound motors each bearing at least 35% of the applied load. The non-load-bearing population fraction consists of both single-motor-bound bead populations and two-motor-bound populations that do not meet the load-sharing criterion. (c) Average bead velocities as a function of applied load for the single-kinesin (red line) and two-kinesin (blue line) simulations. Experimentally-measured two-kinesin complex velocities (blue circles; Figure 3.14) are given for comparison. (d) Average motor binding/detachment rates. Simulated transition rates describing motor binding ($k_{on[1\rightarrow 2]}$, black line) and detachment ($k_{off[1\rightarrow 0]}$, red line; $k_{off[2\rightarrow 1]}$, blue line) are shown, as well as lines that correspond to the expected detachment rates under equal load sharing for the two-state fit (solid grey) and two-state steady-state (dashed grey). Experimentally-measured values for $k_{off[2\rightarrow 1]}$ (blue circles, Figure 3.36) are given for comparison.

The amount of time cargos are driven by one motor or two load-bearing motors determine how effectively two motors will cooperate. In the simulations bead transport starts with the binding of a single motor molecule, followed potentially by the second motor. The probability that the motor system will adopt microstates with a single load-bearing motor decreases abruptly until the applied load reaches 2 pN (as seen in Figure 4.3b); our experimental analyses cannot be performed in this force regime due to the limitations of creating compliance-correction factors at low forces where motors are extremely compliant (see Figure 3.33). However, matching experimental observations, the probability that the system will adopt a single-load-bearing motor microstate increases between applied loads of 2 and 7 pN, and at larger forces the single-motor states abruptly drop. This indicates that two-kinesin complexes do not adapt well to increasing loads in the intermediate force regime, in so far as they do not occupy load-sharing microstates where motors are bound close together on the microtubule.

Similar agreement between experiment and theory is found in analyses of average bead velocities and two-kinesin detachment rates at low applied loads, providing additional verification that the model captures the extent of load sharing in this region (Figure 4.3c). Average cargo velocities follow the single-kinesin F-V relationship closely up to 7 pN, after which, there is a dramatic increase in bead velocity; note that some of the curvature in these plots stems from the stretching of motors during bead displacements as the load increases, especially at low applied loads (< 5 pN). Furthermore, as in static trapping experiments, the transition rate describing the

partial detachment of a complex, $k_{off[2\rightarrow1]}(F_{ap})$, is found to increase non-monotonically with load, producing a peak near the peak detachment force of the two-motor complex (Figure 4.3d). In the vicinity of this peak, experimental detachment rates are significantly higher than the predicted trends for two motors assuming equal load sharing and the highest possible (steady-state) detachment rates for individual motors: $k_{off[2\rightarrow1]}(F_{ap}) = 2*k_{off[1\rightarrow0]}(F_{ap}/2)$ (the grey dashed curve). Such rates therefore provide strong evidence against load sharing, and further support the notion that cargo transport by a two-kinesin complex in a static optical trap is primarily driven by a single motor at a time, especially when the load is smaller than kinesin's stalling force.

Despite the agreement at low applied loads, there are still some significant differences between the experimental measurements and current model predictions. Most noticeably, measured two-kinesin velocities are appreciably higher than their calculated values above 7 pN (Figure 4.3c). The previous analyses of bead displacement sizes indicated that motors may coordinate/synchronize their stepping mechanics at large applied loads (see Figure 3.35), and this behavior is not incorporated into the present model. One would expect that such positive (synergistic) cooperation would depend on the separation distance between motors on the microtubule and significant load-sharing (e.g., if this behavior stems from specific, local inter-motor interaction). As discussed below, the model predicts that motors within the two-kinesin complexes will bind to closely-spaced microtubule lattice sites at forces beyond the stall force of a single kinesin, which could support the type of cooperation that may be occurring in

experiments. Still, the current model's framework could be used to explore these effects.

We also examined how multiple-kinesin dynamics is influenced by the positions of the motors on the cargo (bead) and the presence of a third motor molecule. In both cases, cargo-microtubule detachment force distributions and velocities are found to follow the same trends predicted for the two-kinesin complexes (Figure 4.4). This implies that the deviations between predicted and measured two-kinesin velocities at high forces cannot be simply explained by variability in the structure of multi-motor complexes or the presence of a third motor. Of note, calculated three-kinesin velocities are only slightly higher than those produced in two-kinesin simulations between 7 and 12 pN (as shown in Figure 4.4b). Given this result, it should not be anticipated that any potential coordination between locally-grouped motors leading to the high cargo velocities at high loads (7-14 pN) will result in a significant difference between two- and three-kinesin velocities within this force regime since, to contribute to cargo motion, the third kinesin would face the even more formidable challenge of gaining distance on two synergistically-coupled motor partners.

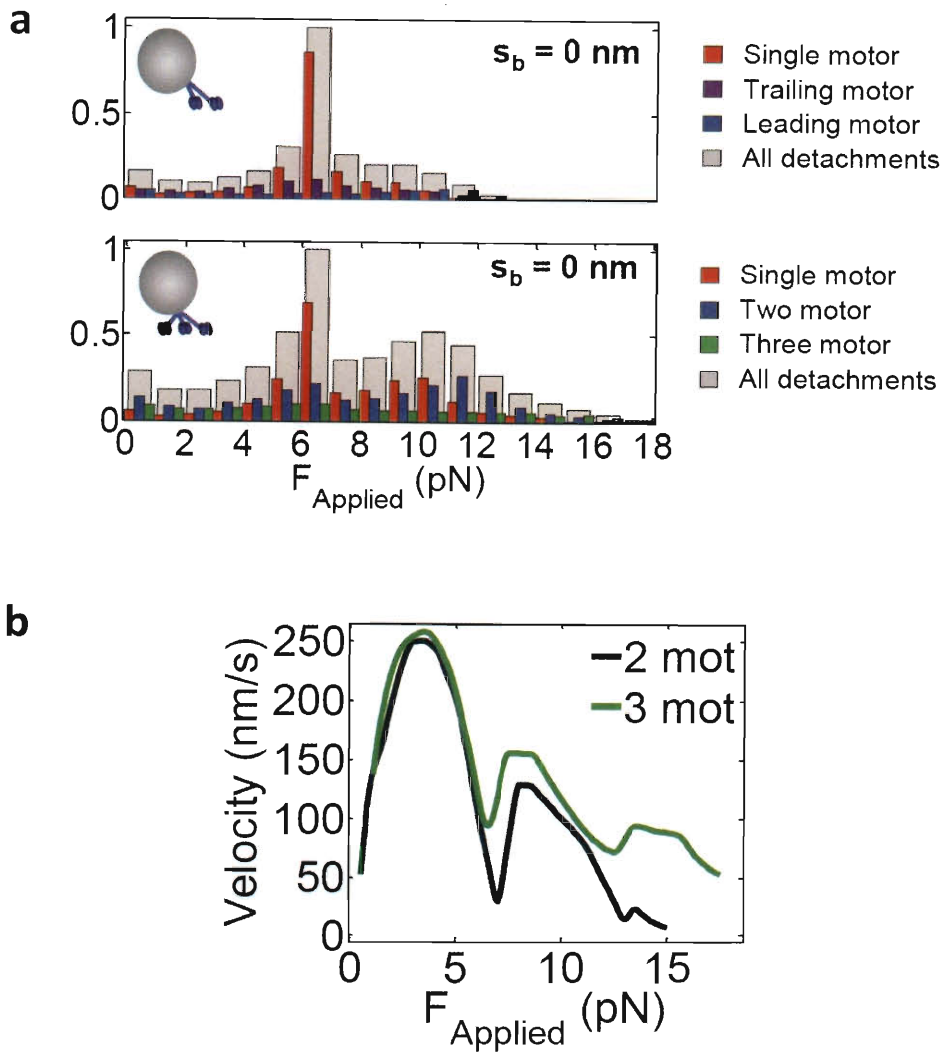

Figure 4.4: Kinesin Motor Cooperation is Generically Insensitive to Cargo-Bound Positions and Motor Number

(a) Detachment force distributions for two kinesins anchored to the same point on the bead surface. The three-kinesin distribution (bottom) shows that adding a third kinesin enhances the activity of the complex, but only enough to give two peaks. The tallest still is still near kinesin's stall force (~7 pN), while the minor peak is less than twice the stall force (near 10 pN). (b) Bead velocities as a function of applied load showing that motor cooperation is not enhanced appreciably by the addition of a third motor or cargo spacing. Note, the F-V behavior shows that motor groups act as effectively one motor until they experience a load that exceeds 7 pN after which addition kinesins contribute significantly to transport.

4.2.2. Evolution of Microstate Densities and their Load Rate Dependencies

The apparent inability for two kinesin motors to cooperate effectively is surprising, particularly considering the extent of the uncooperative behavior and the resultant dependences of cargo velocities and detachment rates on the applied load. However, the extent to which multiple kinesin dynamics are influenced by the non-negligible loading rate in static trapping experiments must also be addressed. To explore this, simulations that examined the dynamics of two-kinesin complexes when they transport cargos against a constant load were performed (mimicking trapping assays that employ force-feedback).

Analyses of cargo transport by two kinesins against increasing (static trap) and constant loads (force-feedback) revealed both significant similarities and differences between these two transport scenarios. In both cases, average motor-microtubule binding rates $\langle k_{on[1\rightarrow 2]}(F_{ap})\rangle$ decrease with increasing load (Figure 4.3d), illustrating how strain energy affects the microstates complexes can transition into via motor binding. The change in ΔE_{config} is large when the second motor binds to a lattice site where, after the transition, it takes on a portion of the applied load. Overall, this constraint creates a strong preference for the two-kinesin system to bind into non-load-sharing configurations where the motors are spaced far apart on the microtubule. Such behavior is reflected in microstate probability distributions describing how often a two-motor complex will occupy different two-motor-bound configurations (Figure 4.5). For both the increasing- and constant-load cases, steady-state inter-motor separation

distances are relatively large and broadly distributed at loads below kinesin's stall force. Given the widths of and similarities between these distributions, it is not surprising that much of the negative cooperative behavior observed in the static trapping experiments is also found in the constant load simulations, implying that kinesins will not necessarily cooperate more productively when loading rates are negligible.

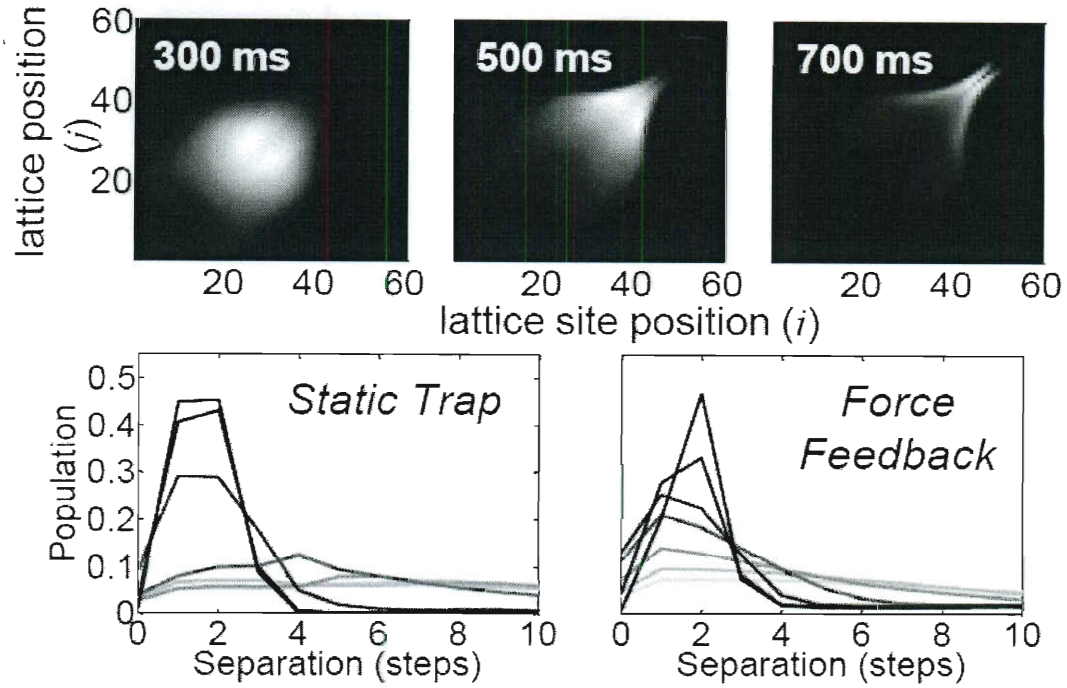

Figure 4.5: Microstate Distribution Dependence on Loading Rate for Mode A Motors

(top) 2-D plots show the probability that a two-kinesin complex will adopt specific two-motor-bound configurations at various time points when transporting cargos against the increasing load of an optical trap. Microstates are designated by the microtubule-bound positions of each motor; i and j are the lattice site positions of motor 1 and 2, respectively. Intensities along the diagonal represent microstates where motors occupy the same lattice site. (bottom) Two-kinesin microstate probabilities plotted as a function of motor-microtubule binding site separation distance assuming loads increase in time (left) or remain constant (right). Line colors indicate applied loads ranging from 1-13 pN (light to dark) in increments of 2 pN.

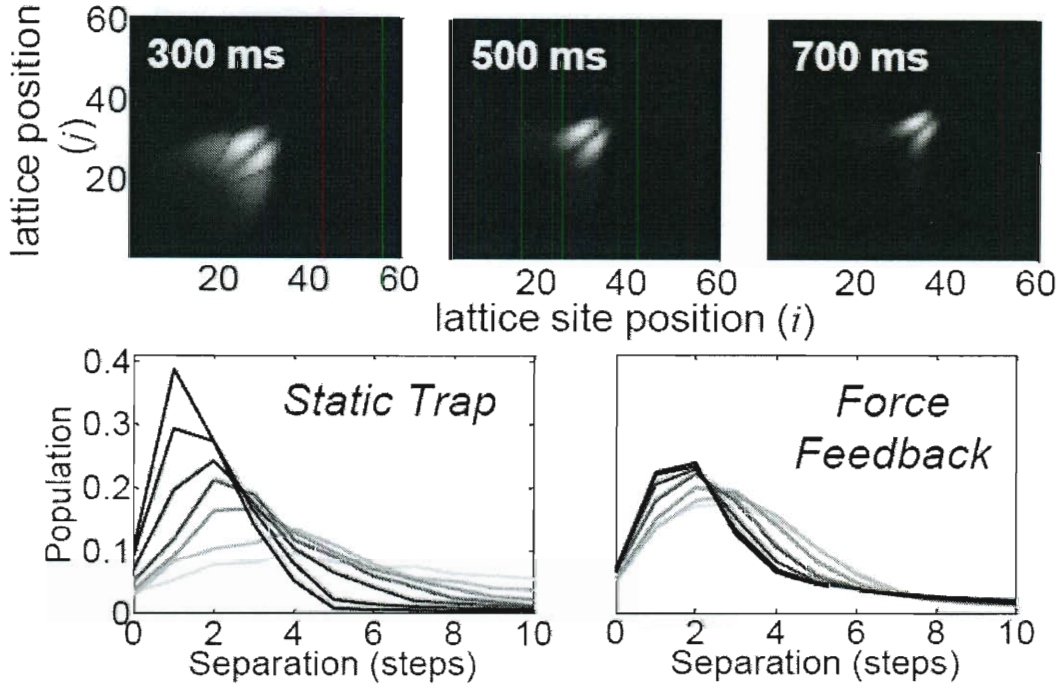

Figure 4.6 Microstate Distribution Dependence on Loading Rate for Mode B Motors

The equivalent plots as in Figure 4.5 for complexes composed of two mode B motors, except that the lines in the bottom panels are plotted for loads of 1-7 pN in increments of 1 pN.

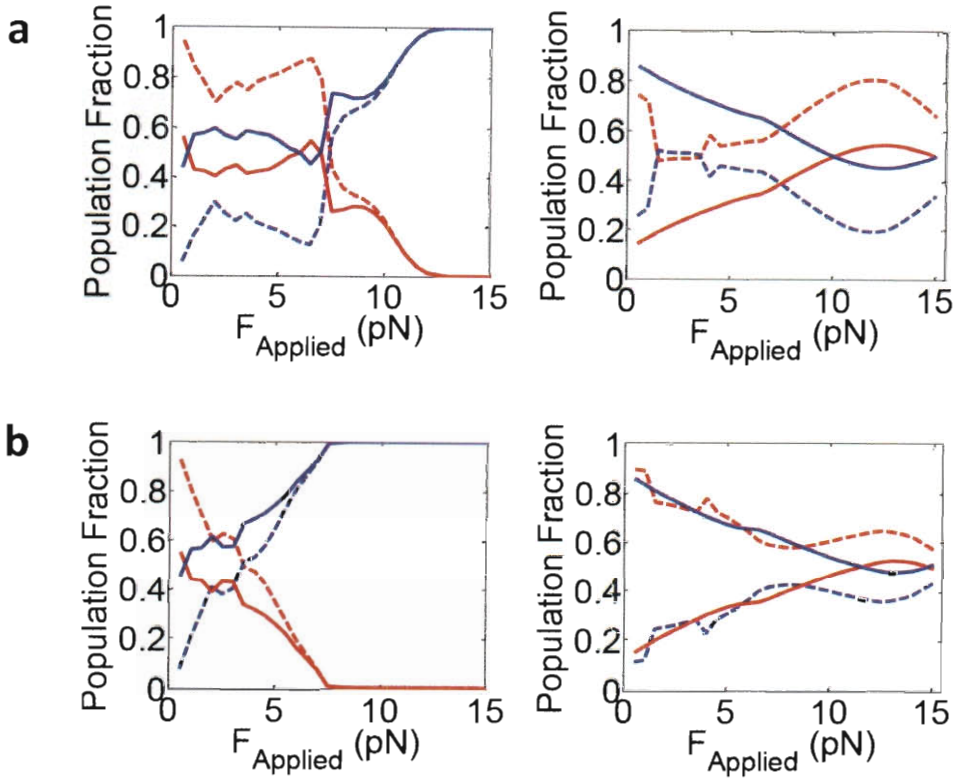

Figure 4.7: Two-Motor Bound and Load-Sharing Fractions as a Function of Applied Load

In each plot single (red solid lines) and two-motor-bound microstate populations are plotted (blue solid lines), as well as the non-load-sharing (red dotted lines) and load-sharing (blue dotted lines) microstate populations (where "load sharing" means that both motors carry at least 35% of the total load. Results for stepping modes A (a) and B (b), respectively, are shown for both increasing loads (left) and constant loads (right).

The distributions of motor separation distances when both kinesins are filament-bound differ significantly for the static trap and force-feedback simulations. In general, the constant-load distributions are more narrowly distributed at nearly all applied forces (Figure 4.5). Furthermore, substantial differences are found between the relative probabilities motor complexes occupy single-load-bearing motor microstates for each case (Figure 4.3b and Figure 4.7).

In contrast to increasing-load (static trap) behaviors, single-motor population fractions in constant load simulations are much lower in the absence of an applied load and rise steadily over the range of 0-12 pN. It is likely that this difference is so pronounced since detachment events in a static trap result in rearward displacements of the bead. When one motor in a two-motor-bound complex detaches in the static trap, the trap pulls the bead backward to a new, lower force with only one motor bound, which raises the average number of bound motors at high forces and lowers it at low forces. This does not occur when applied loads remain constant.

4.2.3. Motor Mechanochemistry Tunes Collective Motor Function

To assess how the stepping behaviors of processive molecular motors influence their collective dynamics, the above simulations were also performed for complexes composed of less efficient motors that advance via stepping mode B (Figure 4.1b and Figure 4.2a). Here, mechanical (elastic) properties and zero-load stepping rates correspond to those determined from single kinesin-1 assays. However, since mode B

motors move much slower against applied loads detachments are assumed to follow the steady-state curve (negligible load-rate) in Figure 4.2c.

Despite the assumption of increased motor-microtubule detachment rates, the alteration in stepping mechanism introduced in mode B results in more effective multiple-motor cooperation than is observed with kinesins (Figure 4.6 and Figure 4.8). Microstate probabilities for static trap loading conditions are much more narrowly distributed and configurations that should support load sharing are much more prevalent, even at early time points in simulations. Similar behavior is produced in constant load simulations. Motor-microtubule binding rates still decrease with increasing force in both cases. However, the curve describing average motor-filament detachment rates ($<k_{off[2\rightarrow1]}(F_{ap})>$) does not contain a peak, and simply increases monotonically and follows the equal-load-sharing trend much more closely (Figure 4.8). In turn, such behavior results in stronger dependence of cargo detachment forces and the average velocities on motor number (Figure 4.9).

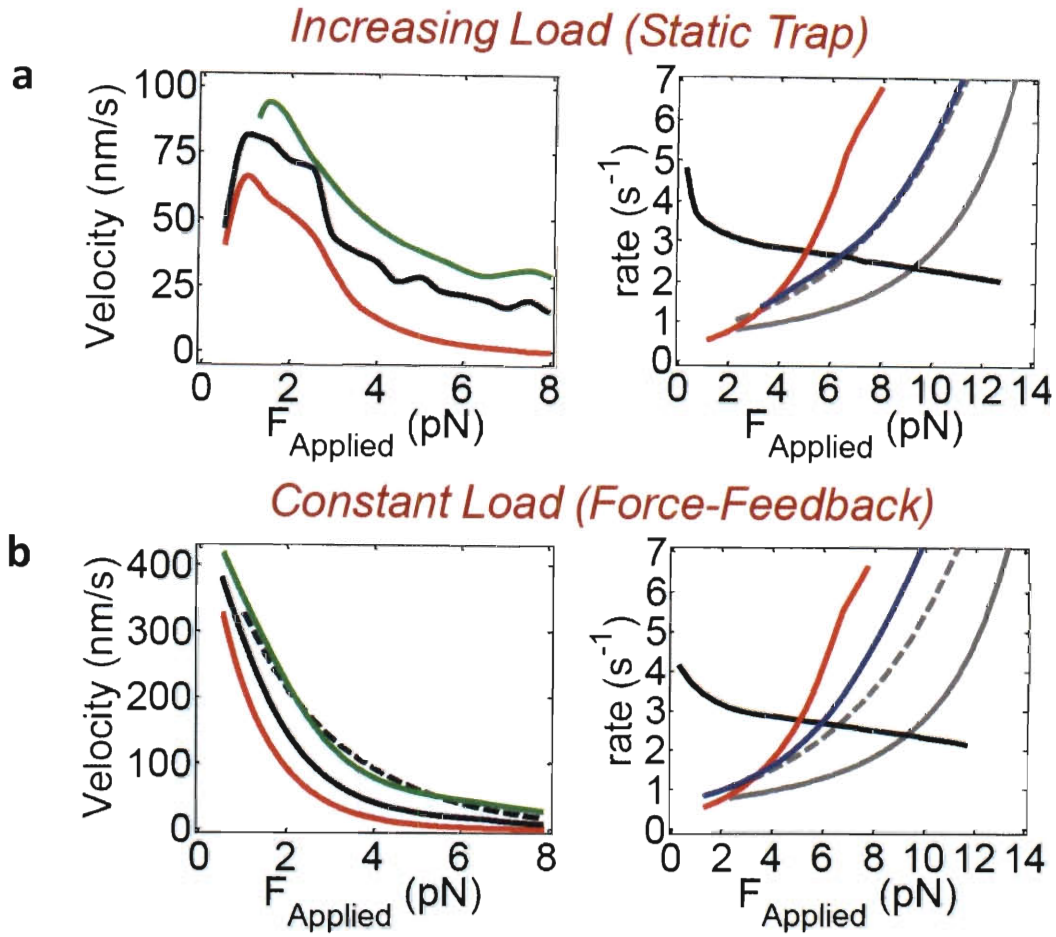

Figure 4.8: More Productive Cooperation Occurs Among Inefficient (Mode B) Processive Motors

(a and b) F-V curves and average motor binding detachment rates calculated assuming cargos are transported against increasing (a) or constant (b) applied loads. Line colors in the F-V plots (left panels) correspond to a single motor (red), two motors with a cargo-separation s_b=0 nm (black), and three motors with s_b =0 (green). Rate plots (right panels) describe motor binding ($k_{on[1\rightarrow 2]}$, black line) and detachment ($k_{off[1\rightarrow 0]}$, red line, and $k_{off[2\rightarrow 1]}$, blue line). The grey lines in the detachment rate plots correspond to the expected rates under equal load-sharing for the 2-state fit (solid) and 2-state steady state (dashed).

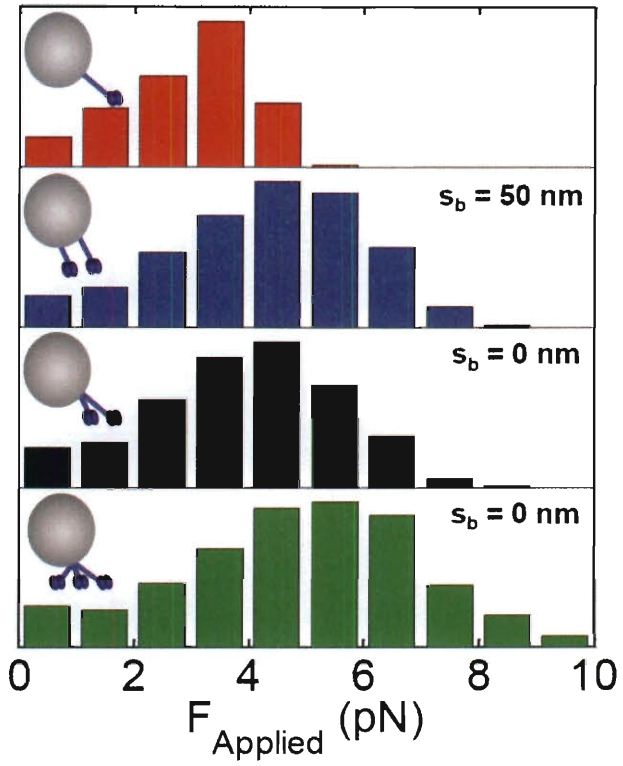

Figure 4.9: Detachment Force Distribution Histograms for Stepping Mode B Motors

The total stepping mode B motor number and on-bead motor separation distance (s_b) is shown in each panel.

cooperate), but surprisingly, less efficient motors such as dynein are also predicted to produce more cooperate behaviors. This is primarily the result of the motor's velocity dependence under load which dictates that inefficient motors have greater potential to crowd together on a microtubule and can thereby share applied loads more readily. This study also highlights that the force and velocity that can be produced by a multi-motor assemblies is dependent on the loading rates experienced, and these effects are further described in Chapter 5.

Chapter 5

Constant-Load Studies Reveal that Cargos Driven by Multiple Motors Respond to Force History

The optical trapping studies presented in Chapter 3 were performed in a 'static' trapping mode where the trapping laser remains stationary throughout experimentation. In this mode, motor molecules that pull against the optical load of the trap experience an increasing rearward force – as if they were tethered by a spring to a stationary object. Static trapping is therefore well-suited to probe a range of load-dependent motor protein behaviors; with each step a motor protein or motor assembly experiences a new higher load. Analyses of these experiments can provide a convenient means of quickly surveying single-molecule behaviors. However, by virtue of the optical trap's distance-dependent loading profile, measurements on biomolecules of interest are inherently under non-steady state conditions that can affect outcomes and

The enhanced load sharing ability of mode B motors indicates that a high sensitivity of forward stepping rates to increasing load, while generally reducing the efficiency of individual motors under load, actually assists in multiple-motor cooperation. This effect largely stems from the rate at which inter-motor distances close being greater than the rate at which cargos advance against an increasing load. To explore this phenomenon, the temporal evolution of average cargo velocities under constant load after microstate distributions were allowed to reach their steady-state at one force and then were subjected to an instantaneous increase of 1 pN in the applied load were examined. After this jump, cargo velocities 'relaxed' to their steady-state levels at the increased load in an approximately exponential manner that could be fit to yield an exponential time constant. Although the absolute relaxation time constants (Figure 4.10a, left) are larger for stepping mode B than for mode A, they are shorter when normalized by the average time that it takes the cargo to advance forward a distance of 8.2 nm (Figure 4.10a, right). This means that when teams of motors with mode B stepping mechanics work against varying loads, they will be more capable of optimizing their inter-motor separation distances before the load changes and defines a new optimum configuration. Moreover, the normalized relaxation time constants decrease monotonically for mode B motors, while mode A motors display a peak at 8 pN, which is close to the force where the largest discrepancy between the steady-state and static trap distributions is found. This result strongly suggests that motors that advance via mode A (kinesin-1) are frustrated kinetically from assuming microtubule-

bound configurations where they share their applied load and that such behavior hampers the function of the two-motor complex significantly

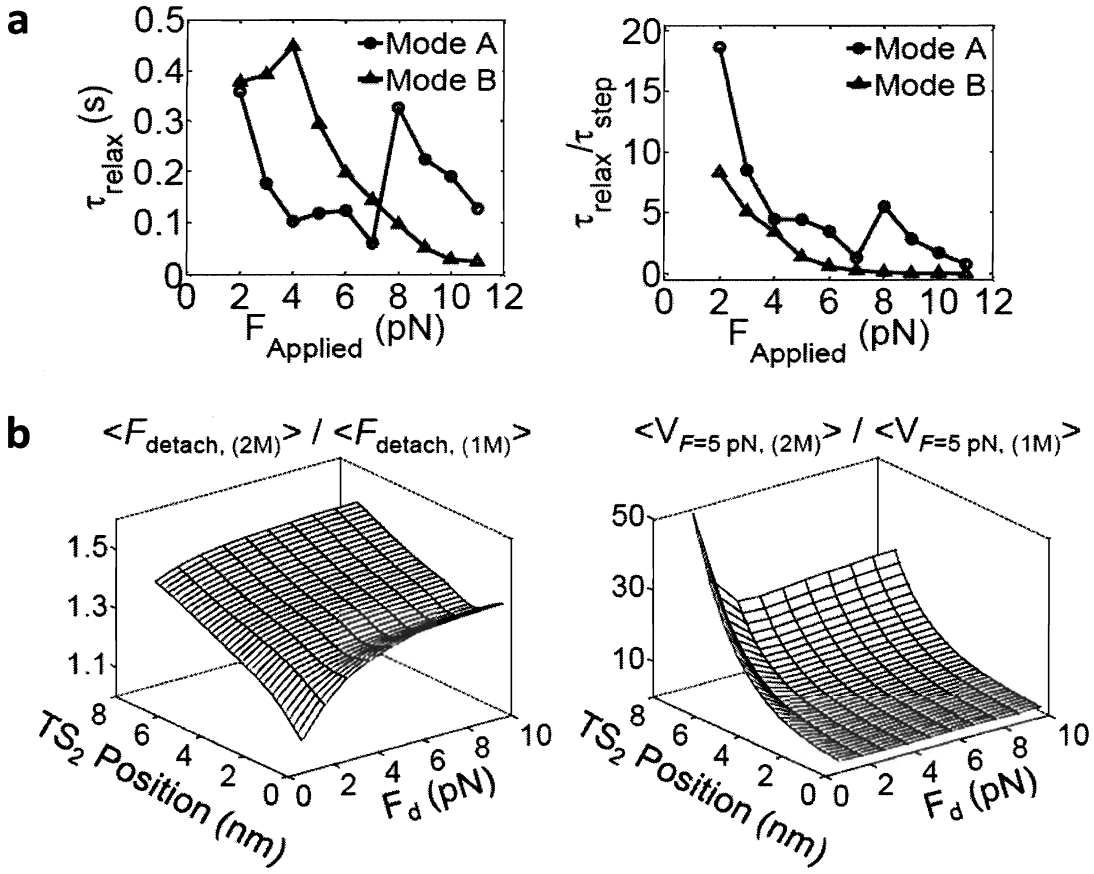

Figure 4.10: Two-Motor Transport Performance Depends on Motor Stepping Efficiencies and Microtubule Affinities

(a) Relaxation time constant of a two-motor system in both stepping mode A and B (left), and the same values normalized by the stepping time constant (right). (b) Average detachment force of a two-motor system in a static trap, normalized by that of a single motor (left). A value of 2 indicates maximally (additive) cooperative behavior. Velocity of a two-motor system at constant load (F_{ap} = 5 pN), normalized by that of a single motor (right).

To further survey how multiple-motor cooperativity depends on the properties of a processive motor's stepping and detachment reaction coordinate, the dependence of average two-motor detachment forces and cargo velocities on the position of TS_2 along a motor's stepping coordinate (which tunes motor stepping efficiency against an applied load), and its critical detachment force (F_d), which, as defined in the single-state Kramer's model, tunes a motor's microtubule-bound lifetime (Figure 4.10b) was determined. To facilitate comparison between motor types, two-motor detachment forces and cargo velocities (at a constant load of 5 pN) have been normalized by the average detachment forces/velocities of their single-motor counterparts. Plots of these values both show that the weakest cooperative behavior ($F_{peak(2)}/F_{peak(1)} = 1$; $V_2/V_1 = 1.0$) occurs when the stepping and detachment reaction coordinates approximate those expected for kinesin-1; the corner of the plot near the origin. As the mode B motor simulations suggest, there is a persistent increase in detachment/velocity enhancements over single motors as motors become less efficient (as the location of TS_2 moves away from the initial motor position on the stepping coordinate). Also, not surprisingly, motors that remain attached to the microtubule more tenaciously (large F_d) also cooperate more effectively. Thus, both of these characteristics should allow motor teams to share the applied load more equitably because in order to do so, a trailing motor must catch its leading partner before either detaches. However, what is striking is that the stepping mechanics of a single motor is equally and potentially even more important than its detachment behavior in determining collective motor function.

4.2.4. Extension of Theoretical Modeling to Three Dimensions

For all simulations described above, motor trajectories are constrained to a single microtubule protofilament, and volume exclusion effects that would otherwise prevent motors from binding the same microtubule lattice sites are neglected. These choices were made because they simplify the model's master equations significantly. These assumptions are considered to be appropriate because most significant two-motor geometries are nearly two-dimensional (planar) when solved in three dimensions. Furthermore, the results above did not change significantly when a 3-dimensional form of the model was tested (incorporating three different parallel microtubule protofilaments) where the motors could occupy explicitly enumerated sites on neighboring protofilaments that produce side-by-side motor-bound geometries.

4.3. The Implications of the Discrete-Microstate Model of Multiple Motors

In this study, a theoretical framework was developed that allows the collective dynamics of multiple-motor complexes to be parameterized using fits to single-motor optical trapping data. Differences between configuration-dependent strain energies of the complexes can be calculated and used to specify transition rates that determine how rapidly a complex's filament-bound geometry evolves in the presence of an applied load.

While the deviations from measured multiple-kinesin velocities at loads exceeding kinesin's stall force suggest motor coordination must be considered to describe multiple kinesin dynamics at high loads, model predictions support the idea that geometric and kinetic constraints largely limit how effectively a group of kinesins can cooperate as a team. Overall, multiple-kinesin complexes have difficulties adopting microtubule-bound configurations that support load sharing whether loads increase in time or remain constant. Also, in general, the present theoretical results highlight that there are load-rate dependencies that affect cargos transported by teams of processive motors, and that the time it takes for a motor complex's microtubule-bound geometry to evolve in response to a load plays a critical role in determining the forces and velocities produced by the system (this will be discussed further in Chapter 5).

One might expect that a group of fast and efficient motors like kinesin would be able to cooperate effectively when transporting cargos since they should be able to adjust their bound geometry rapidly via motor stepping. However, this study shows that less efficient processive motors are much more capable of cooperating effectively. Even though the absolute relaxation times of such motor systems are longer than those calculated for multiple kinesins given the same load conditions these systems possess microstate distributions at steady state that lead to better load sharing behaviors. Less efficient motors also have more time to adjust their bound geometry, and hence, can develop load-sharing configurations more readily.

The differences between the collective motor behaviors described above may have important implications for mechanisms that regulate cargo motion. First, motor stepping efficiencies may play a role in bidirectional transport, where oppositely-directed teams of kinesin and dynein compete antagonistically to drive cargo motion. In this case, the direction and the magnitude of the applied load will change in time as the number of motors competing against one another also changes. Furthermore, several reports suggest that dynein stalls at significantly lower forces than kinesin (Ori-McKenney, 2010; Soppina, 2009). This inefficiency is consistent with observations that dynein's stepping patterns are much more irregular than kinesin's; backwards stepping influences dynein's average F-V stepping. Thus, although more dyneins will be required to produce the forces of a single kinesin, a team of dyneins with an inefficient stepping mechanism should be able to compete with an otherwise stronger kinesin team given

their greater ability to cooperate effectively. With this behavior, the number of dyneins, but not kinesins, would serve as a regulator of bidirectional transport. To date, the mechanochemistry of the motor protein dynein has not been characterized as well as kinesin's; consequently, confirming such ideas requires further investigation.

Summary of Chapter 4

The key features of multiple-kinesin transport can be described by a newly developed discrete-microstate model for multiple motors in two dimensions. In this model, transition rates between discrete assembly microstates (motor-motor-microtubule configurations and motor sub-steps) are dependent on the difference between configurational energies which are parameterized by the measurements of single-kinesin mechanical compliance, stepping rate dependence under load, and detachment kinetics described in Chapter 3. The model recapitulates several observables from measurements of single- and two-kinesin force detachment distributions as well as their velocity-dependence under load and has also been extended to three motors showing again that kinesin motors do not readily cooperate to work against applied loads. Also, because a critical component of the theoretical framework is the modeling of sub stepping rates, the efficiency (and therefore stepping-rate dependence under load) of the modeled motors can be tuned by moving the position of sub-step transition states within the stepping reaction coordinate. In this way, the collective dynamics of other motor types (e.g., dynein) can also be predicted. Interestingly, the ability of motors to cooperate is found to be dependent on the efficiency of a motor's stepping mechanism. As expected, motors with greater affinity for microtubules are predicted to cooperate to a greater extent (motors stay bound to the microtubule for longer periods of time and therefore have more potential to

interpretations of their properties. For instance, motor-microtubule detachment rates are known to decrease with increasing loading rate, as is generally the case for ligand-receptor affinities measured out of equilibrium. This behavior is clearly observed in detachment rate measurements of single-kinesins assemblies (see Figure 5.1).

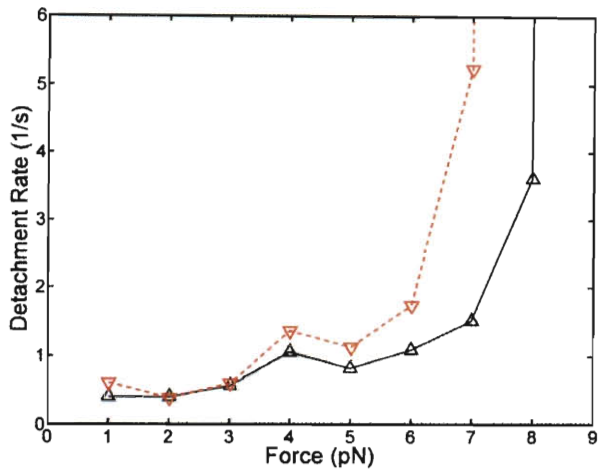

Figure 5.1: Measurements of Motor-Microtubule Force-Dependent Detachment Rates are Affected by Loading Rate

Detachment rates are given as a function of force for single kinesins as measured in a static optical trap at a trap stiffness of 0.05 pN/nm (red, downward triangles, dashed line) and 0.07 pN/nm (black, upward triangles, solid line). Motors probed at larger trap stiffnesses (and therefore larger loading rate) exhibit greater affinity (lower detachment rates) for microtubules.

The loading rate-dependent effects of static optical traps can be mitigated somewhat by reducing the trap stiffness and thereby allowing motors greater freedom of movement under a decreased loading rate. However, by virtue of its fundamental principles a static optical trap cannot be used to impose constant loads and the practical extent to which trap stiffnesses can be lowered is slight. The force profile of an optical trap is nonlinear (see Figure 2.4) and has a maximum - a distance beyond which force caused by the trap begins to decay rather than linearly increasing and producing loads as a Hookeian spring (see Section 1.4). Therefore, in order to apply forces of relevant magnitudes to motor proteins there is a minimum trap stiffness that can be used. Furthermore, although the trapping force is strongly dependent on the size of the target being trapped, the temporal resolution of back-focal-plane position detection offered by microspheres is significantly reduced with larger targets. As a result, a static optical trap used to trap 0.5 μm diameter microspheres in these studies must be performed at a stiffness of at least ~0.01 pN/nm in order to apply forces on the scale of the single-kinesin stall-force. Still, stiffnesses of this magnitude translate to a loading rate of ~0.1 pN/step, which may still be significant to motor function, hence another means of producing constant load must be applied to probe the steady-state behaviors of motor proteins.

As a consequence of motor protein's potential sensitivity to loading rate, it is critical that the activities of motors and motor assemblies be examined under constant loads that can reveal the equilibrium behaviors of motors. An optical trap operating in

force-feedback mode has the ability to apply constant loads; steady loads are achieved through the use of software-based feedback routines that update the position of a steerable laser to maintain a constant trailing distance between motor assemblies and the trap and therefore a constant force (see Chapter 2 and Figure 5.2). However, the software routines that enable controllable steering of the trapping laser also allow more elaborate force profiles (sequences, magnitudes and durations of forces) to be applied and utilized to gain deeper mechanistic understanding of collective motor behaviors than can be garnered from static or feedback studies alone.

Beyond providing a means to probe the steady-state behaviors of motors and motor assemblies the application of constant loads is motivated by cellular environments where viscous loads may generate the dominant forces applied to biological cargos. Since viscous loads scale proportionally with velocity a motor or group of multiple-motors operating under a steady-state behavior might move along microtubules at a relatively constant velocity and as a result experience a constant viscous load. Yet, motors can also experience time- and directionally-variant forces as diverse as the number of intracellular processes to which motors collectively contribute and under as many unique situations as there are distinct assortments of motor number and type. The variety in force regimes experienced by the motor machinery of cells combined with difficulties in characterizing the properties that define motor groups has made previous measurement of collective responses to changing loading conditions unapproachable. However, through the use of the engineered two-kinesin assemblies

(see Section 3.2) and automated optical trap (see Chapter 2) employed here steady-state and dynamic behaviors of motor groups under changing loading conditions have been uncovered and can be used to inform interpretations of complex intracellular transport processes.

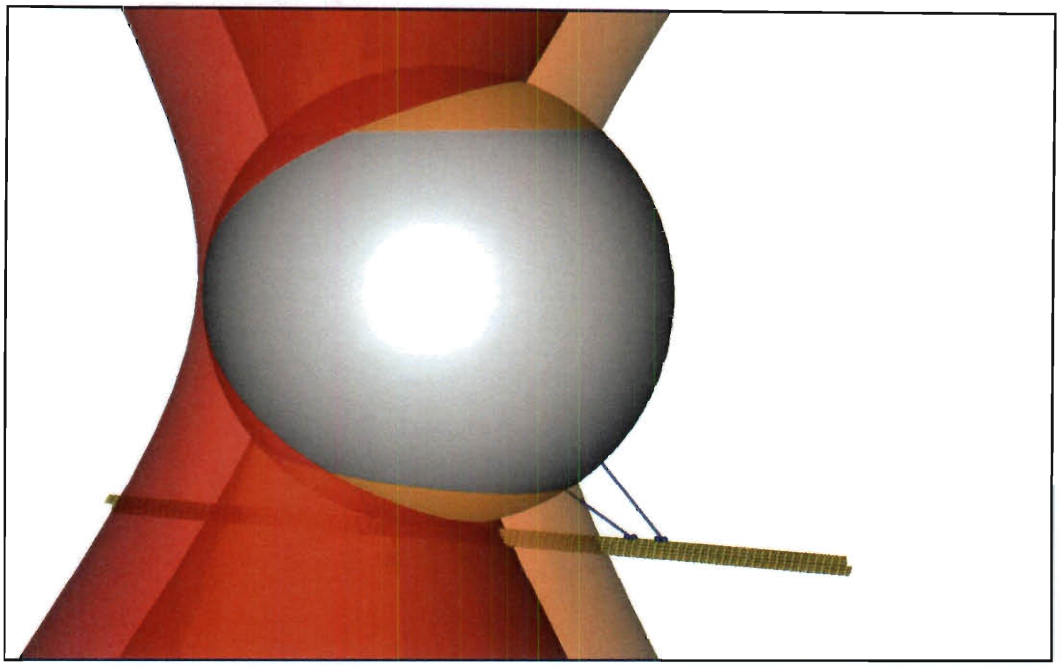

Figure 5.2: A Scaled Representation of a Two-Kinesin Assembly Pulling a Polystyrene Bead Along a Microtubule in a Force-Feedback Optical Trapping Assay

The 1064 nm steerable optical trap is represented in red and the stationary 832 nm detection laser operating as part of a back focal plane detection system is shown in orange.

5.1. Force-Velocity Responses of Two-Kinesin Assemblies under Constant Loads Reveal Cooperative and Configuration-Dependent Behaviors

The responses of two-kinesin assemblies to imposed constant loads were examined through the use of an optical trap operating in force-feedback (force clamp) mode (Figure 5.4). Trapping assays were conducted with bead preparations that yielded less than 30% motile fractions, as in prior studies (see Section 3.3), to ensure that measurements of either one or two motors were achieved in single-kinesin and two-kinesin assays, respectively (see Section 3.3.1). The same kinesin-1 complexes (K560-eGFP-Z_E) with artificial protein linker molecules, Z_R-$(ELS)_6$-ssDNA, and DNA scaffold (50 nm in length) were used as in the assays presented in Chapter 3. Measurements of the single-kinesin force-velocity relationship yielded a near-identical force response as earlier measurement utilizing a static trap (see Figure 3.17 for the F-V measurement from static trapping assays), and also a similar response as was measured in other feedback assays of kinesin motors purified from squid optic lobe (Figure 1.4).

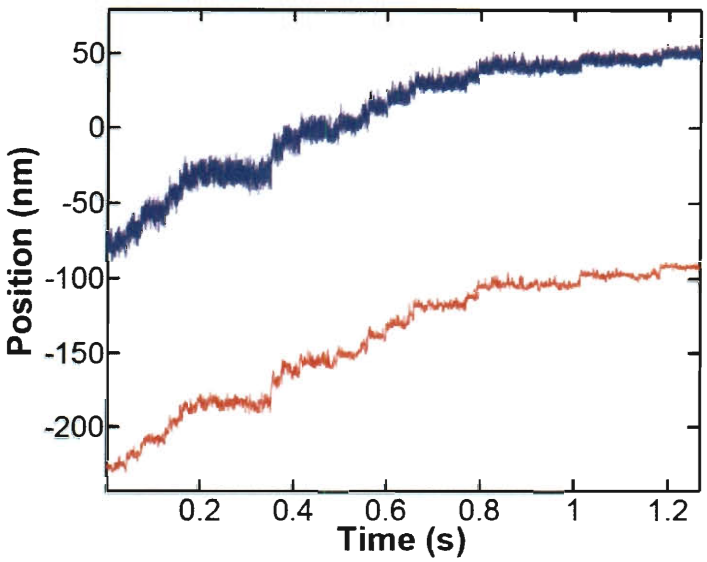

Figure 5.3: Operation of an Optical Trap in Force-Feedback (Force Clamp) Mode

Representative data for a single-kinesin pulling against a constant load induced by an optical trap in force-feedback mode. The position of the motor-transported bead is given in blue and the position of the optical trap steered through calibrated two-axis AODs is given in red. Two-kinesin assemblies were measured in the force clamp by first allowing them to bind microtubules and pull against the static trap until they produce a force of 2 pN (typically about 30 nm of travel with a trap stiffness of ~0.06 pN/nm), at which point the optical trap would be displaced backward and follow bead motions to produce the desired constant load. The position of the optical trap was updated at 200 Hz throughout force-feedback experimentation. Data was acquired and saved at a rate of 30 kHz after low-pass filtering at 10 kHz.

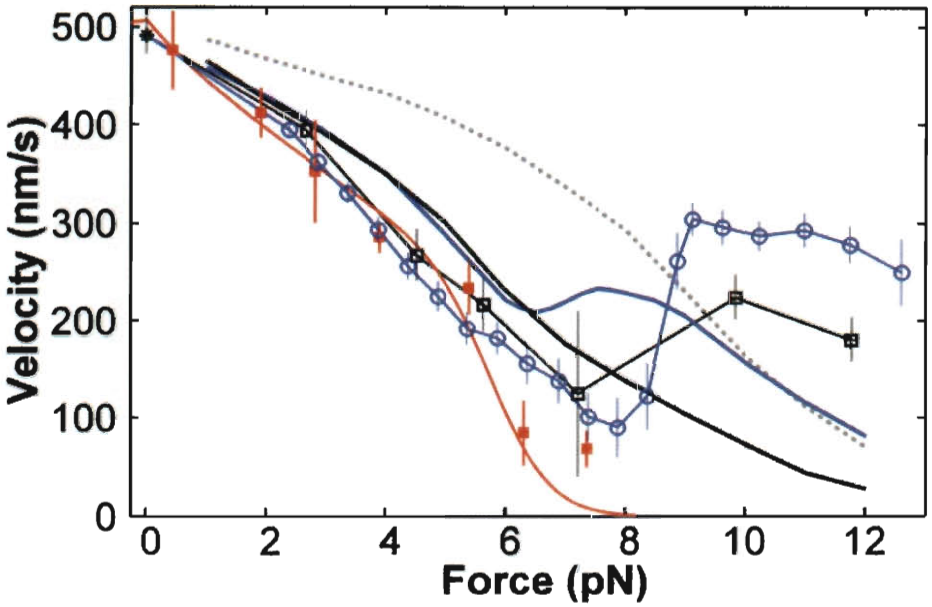

Figure 5.4: Force-Velocity Relationships of Single- and Two-Kinesin Assemblies Against Increasing and Constant Loads

Here, measurements performed under increasing loads (static trap) are represented by circles and those measured under constant loads (force clamp) are marked with squares. Single-kinesin F-V responses measured under constant load are given by the red squares. Two-kinesin F-V trends for increasing loads (blue circles) and constant loads (black squares) are also pictured. Single- and two-kinesin assemblies had to produce a force of 2 pN before feedback routines would engage. The single-kinesin data is fit by the modeling procedure described in Section 4.1.3 to produce a trend line and also serves as a basis for calculations of two-kinesin behaviors using the model described in Chapter 4. The theoretical two-kinesin F-V calculations are also presented for the increasing load (blue solid line) and constant load (black solid line) cases. The constant load case was calculated to match the experimental force clamp conditions by using the microtubule-bound configurational distribution for 2 pN in a static trap as the initial motor distribution for force clamp calculations. The grey dotted line represents the initial two-kinesin velocities the theory predicts for assemblies that have the microtubule-bound configuration expected at 12 pN in a static optical trap (see Figure 4.5); this curve serves as an upper-bound for the velocities the model predicts two-kinesins can produce. The zero velocity data point is from previous fluorescence-tracking experiments using engineered two-kinesin assemblies (Rogers, 2009). All velocity data points are given as the time-weighted mean ± s.e.m.

Comparisons of the force-velocity relationships presented in Figure 5.4 yield insight into single- and two-kinesin assembly dynamics. First, single-kinesin and two-kinesin assemblies demonstrate nearly identical force-velocity behaviors (within the limits of experimental uncertainty) up to ~5 pN whether measured under increasing loads or constant loads. Somewhat surprisingly, the correspondence between these two data sets indicates that the loading rate experienced by two-kinesin assemblies in static trapping studies (at an average trapping stiffness of 0.076 pN/nm, or ~0.5 pN/step) has little effect on measured motor velocities (i.e., kinesin's forward stepping rate is not significantly sensitive to a loading rate of ½ pN per step as compared to the zero-loading-rate case). This is true for single kinesins as well, there is no significant difference between single-kinesin F-V data acquired against increasing or constant loads (compare Figure 3.17 and Figure 5.4, red data). However, both the static and force clamp theoretical calculations (blue and black solid lines in Figure 5.4) predict somewhat higher velocities than what was produced by both experimental cases (50-100 nm/s higher across the sub-stall force range). The theory predicts velocities (motor stepping rates) based primarily on the distribution of microtubule-bound configurations of two-kinesin assemblies under specified loads. The overall lower experimental velocities indicate that the theory might somewhat overestimate the probability of two-motor configurations that allow load-sharing. It is possible that thermal fluctuation of the bead or other unaccounted for geometric effects in three dimensions might account for a distribution of states where two-kinesin assemblies spend a larger proportion of time in unproductive states than is currently expected. For example, the motor systems are

quite stiff along the microtubule axis, but relatively compliant perpendicular to the microtubule; thermal fluctuations of the bead will favor trailing motors binding into unproductive configurations (on parallel protofilaments) to a somewhat greater degree than the two-dimensional case.

Perhaps the most striking differences between experimental data and theoretical calculations are the deviations observed between the two at high loads (above the ~7 pN stall force of a single kinesin). The experimental data sets for both the increasing load and constant load cases measure velocities that are ~150 nm/s faster than the corresponding theoretical curves. Interestingly, the theoretical curve describing the increasing load case (blue solid line) does exhibit a sudden rise in velocities, relative to the theoretical constant load curve (black solid line), near 7 pN. This jump in velocity mimics the rise in velocities found experimentally in the increasing load data as compared to the constant load data (static trapping data is ~100 nm/s faster than force clamp data at loads >9 pN). This velocity difference observed experimentally and theoretically is the result of more favorable motor-microtubule binding configurations in the increasing load assay. In a static trapping assay two-kinesin assemblies bind to the microtubule at essentially zero load and face increasing load as they progress along a microtubule. Only assemblies that maintain configurations that are favorable for load-sharing can travel along their filament track long enough and far enough to reach large velocities (>10 pN). Whereas in the constant load assays the force clamp engages soon after assemblies produce 2 pN, near-

instantaneously applying a larger specified force (i.e., the distribution of configuration states in constant load assays is broader than during increasing load assay, making them less favorable for force-sharing and producing slower velocities on average).

Theoretical predictions of the force-velocity relationship of two-kinesin motors under constant loads capture nearly all of the experimentally observed behaviors. However, surprisingly, experimental velocities are significantly higher than theoretical values at forces >9 pN. In fact, theoretical maximum velocities (grey dashed line in Figure 5.4) that assume near equal load-sharing among the two kinesins in a multi-motor assembly still do not quite approach the high velocities observed experimentally. These observations combined point to the existence of some as of yet unidentified mechanism by which multiple motors within an assembly can enhance their stepping rate against loads in this regime (>10 pN). In static optical trapping assays, the observation of potentially significant numbers of full-size 8 nm bead displacements in histograms of step-sizes generated by two-kinesin assemblies in high-force, high-velocity states is also indicative of such a mechanism where motors may communicate (perhaps through the changing load-sharing distributions) to influence each other's stepping rates and help maintain small inter-motor microtubule-bound separation distances through synchronized stepping of both motors with an assembly (see Figure 3.35). However, synchronized or coordinated stepping and the consequent benefits of load sharing alone cannot account for the enhanced velocities experimentally observed in static and force-feedback trapping experiments at super-stall forces (Figure 3.17and

Figure 5.4). Some other mechanism must be involved in reshaping and increasing (or maintaining) kinesin's load-dependent stepping rate profile (single-kinesin force-velocity relationship) and perhaps also reducing kinesin's propensity for detachment (Figure 3.36) to produce these behaviors. As described in Section 3.6, the decoupling that occurs between ATP hydrolysis at kinesin's active heads and processive forward motion above 5 pN is a prime candidate for understanding the mechanism of these apparently supercharged high-force two-kinesin behaviors. Also, note that the theoretical detachment rates of two-motors (based on fits to experimentally measured single-kinesin detachment rates) overestimate two-kinesin experimental data (as shown in Figure 4.3d). These relatively reduced experimental detachment rates are also indicative of cooperative effects that might exist at high loads, which could also in part explain the enhanced experimental velocities (Figure 4.3c and Figure 5.4)

The velocity distributions from experimental force clamp experiments of two-kinesin assemblies (Figure 5.5) recapitulate the findings from static trapping experiments (see Figure 3.15). Below the single-kinesin stall force, velocity distributions are bimodal - corresponding to two-kinesin assemblies operating in two general classes where either one or both kinesins of an assembly carry the applied load. Above kinesin's single-motor stall force, velocity distributions are uni-modal, indicating that a single class of transport events drives these high velocity transport observations. The high-velocity events in Figure 5.4 above the single-kinesin stall force are therefore the

result of two kinesins working together against the optical load and do not arise due to more than two motors driving transport.

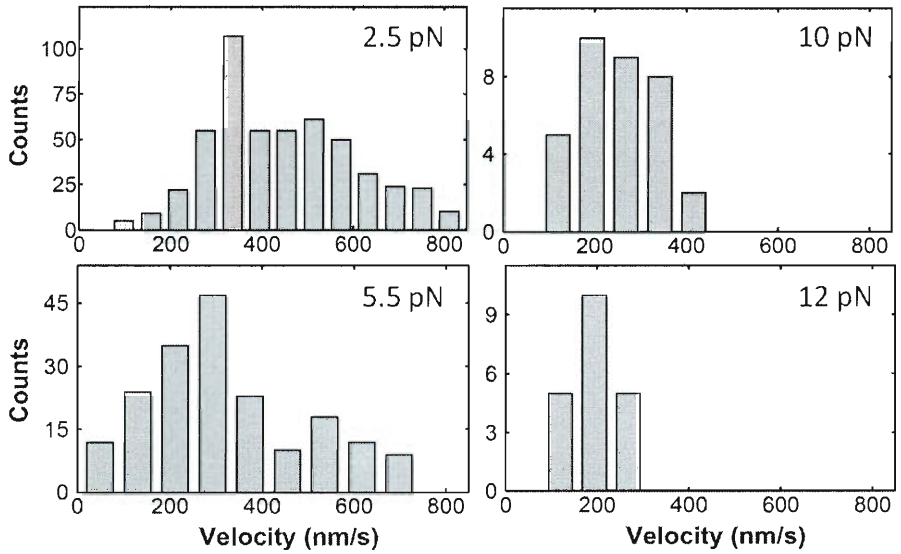

Figure 5.5: Two-Kinesin Assembly Velocity Distributions under Constant Loads Applied With a Force Clamp

Each histogram gives the velocity distribution produced by engineered two-kinesin assemblies against constant optical loads. The distributions represent the velocities produced by two-kinesin assemblies after being pulled from their microtubule-bound configurations in a static trap at 2 pN until microtubule detachment occurred. To measure velocities, a chi-squared optimization program was written in Matlab to fit the data to variable numbers of constant velocity segments. This fitting procedure is equivalent to the use of a running window average, however the optimization routines allow for variable-sized windows that better fit the data without the loss of fast velocity-transition events that would be poorly resolved by windowing. Fitted velocity segments had to have a run length greater than 16 nm and a fitted velocity error estimate less than 100 nm/s to be included. Each 16 nm of displacement were considered to be a single count for these histograms.

5.2. Two-Kinesin Bead Displacements under Constant Loads Yield Insight into Cooperative Effects

Stepping analyses for experiments done under constant load conditions have an inherent advantage over analyses of increasing load (static trap) experimentation. Positional displacements in these data sets do not have to be compliance-corrected (see Figure 3.33) as is required for those measured in the static trap. In a static trap, each time a motor progresses forward it reaches a higher force regime and is consequently stretched to a larger and larger extend in accordance with its force-extension profile (Figure 3.21); because motors stretch as they step forward, measured bead displacements are attenuated and do not give one-to-one correspondence with motor displacements. However, when a motor steps under a constant load induced by the automated optical trap in force-feedback mode, the motors do not stretch and measures of bead displacement are representative of motor displacement. Bead displacements measured for two-kinesin assemblies are presented in Figure 5.6.

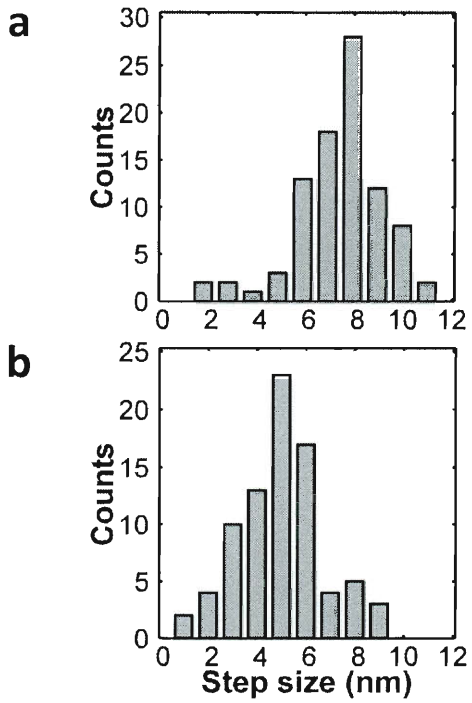

Figure 5.6: Bead Displacement Size Distributions for Two-Kinesin Assemblies in Single- and Two-Load-Bearing Motor States

(a) Bead displacements generated by two-kinesin assemblies measured at forces below the single-kinesin stall force and at velocities < 250 nm/s. (b) Two-kinesin bead displacements measured at forces > 10 pN. All steps were identified by a previously developed chi-squared optimization step-finding algorithm (Kerrsemakers, 2006).

Although motor stretching does not influence the displacement magnitudes presented in Figure 5.6, bead displacements generated by multi-motor assemblies are representative of the forward motion of the motor system's center of geometry and do not correspond to the individual displacements of the constituent motors. Kinesin motors always move forward in discrete 8 nm steps, when motors are part of a larger motor assembly each step displaces the bead a fraction of the 8 nm step size (see Figure 3.29 for theoretical calculations of the bead displacements expected for two-kinesin systems under various force regimes and microtubule-bound configurations). Using this theoretical predictions as a guide, the predominantly ~8 nm steps in Figure 5.6a demonstrate that when two-kinesin assemblies transport their cargo at low-velocities and forces less than the single-kinesin stall force they are primarily in states where one kinesin bears the optical load. Interestingly, there is a noticeable presence of small steps <4nm in magnitude also observed in Figure 5.6. Using Figure 3.24 and Figure 3.29 as guides these events likely correspond to microtubule-bound configurations where the trailing motor within the two-kinesin assembly steps forward and is separated from its partner by a distance of 40-64 nm while bearing <1 pN (~20%) of the optical load. On the other hand, Figure 5.6b demonstrates that at high forces beyond the force-production capabilities of single kinesin motors, two-kinesin assemblies produce dominant step sizes between 4-6 nm. Again using Figure 3.24 and Figure 3.29 as guides, these bead displacement magnitudes suggest that motors are separated on their microtubule track by roughly 0-40 nm, and each motor must therefore carry approximately 30-60% of the optical load at all times.

Bead displacements observed in the static optical trapping studies described in Chapter 3 revealed the possibility of a minority population of synchronized two-kinesin stepping events when two kinesins generated forces >10 pN. While the analogous feedback-based data presented in Figure 5.6b does not appear to yield highly significant numbers of synchronous stepping events (8 nm) among the motors within two-kinesin assemblies, velocities of assemblies at forces above a single kinesin's stall force are lower than their corresponding static trapping values (Figure 5.4). These depressed velocities indicate that two-kinesin assemblies are in less favorable microtubule configurations for load-sharing in feedback assays when compared to static trapping assays. Consequently, any mechanisms that may exist to synchronize motors are likely dependent on the degree to which motors share loads and therefore this behavior may be difficult to observe under the conditions of the feedback experiments where high optical loads are abruptly applied to motor assemblies once they are microtubule-bound and probabilistically in configurations that tend not to support load sharing (see Figure 4.5).

5.3. Multi-Motor Assembly Velocities Depend on Force History

The steady-state microtubule-bound configurations of multiple motor assemblies are force dependent (see Figure 4.5 and Figure 4.6), and these configurations dictate load-sharing (Figure 3.24) and velocities of motor groups (Figure 3.17). To directly examine the effects of motor-microtubule configurations on transport velocities, an experiment was designed to measure the time-dependent multiple-motor assembly velocities starting from two different sets of microtubule-bound configurations. These experiments are accomplished in two parts: (1) two-kinesin assemblies bind to microtubules and pull against a static trap to a load of 7 pN at which point the force clamp is engaged and the load is relaxed to 5 pN for as long as motors stay microtubule-bound, (2) after data has been acquired at a constant load of 5 pN, two-kinesin assemblies detach and then rebind to microtubules pulling against a static optical load to a force of 3 pN at which point the force clamp is engaged for a second time at 5 pN. The results of this experiment are presented in Figure 5.7

The data shows that 3→5 pN experiments have initial velocities near ~200 nm/s; these velocities correspond well to measures of single-kinesin velocities at 5 pN (see Figure 3.17, Figure 5.4, and Figure 5.7a). This result indicates that two-kinesin assemblies travelling along a microtubule to a load of 3 pN against the increasing load of a static optical trap (at a rate of ~ 0.5 pN/step) are most often in configurations where a single kinesin drives transport or only one assembly motor bears the optical load. In contrast, two-kinesins moving forward against higher increasing loads (at 7 pN) are

often in configurations where both motors can participate in load-sharing. Consequently, when feedback is engaged at 5 pN after conditioning of two-kinesin assemblies to 7 pN in the static trap, initial velocities observed are ~500 nm/s, even somewhat higher than two-kinesin load-bearing states measured in optical trapping studies at 5 pN (see Figure 3.17). This further suggests that two-motor assemblies which can achieve higher load production (in this case 7 pN) tend to be in microtubule-bound configurations that are advantageous for load sharing. Initial velocity distributions for both experimental cases (3→5 pN and 7→5 pN) are given in Figure 5.8.

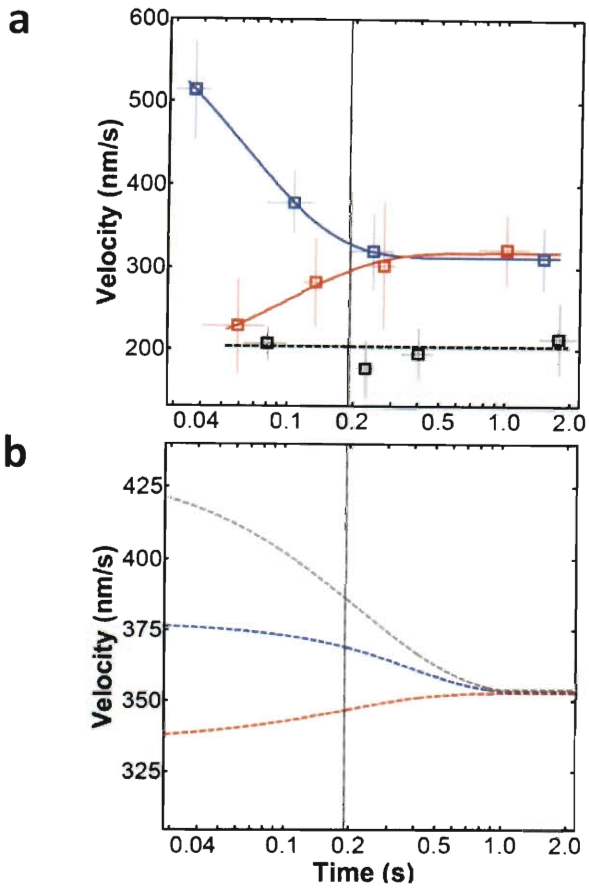

Figure 5.7: Velocity Relaxation of Two-Kinesin Assemblies under Constant Loads

(a) Experimental velocity relaxation of single-kinesin and two-kinesin assemblies. Two-kinesin velocities are shown at 5 pN (in a force clamp) after reaching 3 pN in a static trap (red squares) or after reaching 7 pN in a static trap (blue squares). The solid lines are exponential fits to each data set with time constants of 96 ms and 62 ms for the 3→5 pN and 7→5 pN cases, respectively. The vertical dashed line represents the median run time (200 ms) of force clamp events at 5 pN. Single-kinesin velocities measured at 5 pN (force clamp) after reaching 2 pN in a static trap (black squares). The black horizontal dashed line gives the time-weighted velocity mean of the single-kinesin data. All velocities are given as a time-weighted mean ± s.e.m. (b) Theoretical velocity relaxation values as determined by the previously described model (Chapter 4). Theoretical calculations are given for the 3→5 pN (red dashed line), 7→5 pN (blue dashed line), and 9→5 pN (grey dashed line) cases. The 9→5 pN case is given as theoretical maximum velocities generated by a two-kinesin assembly that starts at time equal to zero with a near equal load-sharing microtubule configuration.

In these experiments, two-kinesins very quickly approach a steady state velocity, however most events last for only a very brief duration (the median run time at 5 pN is measured as 200 ms). The exponential fit to the 7→5 pN force clamp experiment has a time constant of just 62 ms (just enough time for ~5 steps between the two motors together assuming an average single-motor dwell time of 25 ms at these forces) and the 3→5 pN case has a somewhat longer time constant of 96 ms. It is important to note that these values are not true time constants that describe the lifetime of a particular population, there are several microtubule-bound conformations which can produce two-kinesin-like velocities (and many that can also produce single-kinesin like velocities), however these time constants are representative of the loss (or gain) of configurational microstates which on average produce velocities above (or below) that of the mean steady-state distribution of configurations. While the measured time-dependent velocities in these experiments do not have the same absolute velocities as predictions (see Figure 5.7b), the theory and experiments do show general agreement in the velocity relaxation trends displayed. Motor-microtubule configurational states for the 7→5 pN case are predicted to yield higher initial velocities than the 3→5 pN case. Interestingly, the experimental velocities reach their steady-state values significantly quicker than the theory. However, in both the experimental and theoretical calculation complete relaxation of velocities to their steady-state values occurs on a time scale larger than the median run time of events under these loading conditions. This indicates that when two-kinesin assemblies experience sudden shifts in loading conditions, they can often (more than half of the time) perform transport entirely under

non-steady-state conditions before detachment of the motor system occurs. Furthermore, in a biological setting where opposite-ended motors are competing in a tug-of-war for a subcellular cargo (i.e. during bidirectional transport) loading conditions on motor groups can change abruptly effectively shortening the lifetimes of multiple-motor runs (as compared to the force clamp) and shifting much of multiple-motor behaviors to non-steady-state conditions as described in Figure 5.8.

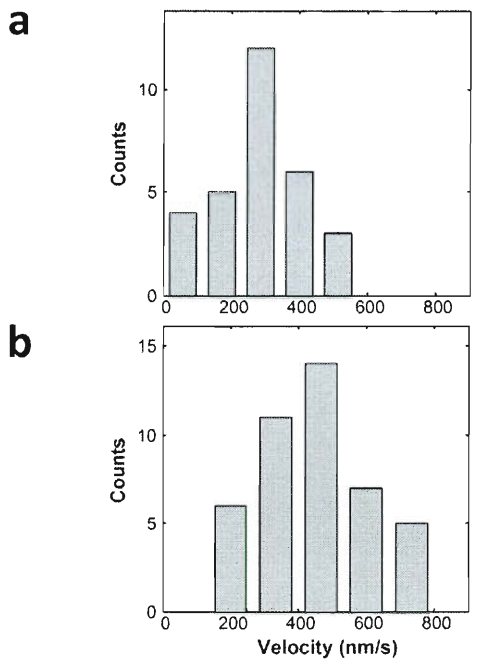

Figure 5.8: Initial Velocity Distributions of Two-Kinesin Assemblies in Velocity Relaxation Experiments

Initial velocity distributions are shown for the velocity relaxation experiments for the 3→5 pN assay (a) and the 7→5 pN assay (b).

Jeney S, Stelzer EHK, Grubmüller H,. and Florin E-L. Mechanical properties of single motor molecules studied by three-dimensional thermal force probing in optical tweezers. *ChemPhysChem* 5, 1150-1158 (2004).

Julien JP and Mushynski WE. Neurofilaments in health and disease. *Prog. Nucleic Acid Res. Mol. Bio.* 61, 1-23 (1998).

Julien JP. Neurofilament functions in health and disease. *Curr. Opin. Neurobiol.* 9, 554-560 (1999).

Kaether C, Skehel P, and Dotti CG. Axonal membrane proteins are transported in distinct carriers: a two=color video microscopy study in cultured hippocampal neurons. *Mol. Biol. Cell* 11, 1213-1224, (2000).

Kanai Y, Okada Y, Tanaka Y, Harada A, Terada S, and Hirokawa N. KIF5C, a novel neuronal kinesin enriched in motor neurons. *J. Neurosci.* 20, 6374-6384 (2000).

Kawaguchi K, Uemura S, and Ishiwata S. Equilibrium and transition between single- and double-headed binding of kinesin as revealed by single-molecule mechanics. *Biophys. J.* 84, 1103-1113 (2003).

Kerssemakers JWJ, Munteanu EL, Liedewij L, Noetzel TL, Janson ME, and Dogterom M. Assembly dynamics of microtubules at molecular resolution. *Nature* 442, 709-712 (2006).

Kimura K, Mizoguchi A, and Ide C. Regulation of Growth Cone Extension by SNARE Proteins. *J. Histochemistry & Cytochemistry* 41, 4, 429-433 (2003).

King SJ and Schroer TA. Dynactin increases the processivity of the cytoplasmic dynein motor. *Nat. Cell Biol.* 2, 20-24 (2000).

Klumpp S and Lipowsky R. Cooperative cargo transport by several molecular motors. *Proc. Natl. Acad. Sci. USA* 102, 17284-17289 (2005).

Kojima H, Muto E, Higuchi H, and Yanagida T. Mechanics of single kinesin molecules measured by optical trapping nanometry. *Biophys. J.* 73, 2012-2022 (1997).

Korn C, Klumpp S, Lipowsky R, and Schwarz US. Stochastic simulations of cargo transport by processive molecular motors. *J. Chem. Phys.* 131, 245107-245116 (2009).

Kozielski F, Sack S, Marx A, Thormahlen M, Schonbrunn E, Biou V, Thompson A, Mandelkow E-M, and Mandelkow E. The Crystal Structure of Dimeric Kinesin and Implications for Microtubule-Dependent Motility. *Cell* 91, 985-994 (1997).

Kukolka F and Niemeyer CM. Synthesis of fluorescent oligonucleotide-EYFP conjugate: Towards supramolecular construction of semisynthetic biomolecular antennae. *Organic & Biomolecular Chemistry* 2, 2203-2206 (2004).

Kulic IM, Brown AEX, Kim H, Kural C, Blehm B, Selvin PR, Nelson PC, and Gelfand VI. The role of microtubule movement in bidirectional organelle transport. *Proc. Natl. Acad. Sci. USA* 105, 10011-10016, (2008).

Kull FJ, Sablin EP, Lau R, Fletterick RJ, and Vale RD. Crystal structure of the kinesin motor domain reveals a structural similarity to myosin. *Nature* 380, 6574, 550-555 (1996).

Kunwar A, Vershinin M, Xu J, and Gross SP. Stepping, strain gating, and an unexpected force-velocity curve for multiple-motor-based transport. *Curr. Biol.* 18, 1173-1183 (2008).

Kural C, Kim H, Syed S, Goshima G, Gelfand VI and Selvin PR. Kinesin and Dynein Move a Peroxisome in Vivo: A Tug-of-War or Coordinated Movement? *Science* 308, 1469-1472 (2005).

Lang MJ, Fordyce PM and Block SM. Combined optical tweezers and single-molecule fluorescence. *J. Biology* 2, 6 (2003).

Lasek RJ, Phillips L, Katz MJ, and Autilio-Gambetti L. The function and evolution of neurofilament proteins. *Ann. NY Acad. Sci.* 455, 462-478 (1985).

LaVail JH and LaVail MM. The retrograde intraaxonal transport of horseradish peroxidase in the chick visual system: a light and electron microscopic study. *J. Comp. Neurol.* 157, 303-358 (1974).

Lawrence CJ et al. A standardized kinesin nomenclature. *J. Cell Biol.* 167, 19-22 (2004).

Leduc C, Campás O, Zeldovich KB, Roux A, Jolimaitre P, Bourel-Bonnet L, Goud B, Joanny J-F, Bassereau P, and Prost J. Cooperative extraction of membrane nanotubes by molecular motors. *Proc. Natl. Acad. Sci. USA* 101, 17096-17101 (2004).

Leduc C, Ruhnow F, Howard J, and Diez S. Detection of fractional steps in cargo movement by the collective operation of kinesin-1 motors. *Proc. Natl. Acad. Sci. USA* 104, 10847-10852 (2007).

Lee KD and Hollenbeck PJ. Phosphorylation of kinesin in vivo correlates with organelle association and neurite outgrowth. *J. Biol. Chem.* 270, 5600-5605 (1995).

Levi V, Serpinskaya AS, Gratton E, and Gelfand VI. Organelle transport along microtubules in Xenopus melanophores: Evidence for cooperation between multiple motors. *Biophys. J.* 90, 318-327 (2006).

Ligon LA, Tokito M, Finklestein JM, Grossman FE, and Holzbaur ELF. A direct Interaction between cytoplasmic dynein and kinesin-I may coordinate motor Activity. *J. Biol. Chem.* 279, 19201-19208 (2004).

Lipowsky R, Klumpp S, and Neiuwenhuizen TM. Random Walks of Cytoskeletal Motors in Open and Closed Compartments. *Phys. Rev. Lett.* 87, 108101 (2001).

Liu Y, Lin C, Li H, and Yan H. Aptamer-directed self-assembly of protein arrays on a DNA nanostructures. *Angew. Chem. Int. Ed.* 44, 4333-4338 (2005).

Lovrinovic M, Spengler M, Deutsch C, and Niemeyer CM. Synthesis of covalent DNA-protein conjugates by expressed protein ligation. *Mol. BioSyst.* 1, 64-69 (2005).

Mallik R, Carter BC, Lex SA, King SJ, and Gross SP. Cytoplasmic dynein functions as a gear in response to load. *Nature* 427, 649-652 (2004).

Mallik R, Petrov D, Lex SA, King SJ, and Gross SP. Building Complexity: An In Vitro Study of Cytoplasmic Dynein with In Vivo Implications. *Current Biology*, 15, 2075-2085 (2005).

Marszalek JR, Ruiz-Lozano P, Roberts E, Chien KR, and Goldstein LS. Situs inversus and embryonic ciliary morphogenesis defects in mouse mutants lacking the KIF3A subunit of kinesin-II. *Proc. Natl Acad. Sci. USA* 96, 5043–5048 (1999).

Miki H, Setou M, Kaneshiro K, and Hirokawa N. All kinesin superfamily protein, KIF, genes in mouse and human. *Proc. Natl. Acad. Sci. USA* 98, 7004-7011 (2001).

Miller RH and Lasek RJ. Cross-bridges mediate anterograde and retrograde vesicle transport along microtubules in squid axoplasm. *J. Cell Biol.* 101, 2181-2193 (1985).

Miyazono Y, Hayashi M, Karagiannis P, Harada Y, and Tadakuma H. Strain through the neck linker ensures processive runs: a DNA-kinesin hybrid nanomachine study. *EMBO J.* 29, 1, 93-106 (2010).

Moll JR, Ruvinov SB, Pastan I, and Vinson C. Designed heterodimerizing leucine zippers with a range of pIs and stabilities up to 10^{-15}. *M. Protein Sci.* 10, 649-655 (2001).

Mori T, Vale RD, and Tomishige M. How kinesin waits between steps. *Nature* 450, 750-755 (2007).

Morifini G, Szebenyi G, Elluru R, Ratner N, and Brady ST. Glycogen synthase kinase 3 phosphorylates kinesin light chains and negatively regulates kinesin-based motility. *EMBO J.* 21, 281-293 (2002).

Morifini G, Pigino G, Szebenyi G, You Y, Pollema S, and Brady ST. JNK mediates pathogenic effects of polyglutamine-expanded androgen receptor on fast axonal transport. *Nature Neuroscience.* 9, 907-916 (2006).

Muller MJI, Klumpp S, and Lipowski R. Tug-of-war as a cooperative mechanism for bidirectional cargo transport by molecular motors. *Proc. Natl. Acad. Sci. USA* 105, 4609-4614 (2008).

Nan X, Sims PA, Chen P, and Xie XS. Observation of Individual Microtubule Motor Steps in Living Cells with Endocytosed Quantum Dots. *J. of Phys. Chem B* 109, 24220-24224 (2005).

Nangaku M, Sato-Yoshitake R, Okada Y, Noda Y, Takemura R, Yamazaki H, and Hirokawa N. KIF1B, a novel microtubule plus end-directed monomeric motor protein for transport of mitochondria. *Cell* 79, 1209-1220 (1994).

Niemeyer CM, Sano T, Smith CL, and Cantor CR. Oligonucleotide-directed self-assembly of proteins: semisynthetic DNA-streptavidin hybrid molecules as connectors for the generation of macroscopic arrays and the construction of supramolecular bioconjugates. *Nucleic Acids Res.* 22, 5530-5539 (1994).

Niemeyer CM, Adler M, Pignataro B, Lenhert S, Gao S, Chi L, Fuchs H, and Blohm D. Self-assembly of DNA-streptavidin nanostructures and their use as reagents in immuno-PCR. *Nucl. Acids Res.* 27, 4553-4561 (1999).

Nishiyama M, Higuch H, and Yanagida T. Chemomechanical coupling of the forward and backward steps of single kinesin molecules. *Nature Cell Biology* 4, 790-797 (2002).

Nonaka S, Tanaka Y, Okada Y, Takeda S, Harada A, Kanai Y, Kido M, and Hirokawa N. Randomization of left–right asymmetry due to loss of nodal cilia generating leftward flow of extraembryonic fluid in mice lacking KIF3B motor protein. *Cell* 95, 829–837 (1998).

Nusslein-Volhard C, Fronhnhofer HG, and Lehmann R. Determination of anteroposterior polarity in Drosophila. *Science* 238, 1675-1681 (1987).

Ori-McKenney KM, Xu J, Gross SP, and Vallee RB. A cytoplasmic dynein tail mutation impairs motor processivity. *Nat.Cell Bio.* 12, 1228-1234 (2010).

Peterman EJG, van Dijk MA, Kapitein LC, and Schmidt CF. Extending the bandwidth of optical-tweezers interferometry. *R. of Sci. Inst.* 74, 7, 3246-3249 (2003).

Presley JF, Cole NB, Schroer TA, Hirschberg K, Zaal KJ, and Lippincott-Schwartz J. ER-to-Golgi transport visualized in living cells. *Nature* 389, 81-85 (1997).

Reck-Peterson SL, Yildiz A, Carter AP, Gennerich A, Zhang N, and Vale RD. Single-molecule analysis of dynein processivity and stepping behavior. *Cell* 126, 335-348 (2006).

Reid E, Kloos M, Ashley-Koch A, Hughes L, Bevan S, Svenson IK, Graham FL, Gaskell PC, Dearlove A, Pericak-Vance MA, Rubinsztein DC, and Marchuk DA. A kinsin heavy chain (KIF5A) mutation in hereditary spastic paraplegia (SPG10). *Am J Hum Genet*. 71, 1189-94 (2002).

Rice S, Lin AW, Safer D, Hart CL, Naber N, Carragher BO, Cain SM, Pechatnikova I, Wilson-Kubalek EM, Whittaker M, Pate E, Cooke R, Taylor EW, Milligan RA, and Vale RD. A structural change in the kinesin motor protein that drives motility. *Nature* 402, 6763, 778-784 (1999).

Rohrbach A and Stelzer EHK. Optical trapping of dielectric particles in arbitrary fields. *J. Opt. Soc. Am. A.* 18, 4, 839-853. (2001).

Rogers SL, Tint IS, Fanapour PC, and Gelfand VI. Regulated bidirectional motility of melanophore pigment granules along microtubules in vitro. *Proc. Natl. Acad. Sci. USA* 94, 3720-3725. (1997).

Rogers AR, Driver JW, Constantinou PE, Jamison DK, and Diehl MR. Negative interference dominates collective transport of kinesin motors in the absence of load. *Phys. Chem. Chem. Phys.* 11, 4882-4889 (2009).

Ross JL, Shuman H, Holzbaur ELF, and Goldman YE. Kinesin and dynein-dynactin at intersecting microtubules: motor density affects dynein function. *Biophys. J.* 94, 3115-3125 (2008).

Sato-Yoshitake R, Yorifuji H, Inagaki M and Hirokawa N. The phosphorylation of kinesin regulates its binding to synaptic vesicles. *J. Biol. Chem*. 267, 23930-23936 (1992).

Schnitzer MJ, Visscher K, and Block SM. Force production by single kinesin motors. *Nat. Cell Biol.* 2, 718-723 (2000).

Schroer TA, Brady ST and Kelly RB. Fast axonal transport of foreign synaptic vesicles in squid axoplasm. *J. Cell Bio.* 101, 568-572 (1985).

Schweller RM, Constantinou PE, Frankel NW, Narayan P, and Diehl MR. Design of DNA-conjugated polypeptide-based capture probes for the anchoring of proteins to DNA matrices. *Bioconjug. Chem.* 19, 2304-2307 (2008).

Seitz A, Kojima H, Oiwa K, Mandelkow EM, Song Y-H, Mandelkow E. Single-molecule investigation of the interference between kinesin, tau and MAP2c. *EMBO J.* 21, 18, 4896-4905 (2002).

Shastry S, Hancock WO. Neck linker length determines the degree of processivity in kinesin-1 and kinesin-2 motors. *Curr. Biol.* 29, 10, 939-943 (2010).

Shubeita GT, Tran SL, Xu J, Vershinin M, Cermelli S, Cotton SL, Welte MA, and Gross SP. Consequences of motor copy number on the intracellular transport of Kinesin-1-driven lipid droplets. *Cell* 135, 1098-1107 (2008).

Simmons RM, Finer JT, Chu S, and Spudich JA. Quantitative measurements of force and displacement using an optical trap. *Biophys J.* 70, 1813–1822 (1996).

Sims PA and Xie XS. Probing dynein and kinesin stepping with mechanical manipulation in a living cell. *Chem. Phys. Chem.* 10, 1511-1516 (2009).

Soppina V, Rai AK, Ramaiya AJ, Barak P, and Mallik R. Tug-of-war between dissimilar teams of microtubule motors regulates transport and fission of endosomes. *Proc. Natl. Acad. Sci. USA* 106, 19381-19386 (2009).

Stagi M, Gorlovoy P, Larionov S, Takahashi K, and Neumann H. Unloading kinesin in transported cargoes from the tubulin track via the inflammatory c-Jun N-terminal kinase pathway. *FASEB J.* 20, 2573-2575 (2006).

Stauber T, Simpson JC, Pepperkok R, and Vernos I. A role for kinesin-2 in COPI-dependent recycling between the ER and the Golgi complex. *Curr. Biol.* 16, 2245-2251 (2006).

Stokin GB, Lillo C, Falzone TL, Brusch RG, Rockenstein E, Mount SL, Raman R, Davies P, Masliah E, Williams DS, and Goldstein LSB. Axonopathy and Transport Deficits Early in the Pathogenesis of Alzheimer's Disease. *Science* 307, 1282-1288 (2005).

Svoboda K, Schmidt CF, Schnapp BJ, and Block SM. Direct observation of kinesin stepping by optical trapping interferometry. *Nature* 365, 721-727 (1993).

Svoboda K. Biological Applications of Optical Forces. *Annu. Rev. Biophys. Biomol. Struct.* 23, 247-285 (1994).

Svoboda K and Block SM. Force and velocity measured for single kinesin molecules. *Cell* 77, 773-784 (1994).

Takeda S, Yonekawa Y, Tanaka Y, Okada Y, Nonaka S, and Hirokawa N. Left–right asymmetry and kinesin superfamily protein KIF3A: new insights in determination of laterality and mesoderm induction by *kif3A–/–* mice analysis. *J. Cell Biol.* 145, 825–836 (1999).

Tanaka Y, Kanai Y, Okada Y, Nonaka S, Takeda S, Harada A, and Hirokawa N. Targeted disruption of mouse conventional kinesin heavy chain, kif5B, results in abnormal perinuclear clustering of mitochondria. *Cell* 93, 1147-1158 (1998).

Teng J, Rai T, Tanaka Y, Takei Y, Nakata T, Hirasawa M, Kulkarni AB, and Hirokawa N. The KIF3 motor transports N-cadherin and organizes the developing neuroepithelium. *Nature Cell Biol.* 7, 474–482 (2005).

Tolic-Norrelykke SF, Schaffer E, Howard J, Pavone FS, Julicher F, and Flyvbjerg H. Calibration of optical tweezers with positional detection in the back focal plane. *R. of Sci. Inst.* 77, 103101, 1–11 (2006).

Urry DW. Physical chemistry of biological free energy transduction as demonstrated by elastic protein-based polymers. *J. Phys. Chem. B* 101, 11007-11028 (1997).

Urry DW, Hugel T, Seitz M, Gaub HE, Sheiba L, Dea J, Xu J, and Parker T. Elastin: a representative ideal protein elastomer. *Phil. Trans. R. Soc. Lond. B* 357, 169-184 (2002).

Vale RD, Reese TS, and Sheetz MP. Identification of a novel force-generating protein, kinesin, involved in microtubule-based motility. *Cell* 42, 39-50 (1985).

Vale RD. Switches, latches, and amplifiers: common themes of G proteins and molecular motors. *J. Cell Biol.* 135, 291-302 (1996).

Vale RD, Funatsu T, Pierce DW, Romberg L, Harada Y, and Yanagida T. Direct observation of single kinesin molecules moving along microtubules. *Nature* 380, 451-453 (1996).

Vale RD. The molecular motor toolbox for intracellular transport. *Cell.* 112,467-480 (2003).

Valentine MT, Fordyce PM, Krzysiak TC, Gilbert SP, and Block SM. Individual dimers of the mitotic kinesin motor Eg5 step processively and support substantial loads *in vitro*. *Nature Cell Biology* 8, 5, 470-476 (2006).

Vershinin M, Carter BC, Razafsky DS, King SJ, and Gross SP. . Multiple-motor based transport and its regulation by Tau. *Proc. Natl. Acad. Sci. USA* 104, 87-92 (2007).

Visscher K and Brakenhoff GJ. Theoretical study of optically induced forces on spherical particles in a single beam trap I: Rayleigh scatterers. *Optik* 89, 174-80 (1992).

Visscher K, Gross SP, and Block SM. Construction of Multiple-Beam Optical Traps with Nanometer-Resolution Position Sensing. *IEEE Journal of Selected Topics in Quantum Electronics* 2, 4, 1066-1077 (1996).

Visscher K, Block SM. Versatile Optical Traps With Feedback Control. *Methods in Enzymology.* 298, 460-489 (1998).

Visscher K, Schnitzer MJ, and Block SM. Single kinesin molecules studied with a molecular force clamp. *Nature* 400, 184-189 (1999).

Wang MC and Uhlenbeck GE. On the theory of the Brownian motion II. *Rev, Mod. Phys*. 17, 323-41; Reprinted in Selected Papers on Noise and Stochastic Processes, ed. N Wax, 113- 32. New York, NY: Dover (1945).

Wang Z, Khan S, and Sheetz MP. Single cytoplasmic dynein molecule movements: characterization and comparison with kinesin. *Biophys. J.* 69, 2011-2023 (1995).

Wang Z and Li M. Force-velocity relations for multiple-molecular-motor transport. *Phys. Rev. E* 80, 041923 (2009).

Weber G and Greulich KO. Manipulation of cells, organelles, and genomes by laser microbeam and optical trap. *Int. Rev. Cytol.* 133, 1-41 (1992).

Wedaman KP, Meyer DW, Rashid DJ, Cole DG, and Scholey JM. Sequence and submolecular localization of the 115-kD accessory subunit of the heterotrimeric kinesin-II (KRP85/95) complex. *J. Cell Biol.* 132, 371-380 (1996).

Welte M, Gross SP, Postner M, Block SM and Wieschaus EF. Developmental and genetic regulation of vesicle transport in drosphila embryos. *Cell* 92, 547-557 (1998).

Welte MA. Bidirectional transport along microtubules. *Curr. Biol.* 14, R525-R537 (2004).

Wong RW, Setou M, Teng J, Takei Y, and Hirokawa N. Overexpression of motor protein KIF17 enhances spatial and working memory in transgenic mice. *Proc. Natl Acad. Sci. USA* 99, 14500–14505 (2002).

Wong YL, Dietrich A, Naber N, Cooke R, and Rice SE. The kinesin-1 tail conformationally restricts the nucleotide pocket. *Biophys J.* 96, 2799-2807 (2009).

Wozniak MJ, Melzer M, Dorner C, Haring HU, and Lammers R. The novel protein KBP regulates mitochondria localization by interaction with a kinesin-like protein. *BMC Cell Biol.* 6, 35-49 (2005).

Xia C, Roberts EA, Her L, Liu X, Williams DS, Cleveland DW, and Goldstein LSB. Abnormal neurofilament transport cause by targeted disruption of neuronal kinesin heavy chain KIF5A. *J. of Cell Biol.* 61, 55-66 (2003).

Yan H, Park SH, Finkelstein G, Reif JH, and LaBean TH. DNA-templated self-assembly of protein arrays and highly conductive nanowires. *Science* 301, 1882-1884 (2003).

Yildiz A, Tomishige M, Vale RD, and Selvin PR. Kinesin walks hand-over-hand. *Science* 303, 676-678 (2004).

Zerial M and McBride H. Rab proteins as membrane organizers. *Nature Rev. Mol. Cell Biol.* 2, 107-117 (2001).

Zochodne DW. Is early diabetic neuropathy a disorder of the dorsal root ganglion? A hypothesis and critique of some current ideas on the etiology of diabetic neuropathy. *J. Peripher. Nerv. Syst*. 1, 119-130 (1996).

5.4. Future Directions for the Study of Intracellular Transport

Through a multi-faceted experimental and theoretical approach, this body of work has illuminated many fundamental behaviors of paired kinesin-1 motor proteins. Surprisingly, kinesin motors in small groups are shown to function most often as a single motor. This behavior arises predominantly due to multiple motors binding to microtubules in configurations that are not amenable to load-sharing. The propensity for multiple motors to bind into such non-cooperative microtubule-bound states is the result of the inherent geometry and mechanics of motor groups pulling spherical cargos along filament tracks, hence, many of the findings here are believed to apply broadly to motor-driven intracellular processes. However, the theoretical treatments presented in Chapter 4 have predicted different and intriguing behaviors for motors (e.g., dynein) that differ fundamentally in their mechanochemical stepping characteristics. Namely, motors with less efficient stepping mechanisms are expected to cooperative more productively than kinesin motors. Experiments that probe the potentially cooperative dynamics of dynein motors are of critical importance to bridge the gap between what is now known of kinesin motor cooperativity and intracellular transport processes that potentially utilize multiple motor groups comprised of different motor types (i.e., kinesin, dynein, and even myosin). However, experimental investigations that examine dynein motors have proven to be difficult in practice, in large part due to dynein's immense size and complications associated with obtaining active samples suitable for single-molecule-level investigations of dynein mechanochemistry. Hence, relatively

Appendix: Protocols for Optical Trapping Assays and Synthesis of Engineered Two-Kinesin Motor Assemblies

A1. Axoneme Purification Protocol

Note: this protocol was modified from a previously developed purification scheme (Gibbons, 1979). The following buffers are needed for the procedure:

Buffer 1 (Low Salt)

20mM Hepes pH7.0
100mM NaCl
4mM $MgSO_4$
1mM $CaCl_2$
0.1mM EDTA
0.1mM ATP
7mM βME

Buffer 2 (High Salt)

20mM Hepes pH7.0
600mM NaCl
4mM $MgSO_4$
1mM $CaCl_2$
0.1mM EDTA
7mM βME
1mM DTT

Obtaining sperm:

1. Obtain 4-8 male sea urchins if possible (or just treat both males and females with KCl and only use those producing sperm)
2. Appling electric current to the top of the sea urchin, next to the anus will lead to a small release of sperm (white) or eggs (pink). Select only those producing sperm.
3. Turn sea urchins over. Inject 0.5 M KCl. Slide the needle into the soft tissue surrounding the mouth. Do not inject too much KCl to start with as this can lead to no sperm release

little is known about the dynein motor. New techniques for purification, molecular manipulation, or live cell imaging of dynein are likely needed to progress the field on this front.

While intracellular motor proteins are known to work in groups larger than two. The evidence presented throughout this thesis indicates that multiple-motor assemblies of more than two motors will suffer from the same geometric constraints as two motors, at least for the case of kinesin. However, within cells, cargos have the potential to be transported by several motor groups separated by relatively large distances on a cargo that move on separate filament tracks. Theoretical treatments that successfully model these larger scale systems hold potential to bridge the gap in understanding between the behaviors of multiple-motor units and the more complex physiological functions that utilize the motor protein machinery of the cell.

Ultimately, understanding intracellular transport processes at a mechanistic level requires specific knowledge of motor cooperativity across motor types and assembly configurations as well as the regulatory factors that can direct motor groups. Through a combination of experimental and theoretical approaches these studies have uncovered the principles that define how multiple-kinesin motors function collectively. Other higher-order regulatory mechanisms may still act on top of these foundational behaviors to control intracellular transport. Yet, the intrinsic structure-function rules that govern multiple-motor systems, as described here, must be integral to mechanisms that regulate intracellular transport.

Summary of Chapter 5

The force and velocity capabilities of multiple-kinesin assemblies are dependent on the force history experienced by these systems. Motor assemblies have steady-state motor-motor-microtubule configurations that favor load-sharing configurations under greater load. Here, the dynamic force-velocity behaviors of multiple-kinesin systems were examined under distinct series of loading conditions by utilizing an optical trapping system switching between static and force clamp modes. As predicted by the theoretical model presented in Chapter 4, experimentally-measured multi-motor assembly velocities depend on the force history experienced by the system. Furthermore, motor assemblies are found to reach their steady-state microtubule-configuration distribution and force-velocity behaviors on time-scales that are relatively long in comparison to the time-scales over which loading conditions are expected to change in biologically relevant transport scenarios. Therefore, multiple-motor assemblies *in vivo* should spend the majority of their time in non-steady-state configurations that are critically dependent on the force-history against which motors operate.

Constant-load experiments also reproduce the results of the increasing-load (static trap) behaviors described in Chapter 3; multiple-kinesin assemblies in general adopt microtubule-configurations that do not allow significant load-sharing, they most often act as a single kinesin motor and step asynchronously when they can share load.

Together, the behaviors observed here are of critical importance for understanding transport phenomena such as bidirectional transport where competing groups of motors interact with one another in a manner which can significantly affect the performance of both motor groups and ultimately determines the transport of such cargos.

References

Adams RJ and Bray D. Rapid transport of foreign particles microinjected into crab axons. *Nature* 303, 718–720 (1983).

Ali MY, Lu H, Bookwalter CS, Warshaw DM, and Trybus KM. Myosin V and kinesin act as tethers to enhance each others' processivity. *Proc. Natl. Acad. Sci. USA*. 105, 4691-4696 (2008).

Ally S, Larson AG, Barlan K, Rice SE, and Gelfand VI. Opposite-polarity motors activate one another to trigger cargo transport in live cells. *J. Cell Biol.* 187, 1071-1082 (2009).

Amos LA. Microtubule structure and its stabilisation. *Org. Biomol. Chem.* 15, 2153-2160 (2004).

Asbury CL, Fehr AN, and Block SM. Kinesin moves by an asymmetric hand-over-hand mechanism. *Science* 302, 2130-2134 (2003).

Ashkin A, Dziedzic JM, and Yamane T. Optical trapping and manipulation of single cells using infrared laser beams. *Nature* 330, 769-771 (1987).

Ashkin A., Schutze K, Dziedzic JM, Euteneuer U, and Schliwa M. Force generation of organelle transport measured *in vivo* by an infrared laser trap. *Nature* 348, 346-348 (1990).

Ashkin A.. Forces of a single-beam gradient laser trap on a dielectric sphere in the ray optics regime. *Biophys. J.* 61, 569-582 (1992).

Bananis E, Murray JW, Stockert RJ, Satir P, and Wolkoff AW. Microtubule and motor-dependent endocytic vesicle sorting in vitro. *J. Cell Biol.* 151, 179-186 (2000).

Barton JP, Alexander DR, and Schaub SA. Internal and near-surface electromagnetic fields for a spherical particle irradiated by a focused laser beam. *J. Appl. Phys.* 64, 1632-39 (1988).

Beeg J, Klumpp S, Dimova R, Gracia RS, Unger E, and Lipowsky R. Transport of beads by several kinesin motors. *Biophys. J.* 94, 532-541 (2008).

Berns MW, Wright WH, Steubing RW. Laser microbeam as a tool in cell biology. *Int. Rev. Cytol.* 129, 1-44 (1991).

Block SM, Goldstein L, Schnapp BJ. Bead movement by single kinesin molecules studied with optical tweezers. *Nature* 348, 348-352 (1990).

Bohm KJ, Stracke R, and Unger E. Speeding up kinesin-driven microtubule gliding in vitro by variation of cofactor composition and physicochemical parameters. *Cell Biol. Int.* 24, 335-341 (2000).

Bornschlogl T, Woehlke G, and Rief M. Single molecule mechanics of the kinesin neck. *Proc. Natl. Acad. Sci.* 106, 17, 6992-6997 (2009).

Bruno L, Echarte MM, and Levi V. Exchange of microtubule molecular motors during melanosome transport in *Xenopus laevis* melanophores is triggered by collisions with intracellular obstacles. *Cell Biochem. Biophys.* 52, 191-201 (2008).

Byrd DT, Kawasaki M, Walcoff M, Hisamoto N, Matsumoto K, and Jin Y. UNC-16, a JNK-signaling scaffold protein, regulates vesicle transport in *c. elegans*. *Neuron* 32, 787-800 (2001).

Campas O, Leduc C, Basserea P, Casademunt J, Joanny J, and Prost J. Coordination of kinesin motors pulling on fluid membranes. *Biophys. J.* 94, 5009-5017 (2008).

Carter BC, Vershinin M, Gross SP. A Comparison of Step-Detection Methods: How Well Can You Do? *Biophysical J.* 94, 306-319 (2008).

Carter NJ and Cross RA. Mechanics of the kinesin step. *Nature* 435, 308-312 (2005).

Constantinou PE and Diehl MR. The mechanochemistry of integrated motor protein complexes. *J. Biomech.* 43, 31-37 (2009).

Coppin CM, Pierce DW, Long H, and Vale RD. The load dependence of kinesin's mechanical cycle. *Proc. Natl. Acad. Sci. USA* 94, 1913-1917 (1997).

Diehl MR, Zhang K, Lee HJ, and Tirrell DA. Engineering cooperativity in biomotor-protein assemblies. *Science* 311, 1468-1471 (2006).

Dietrich KA, Sindelar CV, Brewer PD, Downing KH, Cremo CR, and Rice SE. The kinesin-1 motor protein is regulated by a direct interaction of its head and tail. *Proc. Natl Acad. Sci. USA* 105, 8938-8943 (2008).

Driver JW, Rogers AR, Jamison DK, Das RK, Kolomeisky AB, and Diehl MR. Coupling between motor proteins determines dynamic behaviors of motor protein assemblies. *Phys. Chem. Chem. Phys.* 12, 10398-10405 (2010).

Duke T. Cooperativity of myosin molecules through strain-dependent chemistry. *Philosophical Transactions of the Royal Society of London Series B-Biological Sciences* 355, 529-538 (2000).

Ebneth A, Godemann KS, Illenberger S, Trinczek B, Mandelkow E, and Mandelkow E. Overexpression of Tau Protein Inhibits Kinesin-dependent Trafficking of Vesicles, Mitochondria, and Endoplasmic Reticulum: Implications for Alzheimer's Disease. *J. Cell Biology*, 143, 3, 777-794 (1998).

Evans E. Probing the relation between force-lifetime and chemistry in single molecular bonds. *Ann. Rev. Biophys. Biomol. Struct.* 30, 105-128 (2001).

Fahim MA, Lasek RJ, Brady ST, and Hodge A. AVEC-DIC and electron microscope analyses of axonally transported particles in cold-blocked squid giant axons. *J. Neurocytol.* 14, 689-704 (1985).

Fehr AN, Asbury CL, and Block SM. Kinesin steps do not alternate in size. *Biophys. J.* 94, L20-L22 (2008).

Fehr AN, Gutiérrez-Medina B, Asbury CL, and Block SM. On the origin of kinesin limping. *Biophys. J.* 97, 1663-1670 (2009).

Fisher ME and Kim YC. Kinesin crouches to sprint but resists pushing. *Proc. Natl. Acad. Sci. USA* 102, 16209-16214 (2005).

Gennerich A and Schild D. Finite-particle tracking reveals submicroscopic-size changes of mitochondria during transport in mitral cell dendrites. *Phys. Biol.* 3, 45-53 (2006).

Gennerich A, Carter AP, Reck-Peterson SL, and Vale RD. Force-Induced Bidirectional Stepping of Cytoplasmic Dynein. *Cell* 131, 5, 952-965 (2007).

Gibbons IR and Fronk EA. Latent adenosine triphosphatase form of dynein 1 from sea urchin sperm flagella. *J. Biol. Chem.* 254, 187-196 (1979).

Gittes F, Meyhofer E, Baek S, and Howard J. Directional loading of the kinesin motor molecule as it buckles a microtubule. *Biophys. J.* 70, 418-429 (1996).

Gittes F and Schmidt CF. Interference model for back-focal-plane displacement detection in optical tweezers. *Optics Letters* 23, 1, 7-9 (1998).

Grafstein B and Forman DS. Intracellular transport in neurons. *Physiol. Rev.* 60, 1167-1283 (1980).

Goldstein L.S. With apologies to Scheherazade: tails of 1001 kinesin motors. *Ann. Rev. Genetics* 27, 319-351 (1993).

Goldstein LSB. Kinesin molecular motors: Transport pathways, receptors, and human disease. *Proc. Natl. Acad. Sci. USA* 98, 6999-7003 (2001).

Gordon JP. Radiation forces and momenta in dielectric media. *Phys. Rev. A* 8, 14-21 (1973).

Gross SP, Welte MA, Block SM, and Wieschaus EF. Coordination of opposite-polarity microtubule motors. *J. Cell Biol.* 156, 715-724 (2002).

Guydosh NR and Block SM. Backsteps induced by nucleotide analogs suggest the front head of kinesin is gated by strain. *Proc. Natl. Acad. Sci. USA* 103, 21, 8054-8059 (2006).

Hammond JW, Cai D, Blasius TL, Li Z, Jiang Y, Jih GT, Meyhofer E, and Verhey KJ. Mammalian kinesin-3 motors are dimeric in vivo and move by processive motility upon release of Autoinhibition. *PLoS Biol.* 7, e72 (2009).

Hancock WO and Howard J. Processivity of the motor protein kinesin requires two heads. *J. Cell. Biol.* 140, 1395-1405 (1998).

Hendricks AG, Perlson E, Ross JL, Schroeder HW, Tokito M, and Holzbaur EL. Motor coordination via a tug-of-war mechanism drives bidirectional vesicle transport. *Curr. Biol.* 20, 697-702 (2010).

Higuchi H, Bronner CE, Park H, and Endow SA. Rapid double 8-nm steps by a kinesin mutant. *EMBO J.* 23, 2993-2999 (2004).

Hill DB Changes in the number of molecular motors driving vesicle transport in PC12. PhD thesis. Wake Forest University, Winston-Salem (2003).

Hill DB, Plaza MJ, Bonin K, and Holzwarth G. Fast vesicle transport in PC12 neurites: Velocities and forces. *Eur. Biophys. J.* 33, 623-632 (2004).

Hirokawa N. Kinesin and dynein superfamily proteins and the mechanism of organelle transport. *Science* 279, 519-526 (1998).

Hirokawa N and Noda Y. Intracellular transport and kinesin superfamily proteins, KIFs: structure, function, and dynamics. *Physiol. Rev.* 88, 1089-1118 (2008).

Hirokawa N, Noda Y, Tanaka Y, and Niwa S. Kinesin superfamily motor proteins and intracellular transport. *Nature Reviews Molecular Cell Biology* 10; 682-696 (2009).

Holzbaur EL and Goldman YE. Coordination of molecular motors: from in vitro assays to intracellular dynamics. *Curr. Opin. Cell Biol.* 22, 4-13 (2010).

Holzwarth G, Bonin K, and Hill DB. Forces Required of Kinesin during Processive Transport through Cytoplasm. *Biophys. J.* 82, 1784-1790 (2002).

Homma N, Takei Y, Tanaka Y, Nakata T, Terada S, Kikkawa M, Noda Y, and Hirokawa N. Kinesin superfamily protein 2A (KIF2A) functions in suppression of collateral branch extension. *Cell* 114, 229–239 (2003).

Horiuchi D, Collins CA, Bhat P, Barkus RV, DiAntonio D, and Saxton WM. Control of a kinesin-cargo linkage mechanism by JNK pathway kinases. *Current Biol.* 17, 1313-1317 (2007).

Howard J. Mechanics of motor proteins and the cytoskeleton. Sunderland, MA: Sinauer Associates (2001).

Hunt AJ, Gittes F, Howard J. The force exerted by a single kinesin molecule against a viscous load. *Biophys. J.* 67, 766 (1994).

Hurd DD and Saxton WM. Kinesin mutations cause motor neuron disease phenotypes by disrupting fast axonal transport in *Drosophila*. *Genetics* 144, 1075-1085 (1996).

Hyman AA and Mitchison TJ. Two different microtubule-based motor activities with opposite polarities in kinetochores. *Nature* 351, 206-211 (1991).

Jamison DK, Driver JW, Rogers AR, Constantinou PE and Diehl MR. Two kinesins transport cargo primarily via the action of one motor: implications for intracellular transport. *Biophys. J.* 99, 2967-2977 (2010).

ATP (Sigma A2383)

Make a 200 mM stock (110 mg in 1 mL). Make 12 µL aliquots, snap freeze, and store at -80 C. Also make a small number of 500 µL stocks for purifications, snap freeze, and store at -80 C.

Lysis Buffer (1000 mL)

50 mM phosphate, pH 8.0: 0.47 g Sodium phosphate, monobasic monohydrate (Sigma 71507), 6.61 g Sodium phosphate, dibasic (Sigma S3264)

250 mM NaCl: 14.61 g NaCl (Sigma S3014)

2 mM $MgCl_2$: 2 mL Magnesium chloride solution (Sigma M1028)

20 mM Imidazole: 1.36 g Imidazole (Sigma I5513)

100 µM EDTA: 37 mg EDTA (Sigma E5134)

Before use of 50 mL lysis buffer add:

10 µM bestatin: 250 µL of 2 mM bestatin stock (-20 C refrigerator)

1 µM phosphoramidon: 5 µL of 10 mM phosphoramidon stock (-20 C refrigerator)

1 mM pefabloc: 12 g/500 µL of pefabloc/ 100 mM pefabloc stock (4 C refrigerator)

1 µg/mL aprotinin: 5 µL of 10 mg/mL aprotinin stock (4 C refrigerator)

10 µM leupeptin: 50 µL of 10 mM leupeptin stock (-20 C refrigerator)

5 µM E-64: 125 µL of 2 mM E-64 stock (-20 C refrigerator)

1 µM pepstatin: 50 µL of 1 mM pepstatin stock (-20 C refrigerator)

1 mM TAME: 500 µL of 100 mM TAME stock (-20 C refrigerator)

1 mM ATP: 250 µL of 200 mM ATP stock (-80 C refrigerator)

1 mM βME: 3.5 µL of 14.3 M βME (Sigma 63689)

Ni Wash Buffer (400 mL)

50 mM phosphate, pH 7.2: 0.87 g of Sodium phosphate, monobasic monohydrate (Sigma 71507), 1.94 g Sodium phosphate, dibasic (Sigma S3264)

250 mM NaCl: 5.84 g NaCl (Sigma S3014)

1 mM $MgCl_2$: 0.4 mL of Magnesium chloride solution (Sigma M1028)

20 mM Imidazole: 0.54 g of Imidazole (Sigma I5513)

Before use of 40 mL wash buffer add:

100 µM ATP: 20 µL of 200 mM ATP stock (-80 C refrigerator)

2 mM βME: 5.6 µL of 14.3 M BME (Sigma 63689)

Ni Elution Buffer (40 mL)

50 mM phosphate, pH 7.6: 43 mg of Sodium phosphate, monobasic monohydrate (Sigma 71507), 240 mg of Sodium phosphate, dibasic (Sigma S3264)

250 mM NaCl: 584 mg of NaCl (Sigma S3014)

1 mM $MgCl_2$: 40 µL of Magnesium chloride solution (Sigma M1028)

400 mM Imidazole: 1.09 g of Imidazole (Sigma I5513)

Before use of 4 mL elution buffer add:

100 µM ATP: 2 µL of 200 mM ATP stock (-80 C refrigerator)

2 mM βME: 0.6 µL of 14.3 M BME (Sigma 63689)

A5. Native Kinesin Motor Protein Purification

Day 1:

Streak a plate (evening):

1. Put your cell stock on ice allowing it to thaw slightly.
2. Select an agar plate as appropriate for the resistance of the gene in question (amp, kan, or both) – remember to let it sit upside down, slightly open to allow moisture to escape.
3. Flame the metal loop cell selection tool to sterilize, you can cool it off by sticking the tip into the edge of the agar plate.
4. Select a small amount of cells with the loop. They should appear as small ice crystals on the tip.
5. Spread the tip in a zig zag motion across one half of the plate, then draw the tip straight across that half and zig zag across the other half.
6. Place the plate upside down in the incubator. It should be ready to pick colonies the next morning.
7. Make your mix of TB growth media in two large Erlenmeyer flasks. The recipe for this is posted above the scales. – remember to add the antibiotics after autoclaving, amounts are posted above the scales (and 10 mg of biotin if using a BCCP motor). If there are no TB salts available, make those too. – remember that these must be autoclaved prior to use and before mixing.

Day 2:

Pick colonies and grow up the cells:

1. Select the same number of culture tubes with 2xYT media as the number of colonies you will pick (four is a good number). Pipette the appropriate amount of each antibiotic in each tube. Antibiotic stocks are found in the small refrigerator, usually in 1000x stock. The culture tubes typically contain 5 mL. Each tube requires 5 uL of each antibiotic.
2. Pick a few (two or three) individual colonies using a pipette tip and drop them into their own culture tube. – remember to flame the tube end and cap before and after dropping the pipette tip into the media.
3. Label the tubes if necessary and put them on the spinning wheel within the incubator.
4. Let the cells to reach an OD of about 1.0. It seems that most people judge this by eye as when the tube becomes cloudy and nearly opaque, but without any sedimentation at the bottom of the tube.

5. About thirty minutes prior to the cells reaching 1.0 OD place the 1/1.5 L growth flasks in the incubator at 37 C with agitation at about 220 rpm.
6. When the culture tubes are ready, dump one each into the large flasks and allow to grow during the day to an OD of 1.0. When checking the OD use 900 µL of the waste Millipore water and 100 µL of the cells, multiply the measured OD at 600 nm by 10.
7. When an OD of 1.0 /2.5 has been reached take the flasks out of the incubator and put them on ice. Give the flasks a spin to help them cool more uniformly and quickly. Also, open the incubator and reset its temperature for 22 C.

Induce expression of protein (Do this at the end of the day):

1. First, while the flasks are sitting on ice, collect a sample of the pre-induction cells in an Eppendorf tube. You can collect 1 mL, but you won't need that much to run SDS-PAGE analysis. Be sure to label, note the OD and store it in the -20 C refrigerator. (If using BCCP motors add 10 mg of biotin to each flask). Also, collect 1 mL for competent cell stock.
2. Induce expression by the addition of IPTG, 0.2 mM (48/180 mg) – (IPTG induces activity of beta-galactosidase an enzyme that promotes lactose utilization – to trigger transcription of the lac operon, by binding and inhibiting the lac repressor.)
3. Reintroduce the flasks to the incubator; now at 22 C, allow 16/22 hours for expression overnight.
4. Put rotors in 4 C refrigerator for tomorrow.

Day 3:

Collect and lyse the cells (Again start this early, you need the entire day):

1. Put the large rotor in the centrifuge and spin it at a medium speed (~ 1000 rpm), set the temperature to 4 C. You need to let the centrifuge and rotor equilibrate at this temperature before you introduce your cells.
2. Take another sample of the cells in an Eppendorf tube, again note the OD and label (post-induction), date, and store in -20 C refrigerator.
3. Take the clean large (500 mL) plastic rotor containers; balance the bottles with equal amounts of your cell solution. Or you can balance them in pairs. Do this on ice.
4. Centrifuge the bottles for 12 minutes at 4000 x g (5950 rpm) to pellet the cells.
5. While the cells are spinning go and collect the required liquid nitrogen from the chemistry stockroom. Do not let the cells sit in the centrifuge, they can resuspend.

6. Make your lysis buffers: Start by filling two 50 mL plastic tubes with 50 mL 1 x lysis buffer, pH to 8.0 (50 mL lysis buffer for each 1L culture). The rest of the procedure should be done on ice.
7. Add protease cocktail and supplements to each 50 mL lysis buffer:

   10 µM bestatin: 250 µL of 2 mM bestatin stock (-20 C refrigerator)
   1 µM phosphoramidon: 5 µL of 10 mM phosphoramidon stock (-20 C refrigerator)
   1 mM pefabloc: 12 g/500 µL of pefabloc/ 100 mM pefabloc stock (4 C refrigerator)
   1 µg/mL aprotinin: 5 µL of 10 mg/mL aprotinin stock (4 C refrigerator)
   10 µM leupeptin: 50 µL of 10 mM leupeptin stock (-20 C refrigerator)
   5 µM E-64: 125 µL of 2 mM E-64 stock (-20 C refrigerator)
   1 mM TAME: 500 µL of 100 mM TAME stock (-20 C refrigerator)
   1 mM ATP: 250 µL of 200 mM ATP stock (-80 C refrigerator)
   1 mM BME: 3.5 µL of 14.3 M BME (Sigma 63689) (4 C refrigerator)
8. When centrifugation is done quickly dump off the supernatant into 1L flask and put pellets on ice.
9. With each pellet with 10 mL of stock (unsupplemented) lysis buffer, then pour off (washes out extra media). In one of the 50 mL tubes add 50 mg of lysozyme (-20 C refrigerator, Sigma L6876) and use 40 mL (10 mL each) to resuspend pellets, and then combine them.
10. Flash-freeze the cells in liquid nitrogen, when the nitrogen stops boiling vigorously take the bottle out. Chop the cells well; add the remaining 10 mL of lysis buffer w/ lysozyme. Once the pellet is well separated then add 40 mL of lysis buffer with protease inhibitors and supplements. Mix for a slurry consistency.
11. Add 16 mg of DNAase (-20 C refrigerator, Sigma DN25) to 10 mL lysis buffer w/o lysozyme and add to lysate, allow to incubate on ice for 15 min.

Purify the protein:

1. Switch the rotor in the centrifuge to the SA-600 and allow to equilibrate at 4 C.
2. Transport the lysate equally to 4-6 50 mL centrifuge tubes and centrifuge at 10,000 x g (12000 rpm) for 15 min to pellet cellular debris.
3. While the cells are spinning equilibrate 4 mL of Ni resin with Lysis Buffer in a ~20 mL column.
4. After the first spin, place the supernatant in new tubes and spin again for 45 minutes.
5. Pour supernatant into 50 mL Falcon Tubes, dump resin into full tube, seal the end, and tumble at 4 C for 60 minutes.

6. During tumbling, prepare 40 mL of Ni Wash Buffer, add:
   100 µM ATP: 20 µL of 200 mM ATP stock (-80 C refrigerator)
   2 mM BME: 5.6 µL of 14.3 M BME (Sigma 63689)

   Prepare 6 mL of Ni Elution Buffer:
   100 µM ATP: 3 µL of 200 mM ATP stock (-80 C refrigerator)
   2 mM BME: 0.9 µL of 14.3 M BME (Sigma 63689)
7. After tumbling, collect some flow through for sample and discard the rest. Then rinse with Ni Wash Buffer, collect some periodically for sample.
8. Elute protein into Eppendorf tubes with ~300 µL aliquots of Ni Elution Buffer. Repeat at least eight times. Collect 10 µL samples for each elution.
9. Snap-freeze the samples in liquid nitrogen and store at -80 C.

A6. Kinesin Motor Protein Microtubule-Affinity Purification

Supplies:

Full pipette set & tips
50+ PR tubes
2 x 250 µg tubulin aliquots
3 M KCl
2 x 1.0 mL GTB at RT
200 mM ATP on ice
Glycerol
Millipore Water
2 x TLA 100.2 spinning tubes on ice
1 mM taxol at RT
100 mM AMP PNP on ice
Gloves, Pens, Timer
Motor Stock (do not thaw until step 8)
Extra 1.5 mL tubes
Marker, Calculator

1. Make 10x sucrose solution: Sonicate 100 mg sucrose into 46 µL GTB (optional).
2. Calculate the amount of tubulin needed. 3-4 fold excess of tubulin over motor is recommended. About 125 µg of motor is available in a 300 µL aliquot, requiring 500 µg of tubulin. Current tubulin stock has 250 µg per aliquot, use two aliquots. (05/13/2008 – I calculate ~520 µg tubulin needed for 150 µL elution)
3. Prepare a Cushion for step 5 of GTB and 60% glycerol. Make the following twice, keep at room temperature:

   440 µL GTB
   660 µL 100% glycerol
4. Pre-spin step: Thaw tubulin quickly at 37 C and place in ice. Pipette tubulin solution into cold TLA 100.2 spinning tube (~70 µL)(don't let the tubulin come to room temperature or some of it will polymerize and spin down) and spin 100 krpm 15 minutes at 4 C, a balance tube is necessary. The supernatant will contain the α/β-tubulin and the "junk" will form the pellet.
5. Polymerization step: Remove supernatant (tubulin) from invisible pellet and pipette into new 1.5ml tube, note the volume. Incubate for 10 minutes at 37 C, place centrifuge rotor in 37 C refrigerator also. Warm the centrifuge to 25 C for step 5. Add 1 mM taxol for 20 µM concentration after incubation (e.g. 1.5 µL into 75 µL).

6. Spin through cushion: Pipette 300 µL cushion in the bottom of a TLA 100.2 tube and add 6 µL 1 mM taxol to 20 µM (the cushion volume should exceed the tubulin solution volume). Layer the polymerized MTs carefully on top. Make a balance tube using cushion and H_2O. Place tubes in warm TL 100 rotor and spin 10', 80 krpm at 25 C.

7. Wash cushion: Prepare GTB Wash Buffer by adding 15 µL 1 mM taxol solution to 750 µL GTB at room temperature. After spin, pipette off the supernatant above the cushion carefully. Take a little of the cushion too, but do not expose the pellet. Add 100 µL wash buffer and rinse the sides of the tube without disturbing the cushion. Remove the rinse, then the cushion. Rinse the pellet (without disturbing) with another 100 µL Wash Buffer, remove the rinse.

8. Resuspend microtubules. Add 100/200 µL (see below) GTB Wash Buffer to resuspend the pellet.

9. Binding step: Combine motor and MT.

100 µL	200 µL	MT solution
3 µL	6 µL	1 mM taxol (20 µL final)
1.25 µL	2.5 µL	200 mM AMPPNP (1mM final)
150 µL	294.5 µL	Motor protein solution

Incubate at room temperature for 15' and keep 7 µL sample for a gel ("Pre"), then spin over a 300/600 µL cushion as before (step 5).

10. Take a 10 µL sample of the supernatant for a gel ("S1"), store the rest in a separate Eppendorf tube, and wash the cushion again exactly as in step 6.

11. Release step: Prepare release buffer. Less volume will give you a higher concentration, but more protein will remain bound to the MTs:

12.5 µL	30 µL	3 M KCl (300/700 mM final)
6.25 µL	12 µL	200 mM ATP•$MgCl_2$ (10/20 mM final)
2.5 µL	2.5 µL	1 mM taxol (20 µM final)
104 µL	84 µL	GTB

Resuspend MTs in release buffer and incubate at room temperature for 15 minutes, keep a 2.5 µL sample for a gel ("P1").

12. Transfer to a clean TLA 120.1 tube and spin 80 krpm at 25 C for 10 minutes. Pipette supernatant from TLA tube in 1.5ml tube; keep an 11 µL sample for a gel ("S2"). Add 10X sucrose to motors (optional). Make, e.g., 2 µL aliquot's into tubes already on ice and freeze in liquid nitrogen.

13. (Optional) Dialyze released motors in 100 mL nuclease-free H_2O for 10 minutes at 4 C.

13. Resuspend pellet in 85 µL water and take a 10 µL sample for a gel ("P2").

A7. Covalent Coating of Microspheres

Required Buffers:

40 mL Activation Buffer (10 mM MES, 100 mM NaCl, pH 6.0):

400 µL 1 M MES (Sigma M1317)

234 mg NaCl (Fisher Scientific S671)

pH with NaOH, sterile filter

40 mL Coupling Buffer (100 mM PBS, pH 7.4):

125 mg Monosodium phosphate, monohydrate (Fisher Scientific BP330)

830 mg Disodium phosphate, heptahydrate (Fisher Scientific BP331)

10 mL Quenching Solution (30 mM hydroxylamine hydrochloride, 100 mM PBS, pH 8.0):

31 mg Monosodium phosphate, monohydrate (Fisher Scientific BP330)

208 mg Disodium phosphate, heptahydrate (Fisher Scientific BP331)

21 mg hydroxylamine hydrochloride (Sigma 379921), sterile filter

40 mL Storage Solution (50 mM PBS, pH 7.6)

44 mg Monosodium phosphate, monohydrate (Fisher Scientific BP330)

452 mg Disodium phosphate, heptahydrate (Fisher Scientific BP331)

1 mL 10% azide solution in Storage Solution:

100 mg sodium azide (MP Biomedicals 102891), sterile filter

100 µL 50 mg/mL BSA in Storage Solution

5 mg acetylated BSA (Sigma B2518)

100 µL Storage Solution, sterile filter

Covalent Coating of 0.5 um diameter beads:

1. Wash carboxyl-modified microspheres in Activation Buffer:
   a. Add 100 (50) µL of 100 mg/mL; 10% solids; 4.83 nM beads e.g. non-fluorescent Bangs beads (PC02N) to 0.9 (0.95) mL Activation Buffer, sonicate cold.
   b. Wash beads three times by spinning 10 minutes at 9,300 g (10,000 rpm on Hermle) with resuspension in 1 mL Activation Buffer. Vortex and sonicate cold for 10 seconds between each wash.

2. NHS chemistry:
    a. Wash beads once more, resuspend in 500 µL, vortex & sonicate. Transfer to new tube, sonicate for 30s, then add 250 µL of Activation Buffer twice, one containing 5 (2.5) mg of EDAC (Calbiochem 341006) and the other with 5 (2.5) mg S-NHS (Pierce 24510). Vortex and sonicate solution cold for 10 seconds and shake at room temperature for 30 minutes.
    b. Sonicate, then add 1.4 (0.7) µL 14.3 M 2-mercaptoethanol to quench EDAC, mix well.
3. Protein Coupling:
    a. Wash beads three times in Coupling Buffer as in 1b with vortexing and sonication. Transfer beads to new tube after first wash.
    b. Wash beads once more this time resuspend in 0.5 (0.25) mL of Coupling Buffer, move to a new tube. About 6 (3) mg of protein is necessary to coat the beads.

    For PEG-3500/BSA/BSA-biotin beads add the following to solution:

    2.7 (1.35) mg PEG-3500 (JenKem HO-PEG3500-NH2) in 230 (115) µL CB

    3.3 (1.65) mg BSA (Sigma B2518) in 230 (115) µL CB

    80 (40) µL of 0.6 mg BSA-biotin (Thermo Scientific 29130) in 50 µL CB

    c. Sonicate cold 15 seconds then react overnight at 4 C with constant shaking.
4. Wash & Storage:
    a. Wash beads once as in 1b and resuspend in 1 mL Quenching Solution, vortex, sonicate, and shake for 2 hours at 4 C followed by 10 minutes at room temperature.
    b. Wash beads three times in 1, 0.5, 0.25 mL of buffer of choice, e.g. Storage Solution.
    c. After a fourth wash resuspend in original bead volume, i.e. 98 (49) µL Storage Solution, vortex, sonicate, transfer to new tube and add 1 (0.5) µL 10% sodium azide solution and 1 (0.5) µL 50 mg/mL BSA.

4. Turn the sea urchins over and wait for them to start releasing sperm (from the gonopore) – collect the sperm with a Pasteur pipette into an Eppendorf tube.
5. Dilute semen 3x with sea water (or Buffer1)

Purifying Axonemes (all steps at 0-4 C):

6. Spin 1900g for 5mins.
7. Resuspend pellet in buffer1 with 1% Triton X-100.
8. Homogenize in dounce.
9. Spin 1500g 5mins (to remove heads).
10. Collect supernatant.
11. Spin 12,000g 5mins (to recover broken axonemes).
12. Collect pellet.
13. Resuspend pellet in same volume of buffer1 with 1% Triton X-100.
14. Spin 1500g for 5mins.
15. Collect supernatant.
16. Spin at 12,000g for 5mins.
17. Collect pellet.
18. Resuspend pellet in same volume of buffer1.
19. Spin 12,000g for 5mins.
20. Repeat steps 13&14 three times (to wash).
21. Resuspend in Buffer2 and incubate for 10mins (to remove dynein and motors).
22. Spin at 12,000g 5mins.
23. Resuspend pellet in same volume of buffer1 with 50% glycerol.
24. Store at -20 C.

A8. Coating Biotin-Functionalized Microspheres with Streptavidin

1. Collect a separate stock of biotin-beads if desired.
2. Add 200 µL of Storage Solution to 1.0 mg streptavidin (Invitrogen S888 – note that you must weigh out more solid to get this mass based on ratio on container.), sterile filter. It is also sometimes a good idea to use Invitrogen S11224, fluorescent streptavidin for verification of bead surface chemistry.
3. Add 100 µL of sonicated stock PEG-3500/BSA/BSA-biotin beads. Sonicate cold for 15 seconds.
4. Incubate for 30 minutes at room temperature with continuous shaking.
5. Wash 1x at 4 C; 11900 rpm for 2 minutes on Hermle with resuspension volume of 1 mL (Do not wash too hard, i.e., leave some residual supernatant volume). Vortex and sonicate cold in between.
6. Allow this mixture to incubate overnight at 4 C with shaking.
7. Wash 4x as above with 1, 0.5, 0.25 mL & 50 µL resuspension volumes. Move 50 µL to new container.
8. After resuspension, spin 3 min. at 1000 rpm on Hermle to pellet any large aggregates that may have formed.
9. Keep supernatant in new tube and add 1 µL 10% azide solution (and maybe 1 µL of 100 mg/mL BSA in GTB20s solution).
10. Use the following empirically-determined equation to estimate the bead concentration:

    $$\text{Microsphere Concentration (pM)} = (-0.4925)x^2 + (1.8642)x + (0.0091),$$

    Where, x, is the measured absorption at 500 nm using the spectrophotometer. Note: 'x' must be in the range 0.02 – 0.18 for the equation to be valid. Typically dilute 1 µL of beads into 1 mL total Milli-H_2O and perform measurement. Equation gives concentration of dilution, not of the stock solution.
11. For optical trapping motor assays it is preferable to store beads at approximately 250 pM.

A2. Z_R-$(ELS)_6$ Expression Protocol

Streaking Plate

1. Make 500 mL 8M Urea pH 8.0 and 100 mL GuCl pH 8.0.
2. Pre-warm a kan-amp plate
3. Briefly defrost cell stock on ice
4. Streak the plate with a sterilized wire loop
5. Place plate in incubator at 37 C overnight

Culture Tube Growth

1. Add 5 µL of 1000X kan and amp solutions to 3-5 mL culture tubes, flame culture tubes when opening and closing
2. Using a medium size pipette tip, pick one colony and add to the 5 mL culture tubes place labeled tubes in the rotary incubator at 37 C until submerged tip is no longer visible (i.e. solution becomes dark due to bacteria density).

Expression Media Preparation

1. Prepare two 2 L Erlenmeyer flasks as follows:
    a. 12 g casein (tryptone digest)
    b. 24 g yeast extract
    c. 4 mL glycerol
    d. 900 mL Millipore H_2O
2. Autoclave, liquids cycle
3. Add to the flasks once they cool:
    a. 100 mL TB salts
    b. 35 mg kanamycin
    c. 50 mg ampicillin

Cell Stock Preparation

1. Take a 500 µL sample from one of the culture tubes and add it to a cell stock tube.
2. Add an additional 500 µL of cell stock solution (20% glycerol) and add it to the cell stock tube.
3. Label the tube with: protein name, antibiotic resistance, cell type: BL21, Initials, data
4. Store the cell stock in at -80 C.

Large-Scale Growth and Expression

1. Pre-warm large expression flasks in shaker incubator at 37 C and 250 rpm.
2. Pour media from culture tubes into flasks (one culture tube per flask)
3. Power on spectrophotometer and set to 600 nm reading, blank with 1 mL milli-H_2O.
4. Periodically (every 1-2 hours) check OD of each flask and record.
5. Once the flasks reach an OD of 1 (roughly 5 hours), take a 1 mL sample labeled pre-inoculation and store it in the -20 C freezer.
6. Weight out 238 mp IPTG (located in -20 C) for each flask and add this to each flask (bringing flask to 1 mM IPTG).
7. Allow the flasks to incubate for a minimum of 5 hours, overnight is acceptable.
8. At the end of expression, take an additional 1 mL sample labeled post-inoculation and store it in the -20 C freezer. Also, take an additional 600 nm reading (should be around 1.1-1.2).

Centrifugation and Cell Lysis

1. Pre-chill the large centrifuge with the large rotor inserted by spinning at 5000 rpm 4 C for 30 minutes.
2. Pre-weigh two 500 mL centrifuge containers and record the weights on the containers and lids.
3. Distribute culture between the two containers and weight them, they should be within 100 mg of each other. (480 g each)
4. Spin the containers for 8 minutes at 8000g and 4 C (6900 rpm).
5. Pour liquid into sink, leaving cell pellet undisturbed.
6. Continue steps 3-5 until all culture is used.
7. Reweight the containers and determine the mass of the cell pellets.
8. Transfer as much of the pellet as possible from one container to the other, so that all the cellular material is in on e container.
9. Add 5 mL of 8M urea (pH8.0) for every gram of cell pellet (Pour about a third onto the empty container to wash out as much of the remaining material as possible then add the contents to the other container).
10. Chop up the cell pellet briefly so that it is freely suspended in the urea.
11. Add a medium size stir bar to the container, cap it, and allow it to sit while stirring in the 4 C refrigerator overnight.

Protein Isolation:

1. Ensure the entire cell pellet mass is dissolved in the 8 M urea solution (pH 8.0).
2. Pre-chill the large centrifuge with the small rotor inserted.

3. Aliquot the liquid into as many small centrifuge tubes as are necessary keeping them within 100 mg of each other (usually 2-3 tubes is sufficient).
4. Spin the small centrifuge tubes for 15 minutes at 12000 rpm and 4 C.
5. Pour the liquid into a new set of small centrifuge tubes (check weights again)
6. Spin the small centrifuge tubes for 25 minutes at 15000 rpm and 4 C.
7. Transfer the liquid from the tubes into 50 mL tubes.

Protein Purification

1. Run ~50 mL of 8 M urea (pH 4,5) through the $Z_R(ELS)_6$ column.
2. Equilibrate the column with an additional 25-50 mL of 8 M Urea (pH 8.0). Note: never let the column run dry.
3. Add as much of the column resin to each of the 50 mL conical tubes as possible.
4. Parafilm the caps to ensure a seal, and place them on the rotator in the 4 C refrigerator for at least 1 hour.
5. While rotating, prepare and label two wash tubes and one elution tube.
   a. Wash Tube (50 mL tube): 1 mM BME
      25 mL 8 M Urea (pH 8.0)
      167 µL BME (150 mM BME stock)
   b. Elution Buffer (15 mL tube) 1 mM BME
      10 mL 6 M Guanidinium Chloride (pH8.0)
      67 µL BME (150 mM BME stock)
6. Spin the 50 mL conical vial at 1000 rpm for 10 minutes (table top centrifuge).
7. Pour out a s much liquid as possible while leaving the pellet undisturbed.
8. Resuspend pellet in remaining liquid (add additional 8 M urea if necessary) and pour all contents on to the column.
9. Allow the nickel resin to settle.
10. Open the column and collect the flow through in a 2 mL tube.
11. Once the flow thru has completely entered the bed, add the first wash tube and allow the resin to settle.
12. Open the column and collect all the liquid in a 2 mL tube.
13. Once the first wash ahs completely entered the bed, add the second wash tube and allow the resin to settle.
14. Open the column and collect all the liquid in a 2 mL tube.
15. Once the second wash has completely entered the bed, add the 1.5 mL of elution buffer and allow the resin to settle (let it incubate for 5-10 minutes –only necessary for elutions 1 and 2).
16. Open the column and collect all the liquid in a 2 mL tube.

17. Repeat until 15 elutions have been collected.
18. Collect the following samples in labeled 1 mL microcentrifuge tubes and store them at -20 C.

    1 mL flow through
    1 mL Wash 1
    1 mL Wash 2
    20 µL elution 1-4
19. Pool all elutions into 1-15 mL tube.

Dialysis:

1. Equilibrate sufficient size 6-8000 MWCO dialysis tubing (usually 1-10 cm) in Millipore H_2O in cylindrical dish for 20-60 minutes.
2. Clamp one end with a dialysis clip and aliquot the liquid from step 19 in protein purification into the tubing.
3. Attach a second clip to the other end, trying to minimize bubbles in the tubing.
4. Pour cold Millipore H_2O in to a 4 L beaker adding a large stir bar.
5. Place the tubing containing the sample into the 4 L beaker and cover with aluminum foil.
6. Exchange the water in the 4 L beaker with at least 2 hour gaps until a minimum of 6 exchanges have occurred (~2 days).

Lyophilization

1. Aliquot the samples from the dialysis tubing into labeled 50 mL tubes (no tubes should exceed 20 mL).
2. Place the 50 mL tubes into the -20 C sitting at an angle until the surface is frozen.
3. Inspect the tubes for cracks, assuming no cracks, move the tubes to the -80 C and loosen the caps.
4. Once the samples are completely frozen (about 30-45 minutes at -80 C), tighten the caps and place the samples on ice.

5 Knock the ice off the tubes, remove the caps and place a VWR wipe over the top using a rubber band to secure it.

6. Place all the tubes in a large lyophilizer container with several VWR wipes at the bottom and cap the container.
7. Turn any samples on the lyophilizer to the hold position, connect your container, and turn it to the on vacuum position.
8. Once the pressure on the lyophilizer is less than 100, turn the other samples back to vacuum and ensure the pressure remains under 100.
9. Leave the sample on the lyophilizer for 2 days.

10. To remove the samples: Place all the other samples on hold, turn your sample to the atmosphere position and remove your sample.
11. Turn the other samples back to vacuum and ensure the pressure remains below 100.

A3. Protein/DNA Conjugation Protocol

Required reagents:

8 M Urea (1 L)

13.8 g monobasic sodium phosphate (100 mM)
1.2 g Tris (10 mM)
480.5 g urea (8 M)
Adjust to pH 7.2

10X PBS (1 L)

80 g NaCl
2.0 g KCl
14.4 g dibasic sodium phosphate
2.4 g monobasic potassium phosphate

Adjust to pH 7.3.

Conjugation Buffer (1 L)

2.758 g 20 mM NaH_2PO_4
21.44 g 80 mM Na_2HPO_4

8.766 g 150 mM NaCl
2 mL 0.5 M EDTA (292 mg)
Adjust to pH 7.3.

Sulfo-SMCC (Pierce #22322)
DMF (N,N-Dimethylformamide, Fisher #AC61032-1000)
TCEP (Pierce #20490)
Urea (USB #23036)
Tris (USB #75825)
Sodium Chloride (Fisher #S671-500)
Potassium Chloride (Sigma #P9641)
Monobasic Sodium Phosphate (Fisher #BP330-1)
Dibasic Sodium Phosphate (Fisher # BP 331-1)
Monobasic Potassium Phosphate (USB #20227)
EDTA (USB #15700)
NAP 5 Column (GE Healthcare #17-0853-02)

1. Suspend the protein at a concentration of 10 mg/mL in 8 M urea, pH 7.2. Combine 450 µL of the protein with 50 µL TCEP (400 mM, pH 4.5 – 115 mg in 1 mL). Incubate for 1.5 hours at 37 C. While incubating, equilibrate one NAP-5 column with 10 mL of urea (8 M, pH 7.2).

2. After incubation, add 500 µL of the reduced protein to the NAP-5 column, and elute with 1 mL urea (8 M, pH 7.2), yielding a final volume of 1 mL protein.
3. Combine 100 µL amine-terminal DNA (100 µM), 100uL conjugation buffer, and 60 µL sulfo-SMCC (2 mg sSMCC/60 µL DMF). Incubate for 1 hour at 37 C. While incubating, equilibrate a second NAP-5 column with 10 mL 1X PBS (pH 7.2).
4. After incubation, add 240 µL conjugation buffer to the DNA tube and add 500 µL of the DNA solution to the NAP-5 column and elute with 1 mL 1X PBS, yielding a final volume of 1 mL DNA.
5. Combine 500 µL of protein and 500 µL DNA in two 2 mL tubes wrap them in foil and react them while vortexing. After 2 hours, move the vortexer to 4 C and react overnight.
6. Finally do another round of dialysis, followed by FPLC, a final round of dialysis, and lyophilization as done previously.

A4. Kinesin Motor Protein Purification Reagents

The following is a list of the solutions needed for the purification procedure. Note: For all buffers made in water use Sigma W4502.

Protease Inhibitor Stocks:

Bestatin (Sigma B8385)-1 mg

Make 2 mM stock solution (1 mg in 1.45 mL H_2O), store at -20 C, and mark with one month expiration date (lasts at least one month).

Phosphoramidon (Sigma R7385)-0.5 mg

Make 10 mM stock solution (0.5 mg in 85.1 µL H_2O), store at -20 C, and mark with one month expiration date (lasts at least one month).

Pefabloc (Sigma 76307)-100 mg

Make 100 mM stock solution (24 mg in 1 mL H_2O), store at 4 C, and mark with three month expiration date (lasts up to six months).

Aprotinin (Sigma A1153)-1 mg

Make a 10 mg/mL stock solution (1 mg in 100 µL H_2O), store at 4 C, mark with one year expiration date (4% loss of activity per year at this concentration and temperature).

Leupeptin (Sigma L2884)-1 mg

Make a 10 mM stock solution (1 mg in 210.3 µL H_2O), store at -20 C, mark with six month expiration date (lasts at least six months).

E-64 (Sigma E3132)-1 mg

Make a 2 mM stock solution (1 mg in 1.40 mL H_2O), store at -20 C, and mark with three month expiration date.

TAME (Sigma T4626)-5g

Make a 100 mM stock solution (38 mg in 1 mL H_2O), store at -20 C, and mark with 1 month expiration date.

A9. Kinesin Motor Protein Optical Trapping Assay Reagents

Motility Protocol Required Stocks:

1. 10 mL of 100X potassium acetate (5 M):
   a. 4.9 g potassium acetate (Sigma P1190) in 10 mL Millipore water.
   b. Sterile filter, store at 4 C.
2. 10 mL of 1000X magnesium chloride (4 M)
   a. 8.1 g magnesium chloride (USB 18641) in 10 mL Millipore water.
   b. Sterile filter, store at 4 C.
3. 10 mL of 100X EGTA (0.1 M)
   a. 380 mg EGTA (USB 15703) in 10 mL Millipore water.
   b. Sterile filter, store at 4 C.
4. 5 mL of GTB80s (4X Buffer)
   a. 5 mL GTB (Cytoskeleton BST01)
   b. 200 µL 100X potassium acetate.
   c. 18.75 µL 1000X magnesium chloride.
   d. 150 µL 100X EGTA
   e. Sterile filter, store at 4 C.
5. 1 mL of 100X DTT (0.2 M):
   a. 30.85 mg of DTT (Denville Scientific CD-4070-13) in 1 mL Millipore water
   b. Sterile filter.
   c. Aliquot into 50 µL volumes, store at -20 C.
6. 500 µL of 100X glucose oxidase:
   a. 25 mg of glucose oxidase (Sigma G-2133) in 250 µL glycerol (USB 16374), 125 µL GTB, and 125 µL Millipore Water.
   b. Sterile filter, store at 4 C.
7. 200 µL of 100X catalase:
   a. Mix 100 µL of stock catalase (Roche 10681356) and 100 µL glycerol (USB 16374).
   b. Sterile filter, store at 4 C.
8. 1 mL of 20X glucose (1 M):
   a. 180 mg glucose (Sigma G8270) in 1 mL Millipore water.
   b. Sterile filter, store at 4 C.
9. 200 mM ATP stock
10. Motor Stock
11. 500 µL of 25 mg/mL alpha-casein in GTB

a. Add 12.5 mg alpha-casein (Sigma C8032) to 125 µL GTB
b. Add 375 µL Millipore water
c. Sterile filter, store at 4 C.

If final ATP concentration is in the micromolar range:

12. 1 mL of 100X creatine phosphokinase:
    a. 1.3 mg of creatine phosphokinase (Sigma-Aldrich C3755) in 250 uL GTB.
    b. Add 750 µL Millipore water
    c. Sterile filter, store at -20 C.
13. 1 mL of 100X phosphocreatine (0.2 M):
    a. 51 mg of phosphocreatine disodium salt hydrate (Sigma-Aldrich P7936) in 250 µL GTB.
    b. Add 750 µL Millipore water.
    c. Sterile filter, store at -20 C.

Final Assay Concentrations:

Motility Buffer:

20 mM PIPES, pH 6.8, 50 mM potassium acetate, 4 mM magnesium chloride, 1 mM EGTA, 2 mM DTT

Oxygen Scavenging System:

500 µg/mL glucose oxidase, 100 µg/mL catalase, 9 mg/mL glucose

ATP Regeneration System (if needed):

2 units/mL creatine phosphokinase, 2 mM phosphocreatine

Miscellaneous:

10 µM taxol, 2 mM ATP, 0.5 mg/mL alpha-casein

A10. Kinesin Motor Protein Optical Trapping Sample Preparation

Prepare Motor/Bead Incubation:

1. Add 1 µL of 1/8 – 1/16 dilution (dependent on motor stock) of pre-formed Linker-Scaffold (836 nM stock) to 2 µL motor pull down stock (~100 – 300 nM). Shake for 20 minutes at 4 C.
2. During the shake, aliquot 1 µL of ¼ dilution of homemade Streptavidin/BSA/PEG beads (275 nM stock) into a PCR tube. Sonicate in ice bath for 10-15 seconds. Spin down beads in Eppendorf MiniSpin by a brief 10 krpm spin if needed.
3. Dilute all 3 µL of Motor-Linker-Scaffold mixture from above in GTB20s to allow for the appropriate amount of bead motility (typically add 30 – 60 µL).
4. Add 3 µL (1.5 x 2) of M-L-S dilution to 1 µL microspheres. Shake for 40 minutes at 4 C.
5. Room Preparation: Initialize all necessary programs and turn on all instruments, except for those that cause or require laser emission.

Prepare Assay Solutions:

1. Prepare 50 (25) µL of 10X Oxygen Scavenging System, adequate for 4 (2) slides, and keep on ice:

5 (2.5) µL	100X glucose oxidase
5 (2.5) µL	100X catalase
5 (2.5) µL	100X DTT
13 (6.5) µL	GTB80s
22 (11) µL	Millipore water

2. Prepare 450 (225) µL of Buffer Mix:

26 (13) µL	1 M Glucose
113 (56.5) µL	GTB80s
19 (9.5) µL	alpha-casein (12 mg/mL)
292 (146) µL	Millipore water

Slide Preparation:

1. Flow 1X CV with axoneme solution diluted 1:5 in GTB20s; do not allow time to settle, immediately...
2. Fill chamber with alpha-casein (1 mg/mL in GTB20s) twice, allow chamber to incubate for 2 minutes. Repeat with a single wash.
3. Final Sample Preparation:

   Mix the following:

85 (40.5) µL	Buffer Mix
1 (0.5) µL	ATP (200 mM stock)

10 (5) µL 10X oxygen scavenger
Mix well before addition of motor/bead complex.
4 µL bead/motor assembly
100 (50) µL Total

4. Add 2X CV of this mixture to the slide. Note the time and seal, do not use any slide preparation for longer than 90 minutes.